

University of Central Florida

**STARS**

---

Electronic Theses and Dissertations, 2020-

---

2023

# Ocean Vector Wind Measurement Potential from the Global Precipitation Measurement Mission using a Combined Active and Passive Algorithm

Alamgir Hossan

*University of Central Florida*



Part of the [Electrical and Computer Engineering Commons](#)

Find similar works at: <https://stars.library.ucf.edu/etd2020>

University of Central Florida Libraries <http://library.ucf.edu>

This Doctoral Dissertation (Open Access) is brought to you for free and open access by STARS. It has been accepted for inclusion in Electronic Theses and Dissertations, 2020- by an authorized administrator of STARS. For more information, please contact [STARS@ucf.edu](mailto:STARS@ucf.edu).

---

## STARS Citation

Hossan, Alamgir, "Ocean Vector Wind Measurement Potential from the Global Precipitation Measurement Mission using a Combined Active and Passive Algorithm" (2023). *Electronic Theses and Dissertations, 2020-*. 1889.

<https://stars.library.ucf.edu/etd2020/1889>

**OCEAN VECTOR WIND MEASUREMENT POTENTIAL FROM THE GLOBAL  
PRECIPITATION MEASUREMENT MISSION USING A COMBINED ACTIVE AND  
PASSIVE ALGORITHM**

by

ALAMGIR HOSSAN

B.Sc. Engr., University of Chittagong, 2011

M. Sc. Engr., University of Chittagong, 2013

M.S., University of Central Florida, 2019

A dissertation submitted in partial fulfillment of the requirements  
for the degree of Doctor of Philosophy  
in the Department of Electrical and Computer Engineering  
in the College of Engineering and Computer Science  
at the University of Central Florida  
Orlando, Florida

Spring Term  
2023

Major Professor: W. Linwood Jones

© 2023 Alamgir Hossan

## ABSTRACT

Ocean surface vector wind (OVW) is an essential parameter for understanding the physics and dynamics of the ocean-atmosphere system, thereby improving weather forecasting and climate studies. Satellite scatterometers, synthetic aperture radars, and polarimetric microwave radiometers have provided almost global coverage of ocean surface vector wind for the last four decades. Nonetheless, a consistent and uninterrupted long-time data record with the capability of resolving sub-diurnal variability has remained a critical challenge over the years.

The Global Precipitation Measurement Mission (GPM) is a satellite mission designed to provide space-based precipitation information on a global scale with complete diurnal sampling. This dissertation presents a combined active and passive retrieval algorithm to investigate the feasibility of ocean surface vector wind measurements from the GPM core satellite by utilizing its Ku- and Ka-band Dual-frequency Precipitation Radar (DPR) and the multi-frequency GPM Microwave Imager (GMI) observations.

The unique GPM active and passive geophysical model functions were empirically developed by characterizing the anisotropic nature of ocean backscatter of normalized radar cross-section ( $\sigma^\circ$ ) and brightness temperature ( $T_B$ ) at multiple bands. For passive GMF, the modified 2<sup>nd</sup> Stoke's parameter (linear combination of V and H-pol  $T_B$ s) was used to mitigate the atmospheric contamination and to enhance the anisotropic wind direction signal superimposed on GMI  $T_B$ s.

The GMFs were combined in a maximum likelihood estimation (MLE) algorithm to infer the OVW. Finally, the retrieval algorithm was validated by comparing OVW retrievals with collocated NASA Advanced Scatterometer (ASCAT) wind vectors. The wind speed and direction retrieval performance statistics are promising and comparable with those of conventional

scatterometer and polarimetric radiometer data products. The algorithm demonstrates the capability of the GPM to provide a long-term OVW data record for the entire GPM-TRMM era, which may include unique monthly diurnal OVW statistics.

*To my teachers, Subash Chandra Nath, Pradip Kumar Barua, Arif Iftakher Mahmood, Kazi*

*Tanvir Ahmmed, and all others.*

*To my parents, Rokeya Begum & Md. Abdul Mabud*

*To my elder sister and other siblings*

*To my wife Nahid and daughter Alvina*

## ACKNOWLEDGMENTS

First, I would like to thank my adviser, Dr. W. Linwood Jones, for his endless time, guidance, and all-around support for the past six years! I consider myself very fortunate for having him as my mentor and I convey my gratitude to him for giving me every opportunity to learn and sharing his expertise and passion for the field. I would also like to thank the other committee members: Dr. Wasfy B. Mikhael (UCF), Dr. Xun Gong (UCF), Dr. Mark Bourassa (FSU), Dr. Josko Zec (FIT), and Dr. Suleiman Alsweiss, (GST/NOAA) for their time and suggestions that helped enhance the quality of my dissertation.

I am thankful to NASA Earth science division for their funding which supported part of my dissertation research. I want to thank UCF for providing all the facilities for my dissertation research. Thanks to all the NASA GPM Intercalibration (XCAL) Working Group members, especially Dr. Wes Berg of Colorado State University (CSU), for their support and assistance.

I am grateful to Dr. Suleiman Alsweiss of NOAA STAR/Global Science and Technology (GST) for his help and mentorship in my professional development. I sincerely appreciate all my colleagues at Central Florida Remote Sensing Laboratory (CFRSL) for their cooperation and for creating a friendly work environment. In particular, I would like to thank Dr. Maria March Jacob for her continuous motivation, and Dr. Ruiyao Chen, who helped me with a smooth transition into CFRSL projects during the initial phase. Thanks to all my teachers, mentors, and all my other friends and relatives who have always inspired me to keep going and excel.

Finally, I would like to thank my wife, Nahid, for always having trust in me and listening to my dreams, and my daughter, Alvina, for being a source motivation!

# TABLE OF CONTENTS

ABSTRACT.....	iii
ACKNOWLEDGMENTS .....	vi
TABLE OF CONTENTS.....	vii
LIST OF FIGURES .....	xi
LIST OF TABLES .....	xvi
CHAPTER 1: INTRODUCTION.....	1
1.1: Background .....	1
1.2: Aim and Overview of the Dissertation.....	4
1.3: Organization of the dissertation .....	5
CHAPTER 2: MICROWAVE REMOTE SENSING OF OCEAN VECTOR WINDS.....	7
2.1: Introduction .....	7
2.2: Active Measurement of Ocean Vector Wind .....	8
2.2.1: Geophysical Model Function (GMF).....	12
2.2.2: Scatterometer Characteristics.....	12
2.2.3: OVW Retrieval Algorithm.....	14
2.3: Passive Measurement of Ocean Scaler and Vector Wind.....	15
2.4: Combined Active and Passive Measurement of Ocean Vector Wind.....	20
2.5: Global Precipitation Measurement Mission.....	20



2.5.1:	GPM Instruments .....	21
2.5.2:	Technical Challenges .....	24
CHAPTER 3:	ACTIVE GEOPHYSICAL MODEL FUNCTION .....	26
3.1:	Introduction .....	26
3.2:	Methods .....	28
3.2.1:	GPM Dual-Frequency Precipitation Radar (DPR) .....	29
3.2.2:	Collocation and Quality Control .....	30
3.3:	Geophysical Model Function for the Ocean Ku and Ka-Band PR Backscatter .....	31
3.3.1:	Binning .....	34
3.3.2:	Wind Speed and Incidence Angle Dependence of $\sigma_0$ .....	35
3.3.3:	Azimuthal Anisotropy of $\sigma_0$ .....	38
3.3.4:	Sea Surface Temperature Dependence of $\sigma^0$ .....	43
3.4:	Discussion .....	46
CHAPTER 4:	PASSIVE GEOPHYSICAL MODEL FUNCTION .....	48
4.1:	Introduction .....	48
4.2:	Radiative Transfer .....	48
4.3:	Methodology .....	51
4.3.1:	Matchup Dataset, Pre-processing, and Binning .....	51
4.4:	Brightness Temperature Signal .....	55

4.5:	Atmospheric Clearing .....	61
4.6:	AV-H Geophysical Model Function .....	63
4.7:	Wind Speed Retrieval Algorithm.....	68
4.7.1:	Statistical Regression.....	68
CHAPTER 5:    COMBINED ACTIVE AND PASSIVE OVW RETRIEVAL ALGORITHM		70
5.1:	Introduction .....	70
5.2:	Maximum Likelihood Estimation .....	70
5.3:	Retrieval Algorithm.....	72
5.3.1:	Ambiguity Removal.....	78
CHAPTER 6:    RESULTS AND DISCUSSION.....		80
6.1:	Introduction .....	80
6.2:	Validation.....	80
6.2.1:	Validation Matchup Dataset .....	80
6.2.2:	Wind Speed Validation .....	81
6.2.3:	Wind Direction Validation.....	83
6.2.4:	Retrieval Skill .....	87
6.3:	Discussion .....	89
CHAPTER 7:    CONCLUSION AND FUTURE WORK.....		91
7.1:	Summary .....	91

7.2: Significance of the Study .....	94
7.3: Directions for Future Work .....	95
7.3.1: More Appropriate Noise Model.....	95
7.3.2: An Objective Ambiguity Removal .....	95
7.3.3: Secondary Effects .....	95
7.3.4: Other Potential Improvements .....	96
APPENDIX A: NEUTRAL STABILITY WINDS .....	98
APPENDIX B: COPYRIGHT PERMISSION LETTERS .....	101
REFERENCES .....	103

## LIST OF FIGURES

Figure 2.1: Basic principle of active remote sensing, (a) ocean surface backscattering, (b) wind retrieval algorithm.....	11
Figure 2.2: Basic principle of passive remote sensing, (a) ocean surface scattering, (b) wind retrieval algorithm.....	17
Figure 2.3: GPM core observatory and its sensors ( <i>Credits: NASA Global Precipitation Measurement Mission</i> ).....	21
Figure 2.4: GMI and DPR azimuth diversity.....	25
Figure 3.1: Scan pattern of GPM DPR: (a) before May 21, 2018, and (b) after May 21 2018. Blue circles indicate KuPR footprints, while yellow and pink circles represent matched (KaMS), and high sensitive (KaHS) swath of Ka [81].....	30
Figure 3.2: Spacecraft heading and DPR azimuth viewing angle. ....	33
Figure 3.3: Binnig procedure for $\sigma^0$ geophysical model function.....	35
Figure 3.4: Mean value of binned KuPR (top panel) and KaPR (bottom panel) $\sigma^0$ as a function of wind speed for different earth incidence angle $\theta$ for upwind (left), downwind (middle), and crosswind (right) relative wind directions. ....	36
Figure 3.5: Mean value of binned KaPR (top) and KuPR (middle) $\sigma^0$ as a function of earth incidence angle $\theta$ , for different wind speeds.....	37
Figure 3.6: Wind speed sensitivity of Ka-band vs. Ku-band $\sigma^0$ with EIA: the left-side Fig. compares the maximum variation of $\sigma^0$ for WS change 1 m/s to 20 m/s at Ku-band (blue) with Ka-band (red) at averaged relative wind direction; the right-side Fig. plots the same, but for upwind (solid line), downwind (dashed-dot line), and crosswind (dashed line) directions. ....	38

Figure 3.7: KuPR (top panel) and KaPR  $\sigma^0$  (bottom panel) directional anisotropy (in dB) as a function of relative wind direction ( $\chi$ ) for three different WS values: 6 m/s (blue), 10 m/s (red), and 14 m/s (black) at different earth incidence angles (indicated at the top of each figure). The symbols are bin average, while the solid lines represent their second-order Fourier fits. .... 39

Figure 3.8: Peak-to-peak KuPR (left) and KaPR (right)  $\sigma^0$  downwind/upwind asymmetry (in dB) as a function of WS at different EIAs. .... 41

Figure 3.9: Peak-to-peak KuPR(left) and KaPR (right) downwind/crosswind  $\sigma^0$  anisotropy (in dB) as a function of WS at different EIAs. .... 42

Figure 3.10: PR sweet swath for OVW retrieval ..... 43

Figure 3.11: SST dependence of KuPR and KaPR  $\sigma^0$  at different EIA. Relative  $\sigma^0$  here indicates  $\sigma^0 / \sigma^0(@15C)$  ratio. .... 45

Figure 3.12: SST dependence of KuPR and KaPR  $\sigma^0$  at different EIA. Relative  $\sigma^0$  here indicates  $\sigma^0 / \sigma^0(@15C)$  ratio. .... 45

Figure 4.1: Illustration of (a) wind direction in oceanographic and meteorological convention and (b) relative wind direction. A thick black arrow indicates the wind vector, and the square box at the center of the Cartesian coordinate system represents a typical wind vector cell (WVC). Angles are depicted, and their interrelation is given in the caption on the top right..... 54

Figure 4.2: Binnig procedure for *TB* and AV-H geophysical model function ..... 55

Figure 4.3: Sea surface temperature signature (SST) of GMI brightness temperature at nine lower frequency channels for wind speeds 6, 10, and 14  $ms^{-1}$  ..... 56

Figure 4.4: Sea surface temperature (SST) signal (with mean removed) of GMI brightness temperature at nine lower frequency channels for wind speeds 6, 10, and 14  $ms^{-1}$  ..... 56

Figure 4.5: Wind speed (WS) signature of GMI brightness temperature at nine lower frequency channels for sea surface temperatures of 4, 12, 20, and 28 °C. .... 57

Figure 4.6: Wind speed (WS) signal (with mean removed) of GMI brightness temperature at nine lower frequency channels for sea surface temperatures of 4, 12, 20, and 28 °C. .... 58

Figure 4.7: Wind speed (WS) signal and sea surface temperature (SST) dependence of GMI brightness temperature at nine lower frequency channels. .... 58

Figure 4.8: Wind direction (WD) signature of GMI brightness temperature at nine lower frequency channels for wind speed 6, 10, and 14 ms<sup>-1</sup> at sea surface temperature of 20 °C. .... 59

Figure 4.9: Wind direction (WD) signal (with DC terms removed) of GMI brightness temperature at nine lower frequency channels for wind speeds 6, 10, and 14 ms<sup>-1</sup> at sea surface temperature of 20 °C. .... 60

Figure 4.10: Standard deviations of GMI brightness temperature bins at nine lower frequency channels for wind speeds 6, 10, and 14 ms<sup>-1</sup> at sea surface temperature of 20 °C. .... 61

Figure 4.11: Atmospheric clearing factor (A) for 10, 19, 37, and 89 GHz GMI channels as a function of wind speeds and sea surface temperature. .... 63

Figure 4.12: Wind direction (WD) signals of AV-H combinations at wind speeds 6, 10, and 14 ms<sup>-1</sup> and sea surface temperature of 20 °C for 10, 19, 37, and 89 GHz GMI channels as a function of relative wind direction. .... 65

Figure 4.13: AV-H offset for 10, 19, 37, and 89 GHz GMI channels as a function of wind speeds and sea surface temperature. .... 66

Figure 4.14: Sea surface temperature (SST) and wind speed (WS) dependence of AV-H offset for 10, 19, 37, and 89 GHz GMI channels. Mean AV-H are plotted as a function of SST (top) and WS (bottoms). .....	66
Figure 4.15: Standard deviations of AV-H bins at wind speeds 6, 10, and 14 ms <sup>-1</sup> and sea surface temperature of 20 °C for 10, 19, 37, and 89 GHz GMI channels as a function of relative wind direction. ....	67
Figure 4.16: Peak-to-peak directional anisotropy and corresponding standard deviations of AV-H residuals at sea surface temperatures of 4, 12, 20, and 28 °C for 10, 19, 37, and 89 GHz GMI channels as a function of wind speed.....	68
Figure 5.1: Combined active and passive OVW retrieval algorithm.....	74
Figure 5.2: Example MLE surfaces -- active (top) and passive (bottom).....	75
Figure 5.3: Example MLE surfaces -- active (top row) and passive, which are circularly shifted to match the azimuth with active counterpart (middle row), and different combination of active and passive MLE (bottom row); the leftmost is the combination of Ku-band PR and 10 GHz AV-H, the next is the same except it adds the 19 GHz AV-H MLE. The following one (3 <sup>rd</sup> row, 3 <sup>rd</sup> column) adds Ka-band MLE with the previous one, and finally, the rightmost on the bottom panel shows the combination of MLEs from Ku- and Ka-band, and 10,19, and 37 GHz AV-H MLEs.....	76
Figure 5.4: MLE cost function and probable solutions.....	78
Figure 6.1: Distribution of validation dataset .....	81
Figure 6.2: GMI wind speed retrieval performance.....	82
Figure 6.3: MLE wind speed retrieval performance .....	83
Figure 6.4: Wind direction retrieval performance .....	85

Figure 6.5: Wind direction retrieval performance comparison: (1<sup>st</sup> column) the left most is the combination of Ku-band PR and 10 GHz AV-H, (2<sup>nd</sup> column) the next is the same except it adds the 19 GHz AV-H; (3<sup>rd</sup> column) the following one adds Ka-band with the previous one, and finally, (4th column) the rightmost on the bottom panel, shows the combination of MLEs from Ku- and Ka-band, and 10,19, and 37 GHz AV-H..... 86

Figure 6.6: SST impact on OVW retrieval ..... 87

Figure 6.7: Retrieval skill and ambiguities ..... 88

Figure 6.8: Retrieval skill vs wind speed..... 89



## LIST OF TABLES

Table 2.1: Scatterometer Missions and their Instrument Characteristics .....	13
Table 2.2: GPM DPR Instrument Characteristics.....	22
Table 2.3: GMI Instrument and Performance Characteristics .....	23
Table 4.1: The Spectral Coefficients of GMI Wind Speed Retrieval Algorithm .....	69

# CHAPTER 1: INTRODUCTION

## 1.1: Background

Ocean surface vector wind (OVW) is a crucial parameter for an extensive range of operational and scientific applications, including numerical weather prediction (NWP) and climate studies [1]–[3]. OVW is one of the main drivers of ocean circulation, and it affects the transfer and distribution of heat and moisture fluxes, and thereby, it regulates the evaporation, convection, precipitation, and the overall hydrological cycle that shapes the large-scale atmospheric circulation and global climate [4], [5]. This is why the Global Climate Observing System (GCOS) science panels of the World Meteorological Organization (WMO) recognized OVW as one of the Essential Climate Variables (ECVs) [5], [6].

Satellite-based instruments have been providing OVW measurements on a global scale for the last four decades which has significantly improved our knowledge of the Earth's climate and weather patterns. However, almost all the present and past satellite OVW sensors, except the RapidScat [7], have been in Sun-synchronous polar orbits. Their temporal resolution has therefore remained insufficient for many applications [2]. The Ocean Vector Wind Science Team (OVWST), which coordinates the international OVW community and relevant data products from Earth-observing satellite missions, recommends at least one scatterometer in a non-sun-synchronous orbit with a minimum of two others in sun-synchronous orbits with different crossing times of a day [1]. RapidScat was the first scatterometer in a non-sun-synchronous equatorial orbit, but it existed only for ~2 years [7].

Many studies have reported strong diurnal and semi-diurnal variability of tropical vector winds that may affect cloud formation and precipitation in the tropics [8]–[12]. The diurnal

variability of OVW affects the vertical mixing and exchange of heat and gases between the atmosphere and ocean [12]. These signals create a bias between scatterometer wind observations during ascending and descending passes, thus affecting the cross-calibration between satellite scatterometers with different local crossing times. Therefore, removing this bias is necessary to create a long-term climate-quality intercalibrated dataset [13]. Understanding the diurnal variability of ocean surface vector wind is essential for comprehending the fundamental mechanism of diurnal variability of precipitation and air-sea interaction in the tropics and other regional and global climate studies. However, accurate assessment of diurnal winds has been a long-standing challenge because all the present and past satellite scatterometers, except the RapidScat on the International Space Station, have been in sun-synchronous polar orbits, resulting in sampling a given geographical position twice daily (separated by 12 h), which is insufficient to determine tropical winds' diurnal and semi-diurnal cycles [12]. RapidScat was the first scatterometer in a non-sun-synchronous orbit that provided full diurnal sampling and demonstrated the importance of diurnal sampling [14]–[16]. However, this mission existed only for ~2 years (September 2014 to August 2016). GPM, being in a non-sun-synchronous orbit (65° inclination) [17], may fill this gap with a proper OVW retrieval algorithm besides precipitation measurements.

The Global Precipitation Mission (GPM) launched in February 2014 [18], [19], and the GPM Core Observatory has operated in a non-sun-synchronous orbit (407-km altitude and 65° inclination) as a follow-on mission to the Tropical Rainfall Measuring Mission (TRMM), which provided more than 17 years of valuable microwave observations before ending in April 2015, also from a similar non-sun-synchronous orbit (401-km altitude and 35° inclination) [20]. The GPM-CO has a very well calibrated passive multifrequency microwave imager (GMI) and an

active dual frequency (Ku and Ka-band) precipitation radars (DPR). The GMI is a conical scanning passive radiometer, while the DPR is an active radar cross-track scanner. Both were designed as complementary instruments to determine the 3D structure of global precipitation in  $\pm 65^\circ$  latitudes [21]. Although neither of these instruments is optimum for OVW measurements, each has a robust vector wind (both wind speed and direction) sensitivity. This will be further discussed in Chapter 3 and 4.

The ocean surface normalized radar backscatter, known as  $\sigma^0$ , is biharmonic with wind direction relative to the radar azimuth. This nature of radar return requires multiple azimuth views of the same wind vector cell (WVC) to obtain an unambiguous OVW solution in the inversion. For this, conventional scatterometers employ multi-look antenna system, either in fixed fan beam [22] or rotating pencil beam [23], or rotating fan beam [24] structure (see Chapter 2 for more details). But GPM DPR, both Ku- and Ka-band radar has only a single look, they scan cross track to the flight direction. So, an unambiguous OVW solution is not possible only from DPR. Moreover, the incidence angle range of DPR (-18 degree through 18 degree) while suitable for obtaining 3D rain profile, it is not optimum for OVW measurement. Some recent studies, nevertheless, showed the scalar wind measurement from GPM DPR [25], [26] is possible with reasonable accuracy ( $< 2$  m/s). However, vector wind retrieval from GPM DPR has not been possible so far. Onboard GPM-CO, there is GMI which scan the same WVC conically with a different azimuth view. So, both can be combined to obtain an essential azimuth diversity to resolve the ambiguity problem. This is further illustrated in Chapter 2.

Linearly polarized microwave radiometers have also been limited to providing scalar winds only. Wentz [27] first demonstrated that linearly polarized brightness temperature ( $T_B$ )

observations from the SSM/I contain wind direction (WD) information. However, due to strong atmospheric interference, the use of both V- and H-pol  $T_B$ s for measuring wind direction has not been successful. Meissner and Wentz [28] showed that the polarization combination  $2T_{BV} - T_{BH}$  is almost insensitive to atmospheric fluctuations. Soisuvarn et al. [29] used a more rigorous approach to show that the linear combination of  $T_{BV}$  and  $T_{BH}$ , expressed as  $AVH = (A * T_{BV} - T_{BH})$ , where A was derived from the Advanced Microwave Scanning Radiometer (AMSR)  $T_B$ s using radiative transfer theory, results in an improved "ocean-signal" to "atmosphere-noise" ratio. This approach demonstrated the possibility of OVW measurement from linearly polarized  $T_B$ s using polarized combinations. However, the performance of OVW retrieval for wind speeds less than 10 m/s was not satisfactory. Thus, several other studies have attempted to combine active and passive instruments to measure OVW [30]–[33].

In this dissertation, we demonstrate GPM's vector wind measurement potential by combining its active and passive measurements, which offer the opportunity to create a long-term OVW data product. Flying in a low-earth, non-sun-synchronous orbit, GPM provides a full diurnal global ocean sampling in  $\pm 65^\circ$  latitude in less than two months. Therefore, OVW measurements from GPM will significantly facilitate the in-depth analysis of regional and global diurnal variability of ocean winds.

## 1.2: Aim and Overview of the Dissertation

Therefore, the objective of this dissertation are as follows:

- To investigate the potential for obtaining operational OVW measurements from the GPM Core satellite,

- Perform statistical analysis of 6 years of observations of GPM active and passive instruments to characterize their OVW signature,
- Develop active and passive ocean surface geophysical model functions (GMFs) for Dual-frequency Precipitation Radar (DPR) backscatter and Multi-frequency GPM Microwave Imager (GMI) brightness temperature,
- Develop a combined active and passive microwave OVW retrieval algorithm, and
- Validation of OVW retrievals with ASCAT scatterometer and ERA-5 numerical weather model winds.

### 1.3: Organization of the dissertation

Chapter 1 discusses the background and goals of this dissertation. In Chapter 2, the state-of-the-art of active, passive, and combined active/passive ocean wind vector measurement instruments and techniques are discussed. The characteristics and scan geometries of the GPM sensors are also provided in the context. The development of active geophysical model functions (GMFs) at Ku- and Ka-band is described in Chapter 3. These GMFs characterize the wind speed dependence and azimuthal anisotropy of Ku- and Ka-band  $\sigma^0$  over an EIA range of  $\pm 18^\circ$ . SST effects on the  $\sigma^0$  GMFs are evaluated. In Chapter 4, passive GMI geophysical model functions (GMFs) are described for 3 difference frequency bands. The passive GMFs use the modified 2<sup>nd</sup> Stoke's parameter (a linear combination of V and H-pol  $T_B$ s) to mitigate the atmosphere and enhance the anisotropic WD signal superimposed on GMI  $T_B$ s. Chapter 5 describes the combined active and passive ocean vector wind (OVW) retrieval algorithm that uses DPR and GMI measurements and GMFs in a maximum likelihood estimation procedure to infer wind speed and wind direction. The OVW retrieval algorithm was validated in Chapter 6 by comparing retrievals

with collocated ERA5 reanalysis and Advanced Scatterometer (ASCAT) vector wind data products. The statistics of WS and WD retrieval accuracy performance are presented. Finally, Chapter 7 concludes the dissertation with a summary of the significance and possible applications of this dissertation. It also provides directions for potential future research.

## **CHAPTER 2: MICROWAVE REMOTE SENSING OF OCEAN VECTOR WINDS**

### 2.1: Introduction

The history of microwave remote sensing began with the emergence of microwave radar technology during World War II, where radar backscatter was observed to be correlated with wind speed, wave height, and radar azimuth [34], [35]. Prof. R. K. Moore was the first to envision the potential of this technology for ocean studies, and in the late 60s, he collaborated with notable oceanographer Prof. Willard J. Pierson on radar remote sensing of ocean waves [36]. In the early 70s, research was carried out that built the foundation for space-based remote sensing. NASA's SeaSat-A, launched in July 1978, was the first satellite mission for oceanographic applications that carried a scatterometer, the SeaSat-A Satellite Scatterometer (SASS), for OVW measurement [37]. Since then, many satellite missions have flown that carry various active and passive instruments with diverse capabilities to provide a continuous OVW data record.

Active microwave instruments -- scatterometers, altimeters, synthetic aperture radars (SARs), etc., are radar-based devices that measure the ratio of the backscattered microwave signal to the transmitted signal. Passive microwave instruments -- radiometers, measure, on the other hand, the polarized absolute blackbody emission from the Earth's surface and atmosphere.

Radar scatterometers have been the primary choice for vector wind measurement because of the sensitivity of their geophysical model function to the ocean vector wind parameter and the lack of sensitivity to other atmospheric and oceanic physical parameters [5]. Nevertheless, microwave radiometers have also been providing scalar winds since 1987, and since 2003, the first space-based polarimetric radiometer, WindSat, has provided comparable (to scatterometer) vector



wind measurements [38], [39]. Although the primary purpose of microwave altimeters is measuring sea-surface height, it has also contributed to the space-based monitoring of scalar winds. But they have a narrow swath near the nadir and offer minimal spatial coverage. SARs are high-spatial resolution imaging radars, but the lack of repeating spatial coverage on a daily basis has limited their utility for operational measurements. Nevertheless, they have found limited applications for monitoring ocean winds with kilometer-scale spatial resolution, which are more suitable for some applications, like coastal remote sensing. Further, their vector wind capability is currently under research [40].

In addition, there are different categories of instruments, like NASA's Soil Moisture Active Passive (SMAP), that employ both active radars and passive radiometers to measure other geophysical parameters (soil moisture and ocean salinity); but they have demonstrated the capability of OVW measurements as secondary products [41]–[44]. The GPM is a similar mission that carries dual-frequency precipitation radars and a multi-frequency microwave radiometer for precipitation measurements, and this dissertation investigates developing GPM's OVW measurement capability. This Chapter provides a quick review of the active and passive OVW technologies. In the following section, we will discuss the GPM instrument characteristics from the perspective of these.

## 2.2: Active Measurement of Ocean Vector Wind

Active ocean vector wind measurement is based on the radar principle -- active instruments transmit microwave electromagnetic pulses and detect the reflected or the backscattered signal. The received power by a monostatic radar (using the same antenna for transmission and reception) receiver can be computed by the so-called radar equation,

$$P_r = \left\{ \left( \frac{P_t G}{4\pi R^2} * \sigma \right) * \frac{1}{4\pi R^2} \right\} * A_e = \left\{ \left( \frac{P_t G}{4\pi R^2} * \sigma \right) * \frac{1}{4\pi R^2} \right\} * \frac{\lambda^2 G}{4\pi} = \left[ \frac{P_t G^2 \lambda^2}{(4\pi)^3 R^2} \right] * \sigma, \quad \text{watts} \quad (2.1)$$

where,  $P_t$  is the transmitted power in watts,  $G$  is the gain of the radar antenna,  $A_e$  is the effective aperture area of the antenna ( $m^2$ ), which in turn is determined by the antenna gain and wave length,  $\lambda$  of the incident wave (m),  $R$  is the distance between the radar and ocean surface (spacecraft altitude in meters), and  $\sigma$  is the radar cross section in square meters. The first term in Eq. 2.1 then represents the incident flux at the ocean surface. Incident flux times the effective target scattering area ( $\sigma$ ) is the backscattered power by the ocean surface. Finally, the proportion of the backscattered flux intercepted by the radar antenna back is determined by the effective aperture area of the antenna.

From Eq. 2.1, the definition of the radar cross section can be derived.

$$\sigma = \frac{\text{backscattered power per unit solid angle}}{\text{incident power density}/4\pi} \propto \frac{|E_{\text{backscatter}}|^2}{|E_{\text{incident}}|^2} \quad (2.2)$$

where  $E_{\text{backscatter}}$  and  $E_{\text{incident}}$  are the backscattered and incident electric field intensity respectively.

Note, radar backscatter is a property scattering object alone, and it is a measure of the ratio of received power to the transmitted power. The normalized radar cross section (NRCS) is defined as the average radar cross-section over radar's instantaneous field of view (IFOV),

$$\sigma^0 = \frac{\sigma}{\text{Pulse IFOV}} \quad (2.3)$$

Now, for the pulse limited footprint (IFOV), the expression for can derived as:

$$\sigma^0 = \left[ \frac{(16\pi)^2 \cos \theta_i}{G^2 \lambda^2 \beta^2} * R^2 * \frac{P_r}{P_t} \right] \propto \frac{P_r}{P_t} \quad (2.3)$$

where  $\theta_i$  is the incidence angle and  $\beta$  is the beamwidth of the pulse, and both are known from instrument geometry. So, measuring  $\sigma^0$  reduces to making a relative power measurement (i.e.,  $\frac{P_r}{P_t}$  in watts).  $\sigma^0$  depends on the physical and electrical properties of the target with respect to the radar sensor's frequency, polarizations, incidence, and azimuth angle.

The actual ocean surface is not smooth; the surface (air drag) friction between winds and the ocean surface transfers atmospheric wind momentum that causes multi-scale roughness (small-scale ocean waves).  $\sigma^0$  at microwave frequency is a strong function of small-scale (centimeter to decimeter) capillary waves that are superimposed on larger-scale gravity waves (on the order of meters) as illustrated in Figure 2.1a. These centimeter-scale capillary waves, which are periodic but asymmetric, interact with electromagnetic radiation of the wavelength of similar orders in a fashion that involves multiple mechanisms [45], [46]. As a result, the  $\sigma^0$  vary as a function of wind speed and wind direction such that higher wind speed causes higher roughness that results in larger  $\sigma^0$ .

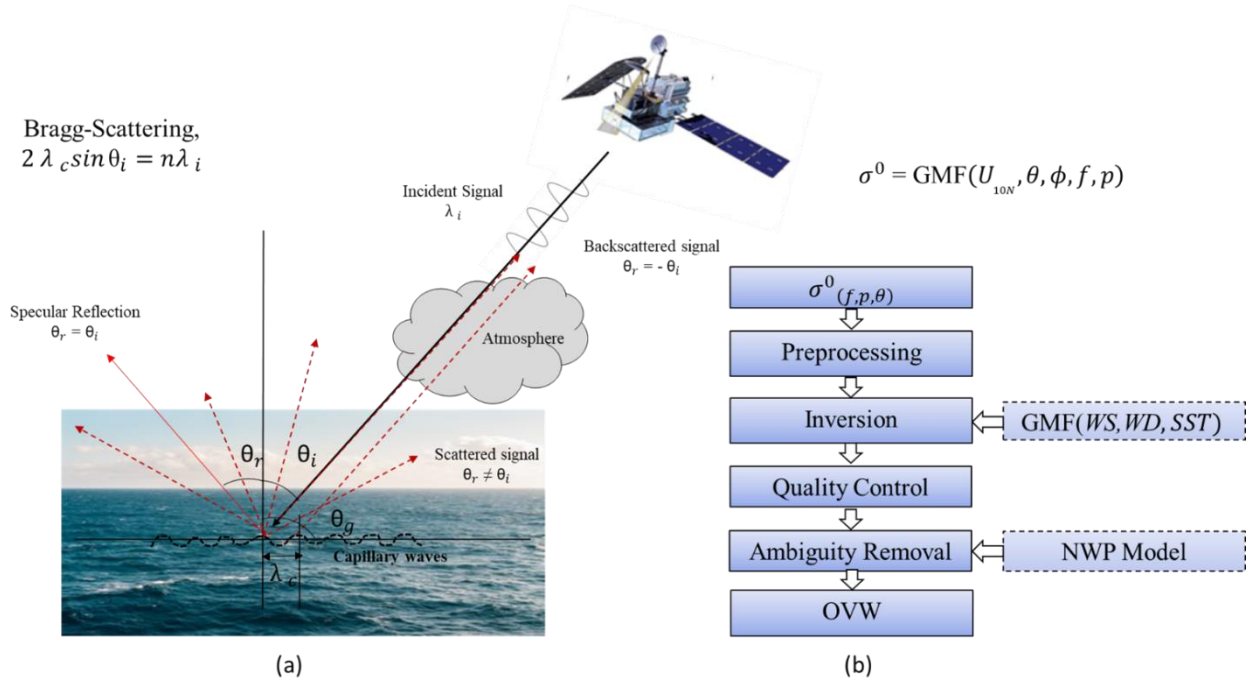


Figure 2.1: Basic principle of active remote sensing, (a) ocean surface backscattering, (b) wind retrieval algorithm

Depending on the angle of incidence, Bragg scattering is the most dominant mechanism for wind-induced ocean surface roughness for the microwave frequency of interest [47], [48]. Mathematically, the condition for Bragg resonance is given by,

$$2 \lambda_c \sin \theta_i = n \lambda \quad (2.3)$$

where  $\lambda$  and  $\lambda_c$  are the wavelength of incident radar signals and small-scale ocean surface capillary waves,  $\theta_i$  is the incidence angle, and  $n$  is a positive integer number (major radar backscatter comes from  $n = 1$  [46]). As seen from Eq. 2.3, for a particular microwave frequency, the Bragg resonance is limited to a critical incidence angle, but there is a continuum of ocean wavelengths in the roughness spectrum that results in effective Bragg scattering over a wide range of incidence angles. For example, conventional Ku-band and C-band scatterometry generally uses the incidence angle

range between  $20^\circ \leq \theta_i \leq 70^\circ$ , where the upper bound is also determined by the requirement of a reliable signal-to-noise ratio (SNR). For a lower incidence angle (near nadir), the Bragg scattering becomes weak, and quasi-specular reflection becomes gradually dominant with a transition region in between [49]–[51].

### 2.2.1: Geophysical Model Function (GMF)

The empirical relation between  $\sigma^0$  and wind speed and direction relative to the azimuth for a particular frequency, incidence angle, and polarization is conventionally called the Geophysical Model Function (GMF). Some other secondary factors, like sea surface temperature, wave heights, etc., do affect the GMF to limited extent, so they are also considered accordingly. Although some analytical relation for GMF exists, GMFs are usually developed empirically or semi-empirically (physics-based) for better reliability.

$$\sigma^0 = \text{GMF}(U_{10N}, \theta, \phi, f, p) \quad (2.4)$$

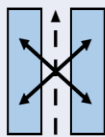

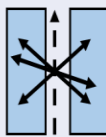

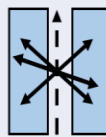


where  $U_{10N}$  is the equivalent neutral stability wind speed in m/s at 10-meter height [52], [53] (see APPENDIX A for more about neutral stability wind  $U_{10N}$ ),  $\theta$  is Earth incidence angle (deg.),  $\phi$  relative wind direction (deg.),  $f$  is the signal frequency (GHz), and  $p$  is the polarization of the signal.

### 2.2.2: Scatterometer Characteristics

There have been many scatterometer missions since the launch of the SeaSat SASS in 1978. Some of the major instruments and their major characteristics are summarized in Table 2.1 below. In terms of frequency bands, there have been two major complementary bands used in all the instruments so far – the Ku-band (~14 GHz) and the C-band (~5 GHz) scatterometers. The National Aeronautics and Space Administration (NASA) scatterometers have historically been using the Ku-band (from SeaSat to RapidScat). In contrast, the European Space Agency (ESA) has

predominantly used the C-band scatterometers (AMIs on ERS-1 and -2, ASCATs onboard MetOp-A, -B, and -C satellites). Both bands have their relative merits and shortcomings [35], [54]. Ku-band scatterometers have higher wind sensitivity. However, they are more sensitive and affected by rain and other atmospheric contaminations.

Table 2.1: Scatterometer Missions and their Instrument Characteristics

Characteristics	SASS SEASAT	AMI ERS-1, -2	NSCAT ADEOS-1	QuikSCAT ADEOS-1, -2	ASCAT METOP-A, -B, -C	RapidSCAT ISS	HY-2A, -2B, -2C SCAT
Lifetime	6/1978 – 10/1978	8/1991-1/2001	8/1996-6/1997	6/1999-11/2009	2006-present	9/2014-11/2016	10/2018-present
Band (Freq, GHz)	Ku (14.6)	C (5.3)	Ku (13.99)	Ku (13.4)	C (5.25)	Ku (13.4)	Ku (13.4)
Polarization	V-H, V-H	V-V	V-V, V-H, V-H	V-V, H-H	V-V	V-V, H-H	V-V, H-H
EIA (deg)	22°-55°	18°-47°, 24°-57°	18°-57°, 22°-63°	46°, 54°	25°-65°	49°, 56°	41°, 48°
Spatial Res (km)	50	50	25	25/12.5	25	25/12.5	25
Swath width (Km)	500x2	500	600x2	<b>1410, 1800</b>	550x2	900, 1100	1700
Scan Configuration	Fan beam	Fan beam	Fan beam	Pencil Beam	Fan beam	Pencil Beam	Pencil Beam
Daily Coverage (%)	Variable	41	77	93	65	51	>90
Orbit	Sun Synchronous	Sun Synchronous	Sun Synchronous	Sun Synchronous	Sun Synchronous	<b>Non-sun-synchronous</b>	Sun Synchronous
Scan Pattern							

On the other hand, C-band scatterometers are less impacted by rain. But they have less wind sensitivity for lower and higher wind conditions. Another significant difference arises from the scan geometries of the instruments. All initial Ku-band scatterometers and all C-band scatterometers have used fixed fan-beam configuration that uses static antennas at multiple azimuth directions on each side of the swath to resolve directional ambiguities [55]. Fan-beam antennas use single or dual polarizations and variable incidence angles, avoiding near nadir range

that leaves a nadir gap at the middle of the swath. Although fan-beam instruments provide a homogenous quality wind over the entire swath, the nadir gap poses a problem in daily coverage. With the launch of the SeaWinds scatterometer aboard the QuikSCAT satellite, NASA set up a new design, a conically scanning pencil-beam antenna configuration [56], that filled the nadir gap and resulted in a very wide swath that provided almost a global coverage in a single day. But the quality of the winds depends on the position of the swath, with better quality in the “sweet swath” in the middle and poor quality over the nadir and far swath where azimuth diversity is poor. Later, scatterometers by NASA (RapidScat [7], [57]) and other agencies (HSCAT on HY-2 satellite series by the China National Space Administration (CNSA) [58], [59], OSCAT series by Indian Space Research Organization (ISRO)) followed a similar configuration to continue the legacy [54], [60], [61]. Recently, unlike either fixed fan-beam or rotating pencil-beam configuration, a new design called the rotating fan-beam structure has been employed in China-France Oceanography Satellite (CFOSAT) scatterometer (CSCAT) [24], [62], [63]. It is expected to provide better-quality winds by taking advantage of both the rotating pencil-beam and fixed-fan beam scatterometers [24].

### 2.2.3: OVW Retrieval Algorithm

The ocean vector wind retrieval procedure, as shown in Fig. 2.1b, usually starts with preprocessing of  $\sigma^0$  measurements include calibration, gridding, and filtering for non-wind conditions such as ice, land, etc., followed by the inversion, where the measurement is compared with trial wind speed and direction with the help of a pre-tuned GMF. This inversion is usually non-linear, and thus non-linear optimization technique such as the maximum likelihood estimation (MLE) is used [64]. Due to the biharmonic nature of  $\sigma^0$  with wind direction, multiple ambiguous

vector wind solutions result from the inversion. Then an appropriate ambiguity removal (AR) algorithm, which is initialized with an analytic wind field from the numerical weather prediction (NWP) model (called ‘nudging’), to select the best OVW solution, ensuring the spatial and metallurgic consistency [65], [66].

### 2.3: Passive Measurement of Ocean Scaler and Vector Wind

Passive remote sensing of ocean surface winds relies on the principle of microwave radiometry. A part of the total energy received by the Earth’s atmosphere from the sun and cosmic background in the form of electromagnetic radiation is scattered and absorbed by it. The rest is transmitted toward the Earth’s surface, where it is further scattered and absorbed. According to the thermodynamic principle, the absorption of electromagnetic energy is followed by the rise in temperature, and under thermal equilibrium, the absorption rate equals the emission rate. The spectral brightness intensity,  $I_f$ , due to the emission by the Earth’s surface is determined by Planck’s quantum theory of blackbody radiation [47],

$$I_f = \frac{2hf^3}{c^2} \left( \frac{1}{e^{hf/kT} - 1} \right) \quad (2.5)$$

where  $h$  is Planck’s constant (joules),  $k$  is Boltzmann’s constant (joules/K),  $f$  is the frequency (Hz),  $c$  is the speed of light in vacuum (m/s), and  $T$  is the absolute physical temperature (K). The unit of is given in  $Wm^{-2}sr^{-1}Hz^{-1}$ .

For the microwave region of the electromagnetic spectrum, where  $hf/kT \ll 1$ , Eq. (2.5) can be well approximated by Rayleigh-Jean’s law, which simplifies Planck’s law as follows:



$$I_f \approx \frac{2kT}{\lambda^2} \quad (2.6)$$

Now, if a polarized antenna with an effective receiving aperture area  $A_r$  and radiation pattern  $F(\theta, \phi)$ , surrounded by a blackbody with brightness intensity given by Eq. (2.6), the total power received by the antenna can be provided by,

$$P = \frac{1}{2} A_r \int_{f_1}^{f_2} \iint_{4\pi} \frac{2kT}{\lambda^2} F(\theta, \phi) d\Omega df \quad (2.7)$$

If the receiver is bandlimited by a narrow bandwidth  $B$ , and is approximately constant over the bandwidth, Eq. (2.7) simplifies to,

$$P = \frac{kTBA_r}{\lambda^2} \iint_{4\pi} F(\theta, \phi) d\Omega = kT_B(\theta, \phi)B \quad (2.8)$$

where  $\iint_{4\pi} F(\theta, \phi) d\Omega = \frac{\lambda^2}{A_r}$  is the solid angle subtended by the antenna pattern, and  $T_B(\theta, \phi)$  is the blackbody equivalent radiometric brightness temperature or the material's brightness temperature. The brightness temperature,  $T_B(\theta, \phi)$ , is related to the physical temperature  $T$  of the material by its emissivity such that [47], [67]:

$$T_B(\theta, \phi) = E(\theta, \phi) T \quad (2.9)$$

where the  $T$  is the physical temperature of the material for the ocean surface; it is the sea surface temperature (SST,  $T_S$ ). The  $\theta$  and  $\phi$  within the parenthesis indicate the brightness temperature,  $T_B$ , is a function of incidence and azimuth angle. It is also a function of the frequency and polarization of the signal used. For simplicity, we will use,  $T_B$ , to represent the brightness temperature, and  $E$  to indicate the surface emissivity.

Figure 2.2 illustrates the radiative transfer process and passive microwave remote sensing of ocean surface winds. Since the microwave reflectivity  $R$  is a function of wind-induced ocean surface roughness, the emissivity,  $E$ , is also the function of the same, according to Kirchhoff's law:

$$E + R = 1 \tag{2.10}$$

Brightness temperature ( $T_B$ ) from multifrequency microwave radiometers are inverted to retrieve different environmental parameters including ocean winds [38]. Spectral combinations of  $T_B$  measurement is usually utilized.

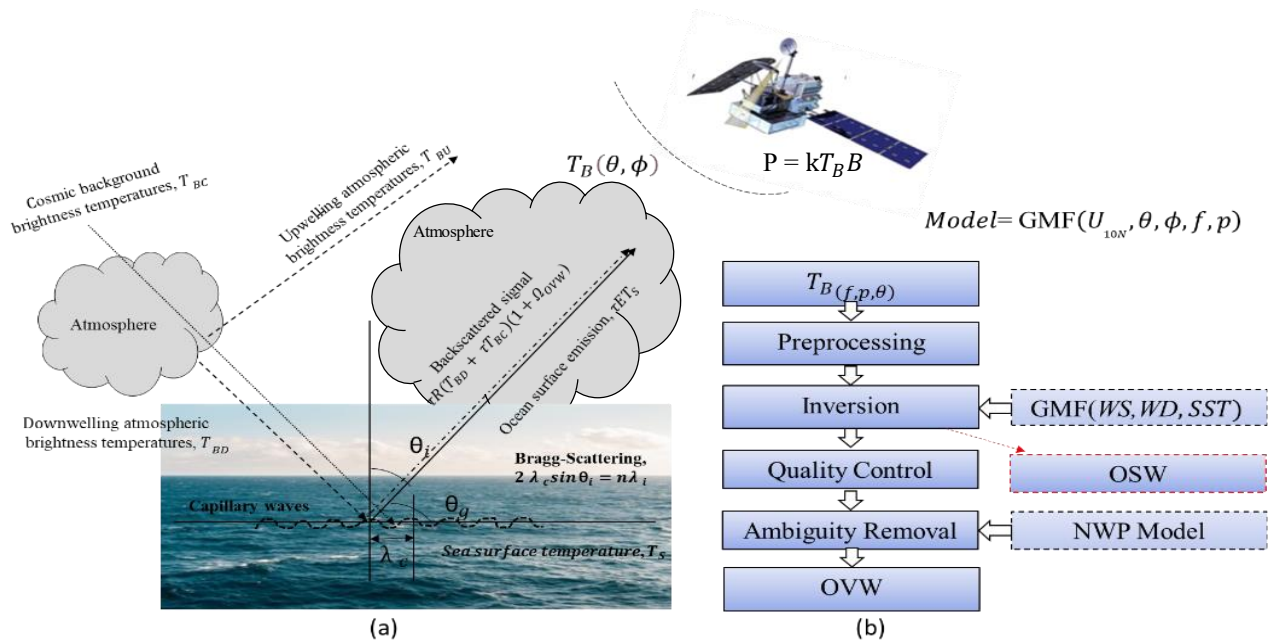


Figure 2.2: Basic principle of passive remote sensing, (a) ocean surface scattering, (b) wind retrieval algorithm

Microwave radiometers began measuring ocean surface scalar wind at the same time as microwave scatterometers with the launch of the Scanning Multichannel Microwave Radiometer (SMMR) on board the SeaSat satellite in 1978. When SeaSat failed, the second SMMR instrument on the Nimbus-7 spacecraft, launched at the same time, continued the wind speed measurements.

The operational measurement of ocean surface scalar winds began in 1987 with the launch of the Special Sensor Microwave/Imager (SSM/I) series by the US Department of Defense (DoD) and the National Oceanic and Atmospheric Administration (NOAA) as part of the Defense Meteorological Satellite Program (DMSP) [13]. The DMSP SSM/I (later the SSMIS, the Special Sensor Microwave Imager/Sounder) series has continued the legacy to date, launching 10 more follow-up sensors. Other agencies, including NASA and the Japan Aerospace Exploration Agency, have also launched microwave radiometers that have provided long-term ocean scalar data records.

However, the majority of radiometers launched so far (with the exception of WindSat and the recently launched Compact Ocean Wind Vector Radiometer, or COWVR [68], aboard the International Space Station) have been designed as total power radiometers, which measure only the magnitude of the electromagnetic radiation in a specific polarization direction, usually the vertical (V) or horizontal (H) polarization. This design allows for high accuracy and precision with a simpler design, but it is limited in its ability to provide a complete characterization of the polarization states. Consequently, retrieval of wind direction information has not been possible from these radiometers.

On the other hand, a fully polarimetric radiometer is capable of measuring all four components of the polarization state of the incoming radiation: the horizontal and vertical components, as well as the two circular components (left-handed and right-handed). These four components are collectively known as the Stokes vector and are given by [69]:

$$I_s = \begin{bmatrix} I \\ Q \\ U \\ V \end{bmatrix} = \begin{bmatrix} T_V \\ T_H \\ T_{45} - T_{-45} \\ T_{LC} - T_{-RC} \end{bmatrix} = [\langle E_V E_V^* \rangle] \begin{bmatrix} \langle E_V E_V^* \rangle \\ \langle E_H E_H^* \rangle \\ 2\text{Re}\langle E_V E_H^* \rangle \\ 2\text{Im}\langle E_V E_H^* \rangle \end{bmatrix} \quad (2.11)$$

Stoke's vectors facilitate the complete characterization of the polarization states of radiation and enable vector wind measurement. In the 1990s, numerous research efforts were focused on passive polarimetric remote sensing [69]–[72], laying the foundation for the first space-borne fully-polarimetric microwave radiometer, WindSat, which was developed by the U.S. Navy and the National Polar-orbiting Operational Environmental Satellite System Integrated Program Office (NPOESS IPO) and launched aboard the US DoD satellite Coriolis in 2003 [38], [39]. WindSat not only demonstrated the proof-of-concept of space-based passive fully-polarimetric remote sensing of ocean vector winds, but it also provided an uninterrupted operational and scientific data record through 2020. Although it has its own relative advantages and limitations compared to scatterometer wind products, the accuracy of the latest version of its vector wind data product is very close to that of the QuikSCAT vector wind data product for winds greater than 6 m/s [1], [73], [74]. WindSat also provided other environmental parameters, including sea surface temperature (SST), rain rate (RR), water vapor (WV), cloud liquid water (CLW), and more [75]. Despite the success of the WindSat mission, there have been no similar fully-polarimetric microwave radiometers in the last two decades.

Recently, NASA's Jet Propulsion Laboratory launched an upgraded version of WindSat, called the Compact Ocean Wind Vector Radiometer (COWVR), aboard the ISS as a technology demonstration of the next generation instrument. The COWVR reduced the size and cost by simplifying the design [68]. Although the mission is currently operational, as of the writing of this dissertation, the dataset has not been publicly available.

#### 2.4: Combined Active and Passive Measurement of Ocean Vector Wind

In addition to the specialized OVW measurement missions, there have been missions that measured other land and ocean parameters such as soil moisture (SMAP) and ocean surface salinity (Aquarius). These missions carried complementary radar instruments with radiometers onboard the same spacecraft. For example, NASA launched the Aquarius mission to measure ocean surface salinity, which carried an L-band radar scatterometer and an L-band radiometer [76]. The purpose of the scatterometer was to correct wind-induced roughness effects on salinity measurements by the radiometer. In [76]–[78], Yueh et. al. showed that the L-band radar and radiometer measurements could potentially be combined to derive combined OVW and salinity products. Following this, Fore et al. [42] at JPL retrieved combined active/passive (CAP) OVW and salinity products from the SMAP mission, which carried similar L-band active and passive instruments to measure primarily soil moisture. Although the individual L-band sensors are not as effective as Ku or C-band sensors for lower wind speed regimes, the SMAP CAP OVW retrieval performance is comparable to QuickScat/RapidScat for lower wind speeds, and even better for higher wind speeds ( $>12.5$  m/s) [42]. It is important to note that the radar instrument onboard SMAP was a conical scanning scatterometer with forward and aft azimuth looks, and the radiometers were capable of measuring the third and fourth Stoke's parameters.

#### 2.5: Global Precipitation Measurement Mission

The GPM Core Observatory (shown in Fig. 2.3) was launched in February 2014 by NASA and JAXA and is in a 407-km circular non-sun-synchronous orbit with a  $65^\circ$  inclination around the Earth. It was designed as an upgraded follow-up mission of the Tropical Rainfall Measuring Mission (TRMM) primarily for measuring precipitation [79]. In addition to precipitation, other

environmental products such as sea surface temperature (SST), columnar water vapor (WV), and columnar cloud liquid water (CLW) have also been available from the GPM observatory [80].

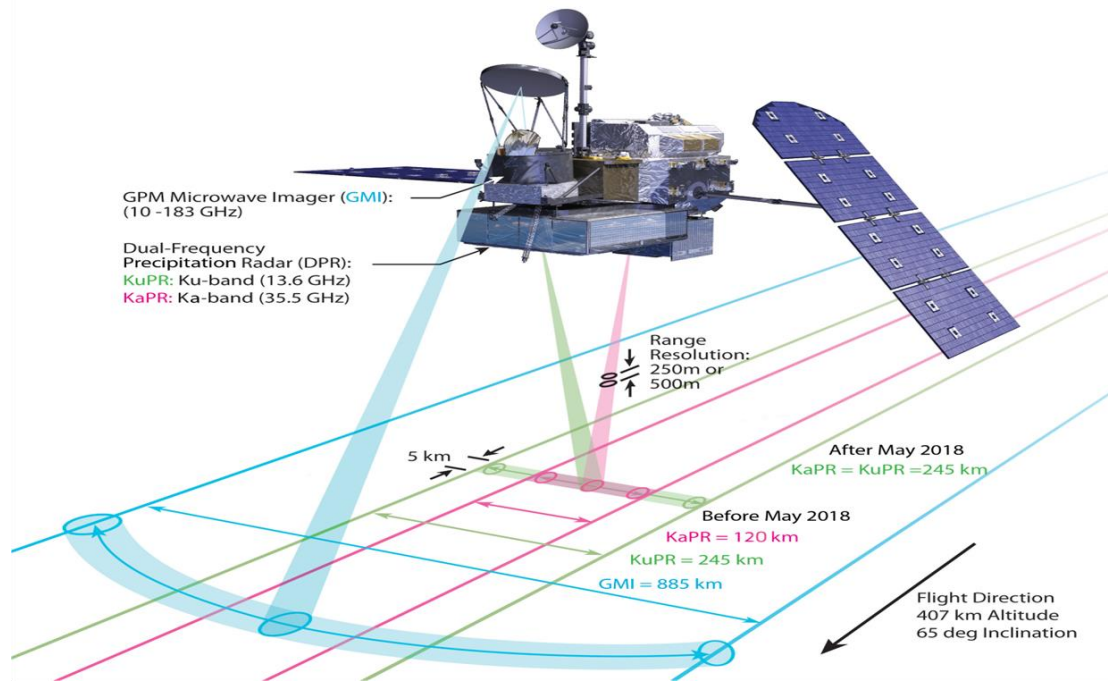


Figure 2.3: GPM core observatory and its sensors (Credits: NASA Global Precipitation Measurement Mission)

## 2.5.1: GPM Instruments

### 2.5.1.1: GPM Dual-Frequency Precipitation Radar (DPR)

The GPM DPR is equipped with two precipitation radars (PR) operating at Ku-band (13.6 GHz) and Ka-band (35.5 GHz), both utilizing horizontal-polarized signals. Cross-track measurements are performed using separate phased array antennas, resulting in 49 contiguous and coincident narrow instantaneous field of view (IFOV) beam positions covering an Earth incidence angle (EIA) range of  $\pm 18^\circ$ . These beams are separated by approximately  $0.75^\circ$  in EIA, producing a spatial footprint of around 5 km in diameter that generates a common 245 km swath at the center of the GMI swath, as depicted in Fig. 2.3. However, initially, the Ka-band swath was limited to

120 km because the outer 24 beams (12 on each side) were interleaved with the central 25 coincident beams until being reconfigured for full 49-beam coincident measurements over the entire 245 km swath on May 21, 2018 [81]. The detail instrument characteristics of GPM DPR are given in Table 2.2.

Table 2.2: GPM DPR Instrument Characteristics

Instruments	KuPR	KaPR
Frequency (GHz)	13.6	35.5
Antenna type	Active phased array (128)	Active phased array (128)
Swath width (Km)	245	245 (125 before May 2018)
Horizontal Res at nadir (Km)	5.2	5.2
No of cross track beams	49	49
EIA (deg)	$0 \pm 18$	$0 \pm 18$
Range resolution (m)	250	250/500
Transmitter pulse width ( $\mu$ s)	1.6	1.6/3.2
PRF (kHz)	$4.2 \pm 0.1$	$4.2 \pm 0.1$
Measurement Accuracy (dBZ)	$< \pm 1$	$< \pm 1$

#### 2.5.1.2: GPM Microwave Imager (GMI)

The GMI is a well-designed and well-calibrated total power microwave radiometer that utilizes 13 radio frequency channels (10V/H, 19V/H, 23V, 37V/H, 89V/H, 166V/H, 183+/-3V, 183+/-8V) to measure  $T_B$  over a 931 km swath [82]–[85]. All channels share a common rotating antenna with conical scanning to provide  $T_B$  measurements, as illustrated in Fig. 2.3. The higher frequency channels (>90 GHz) are primarily used for atmospheric sounding and are less sensitive

to surface parameters, including winds, which is why they were excluded. The 89 GHz and 23V channels were also not used due to their sensitivity to atmospheric water, liquid water, and water vapor. Hence, only the 10, 19, and 37 GHz channels were utilized in this dissertation due to their ability to capture wind vector signatures. The electrical and physical properties, spatial resolution, measurement precision of GMI channels is summarized in Table 2.3.

Table 2.3: GMI Instrument and Performance Characteristics

Ch	Center Freq (GHz)	Pol	Bandwidth (MHz)	Sample Time (msec)	EIA (deg)	Beam Width (deg)	EFOV (Km)	Mean Spatial Res (Km)	On-orbit NEDT (K)
1	10.65	V	96.5	3.6	52.74	1.72	20x32	25	0.77
2	10.65	H	94.7	3.6	52.73	1.72	20x32	25	0.78
3	18.7	V	193	3.6	52.76	0.98	12x18	15	0.63
4	18,7	H	194	3.6	52.76	0.98	12x18	15	0.60
5	23.8	V	367	3.6	52.76	0.85	10x16	13	0.51
6	36.64	V	697	3.6	52.79	0.82	10x15	12	0.41
7	36.64	H	707	3.6	52.79	0.82	10x15	12	0.42
8	89	V	2x2735	3.6	52.78	0.38	6x7	7	0.32
9	89	H	2x2758	3.6	52.78	0.38	6x7	7	0.31
10	166	V	2x1569	3.6	49.11	0.38	6x6	6	0.70
11	166	H	2x1601	3.6	49.11	0.37	6x6	6	0.65
12	183.31 ± 3	V	2x1482	3.6	49.11	0.37	6x5	6	0.56
13	183.31 ±7	V	2x1874	3.6	49.11	0.37	6x5	6	0.47



### 2.5.2: Technical Challenges

The GPM instruments, the GMI and DPR, were not specifically designed for measuring vector winds. Therefore, OVW measurement by these instruments pose some technical challenges. Retrieval of ocean vector winds (OVW) requires observations of the same wind vector cell (WVC) from multiple azimuth directions. As the PRs perform observations with a single look (i.e., cross-track), they alone cannot provide unambiguous OVW retrieval. However, the GMI observes the same WVC with a different azimuth angle, approximately  $\sim 75^\circ$  off the PR view angle, as shown in Fig. 2.4, depending on the latitude. This facilitates the essential azimuth diversity required for removing wind vector ambiguity. Moreover, the nature of the AV-H GMF is different from conventional scatterometer GMF, as it is predominated by the first harmonic, which also helps to reduce the ambiguity problem [86], [87]. Another limitation of the DPR is its incidence angle, which is not optimal for OVW sensing. The inclusion of the Ka-band, which demonstrates higher sensitivity to winds, alleviates this to a great extent [88]. The use of modified second Stokes parameters for passive linearly polarized  $T_{BS}$  (i.e.,  $A * T_{BV} - T_{BH}$ ) helps to mitigate atmospheric noise and enhance the WD signal [89]–[91].

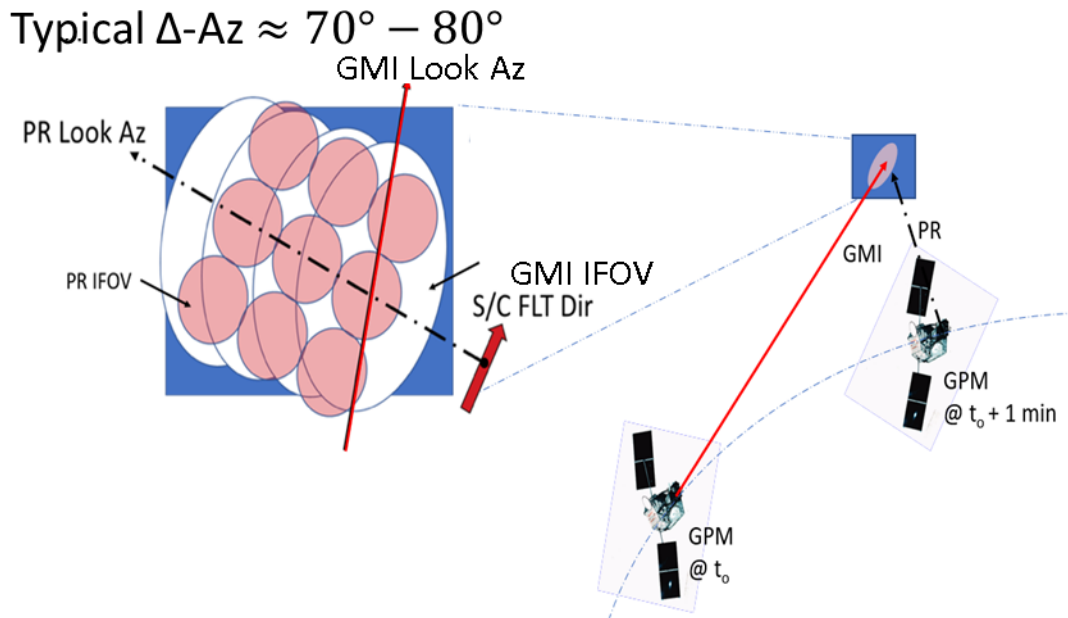


Figure 2.4: GMI and DPR azimuth diversity

In next two chapters, we present a comprehensive statistical analysis of GPM DPR backscatter and multi-frequency GMI brightness temperature ( $T_B$ ) observations, respectively, and characterize their OVW signature as a function of relevant geophysical parameters to derive the corresponding active and passive ocean surface geophysical model functions (GMFs).

## CHAPTER 3: ACTIVE GEOPHYSICAL MODEL FUNCTION

*The contents of this chapter have been published in the following article: Hossan A, Jones WL. Ku- and Ka-Band Ocean Surface Radar Backscatter Model Functions at Low-Incidence Angles Using Full-Swath GPM DPR Data. Remote Sensing. 2021; 13(8):1569. <https://doi.org/10.3390/rs13081569> [92].*

### 3.1: Introduction

A robust geophysical model function (GMF), relating the ocean surface normalized radar cross section (known as  $\sigma^0$ ) and the ocean wind speed and direction, and other possible secondary parameters, like, sea surface temperature, is essential for the development of an accurate ocean vector wind (OVW) retrieval algorithm. The  $\sigma^0$  GMF is also crucial for on-orbit radar calibrating active remote sensors and correcting atmospheric path attenuation in satellite cloud and rain profiling radars [93]. While the literature for ocean  $\sigma^0$  is extensive, most studies concern Ku- and C-band frequencies for either radar scatterometers at moderate earth incidence angles (EIA) or nadir-viewing radar altimeters.

On the other hand, the satellite Ku-band Precipitation Radars (PR) onboard the Tropical Rainfall Measuring Mission (TRMM) [94] and the Ku/Ka-band Dual-frequency Precipitation Radar (DPR) on the follow-on Global Precipitation Mission (GPM) [17], [79], also measure ocean backscatter from space. These radars view the surface at near-nadir EIA, with cross-track scans within nadir to  $\pm 18^\circ$ ; this scenario offers a unique scientific opportunity to investigate air-sea interaction processes as a function of wind and wave parameters from non-sun synchronous, low-earth orbiting satellites. Notable among near-nadir ocean backscatter studies were: Freilich and Vanhoff [49], who established an empirical relation between ocean surface  $\sigma^0$  and wind speed for

EIA  $0^{\circ}$ – $18^{\circ}$  using TRMM Ku PR measurements; Jones et al. [95], and Souisvarn et al. [96], who was the first to characterize the TRMM Ku PR  $\sigma^0$  wind direction anisotropy for EIA  $12^{\circ}$ – $18^{\circ}$  over wind speeds of 3–9 m/s; Li et al. [97], who first demonstrated the wind speed (WS) retrieval from TRMM PR; and finally, Tran and Chapron [98], who first reported the directional anisotropy and sea state dependency of nadir  $\sigma^0$  measurements by Ku- and C-band satellite altimeters and also near-nadir measurements from TRMM PR [10]. More recently, an investigation by Chu et al. [99] provided a comprehensive analysis of near nadir  $\sigma^0$  as a function of combined wind vector and wave parameters (including wave height and steepness) by using a large set of collocated TRMM PR and in situ data. Additionally, Chu et al. [100] discussed the unique behavior the Ku-band  $\sigma^0$  at low incidence angles by analyzing its upwind–downwind asymmetry and upwind–crosswind directional modulations.

Before 2014, the ocean  $\sigma^0$  at Ka-band was based on airborne experiments. Although these radar backscatter measurements provided valuable insights that indicated a similar behavior of Ka-band  $\sigma^0$  to that at Ku-band, the results of various studies were inconsistent with each other [101]. In February 2014, the GPM satellite was launched, with the dual-frequency precipitation radar that provided the first space-based measurements of global ocean radar backscatter at low incidence angles at both Ku- and Ka-bands [19]. Recent studies analyzed these simultaneous GPM DPR  $\sigma^0$  measurements [102], [103]; however, results for Ka-band were limited to EIA of  $\pm 9^{\circ}$  (corresponding to  $\sim 125$  km at the center of collocated Ku swath). Fortunately, on May 21, 2018, the Ka-band was reconfigured to provide fully collocated measurements with Ku PR over the entire  $\sim 250$  km swath corresponding to EIA range of  $\pm 18^{\circ}$  [81].

In addition, Wang et al. [104] performed a comprehensive investigation of sea surface temperature (SST) effects on ocean surface  $\sigma^0$  at the corresponding EIAs and polarizations for C- and Ku-band scatterometers. Although negligible at C band, they concluded that SST effects were significant for Ku band and should be included in the ocean surface  $\sigma^0$  geophysical model function (GMF). Based on their findings, we performed a similar analysis of GPM DPR backscatter measurements at low incidence angles. Results are given herein that document the effects of SST on both Ku- and Ka-band Ocean radar backscatter. To account for the SST effects properly, the SST was included as an independent dimension of the GMF.

Therefore, this chapter presents the comparative results from the full-swath, collocated, GPM DPR measurements, and separate (Ku- and Ka-band) GMFs are described for horizontal-polarization, which characterize the clear-sky, ocean surface  $\sigma^0$  as a function of EIA and environmental parameters—namely, ocean surface wind speed (WS), wind direction (WD), and SST. However, it should be noted that the smooth surface Fresnel reflection coefficient is the same for both H-pol and V-pol at low incidence angles below  $\sim 20^\circ$ . As a result, this dissertation should apply to both linear polarizations.

The chapter is organized as follows: instruments and data are described in section 3.2. In section 3.3, the WS, relative wind direction (RWD), SST dependency of  $\sigma^0$ , and model description are provided. Comparative results at Ku and Ka bands are also given in the same section, which is followed by the discussion in section 3.4.

### 3.2: Methods

The Global Precipitation Mission satellite was launched on 27 February 2014 into a  $65^\circ$  inclination, 407 km altitude, non-sun-synchronous orbit. This is a joint Earth Observation Science

mission by the National Aeronautics and Space Administration (NASA) and the Japan Aerospace Exploration Agency (JAXA), which extends the TRMM time series [94], [89], and enhances the measurement of global precipitation [17], [19], [85]. The satellite carries two microwave remote sensors: a passive GPM microwave imager (GMI) and a dual-frequency precipitation radar (DPR).

### 3.2.1: GPM Dual-Frequency Precipitation Radar (DPR)

As mentioned in Section 2.5, a Ku-band (13.6 GHz, H pol) precipitation radar (KuPR) and a new Ka-band (35.5 GHz, H pol) precipitation radar (KaPR) form the dual-frequency precipitation radar (DPR) onboard the GPM core observatory. The GPM KuPR uses an electronically scanned phased array to scan the surface perpendicularly to the flight direction at 49 beam positions over an EIA  $\pm 18^\circ$ . Contiguous beams are separated by about  $0.75^\circ$  in earth incidence angle, resulting in a spatial footprint of about 5 km in diameter that produces a continuous 245 km measurement swath. The Ka PR also has 49 cross-track beams with the same beam width as Ku PR after May 21, 2018. Initially, only 25 of the Ka-band beams with the same range resolution as the KuPR (250 m) were overlapped with the central 25 beams of KuPR, resulting in a common swath of 125 km, as shown in Figure 3.1a. These 25 Ka-band beams are called “matched scan (KaMS)”, and the other 24 beams which have a different range resolution (500 m) and are called “high sensitivity scan (KaHS)” because of their superior noise performance, were interleaved with the KaMS beams as shown in Figure 3.1a. On 21 May 2018, the Ka-band radar was reconfigured, as shown in Figure 3.2b, to provide coincident measurements with KuPR over a 245 km common swath [81]. This new configuration allows a comparison of radar backscatter characteristics at both frequencies for a common EIA range (nadir to  $\pm 18^\circ$ ).

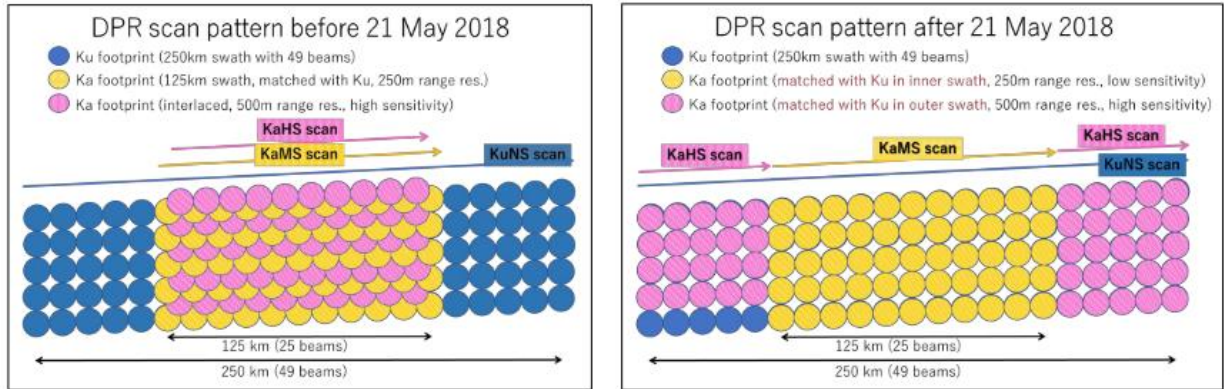


Figure 3.1: Scan pattern of GPM DPR: (a) before May 21, 2018, and (b) after May 21, 2018. Blue circles indicate KuPR footprints, while yellow and pink circles represent matched (KaMS), and high sensitive (KaHS) swath of Ka [81].

### 3.2.2: Collocation and Quality Control

Two years (2019-2020) of Ku and Ka PR level 2 standard (L2A GPM V07) products from the NASA GPM research data archive (<https://arthurhou.pps.eosdis.nasa.gov>) were used to develop the GMFs, and another independent year (2021) was prepared for the validation. In addition to atmospheric attenuation corrected ocean surface  $\sigma^0$ , the DPR product also contains navigation, sensor geometry, geolocation, and quality flags. PR rain, surface type, and data quality flags were used to filter the radar backscatter to ensure rain-free ocean  $\sigma^0$  measurements, which were then smoothed (using a triangular moving average filter) to remove quantization noise caused by analog to digital conversion. Finally, the filtered ocean  $\sigma^0$  measurements were collocated with pertinent environmental parameters from two sources to provide a “match-up” dataset.

The first source of environmental parameters (WS and SST) were geophysical retrievals from coincident passive microwave GMI brightness temperatures ( $T_B$ s). These data were provided by the Remote Sensing Systems (RSS) archive (<http://www.remss.com/missions/gmi/>) [105] in the form of daily  $0.25^\circ$  earth-gridded maps that were separated into ascending and descending orbit

segments. For the 10-m wind speed, we used the wind speed that was derived from low-frequency channels (10.7, 18.7, 23.8, and 36.5 GHz). The second source of environmental parameters was the European Centre for Medium-Range Weather Forecasts (ECMWF) global atmospheric reanalysis (ERA-5) [106]. Hourly 10-meter neutral wind vector and SST products with 31 km grid spacing are available in ERA-5, which were re-gridded in  $0.25^\circ$  to match GMI products.

Finally, the match-up dataset was completed by gridding the GPM DPR data (Ku and Ka) into  $0.5^\circ \times 0.5^\circ$  (and  $0.25^\circ \times 0.25^\circ$ , for performance comparison) boxes, with associated GMI-derived WS and SST and ERA-5 WD. All  $\sigma^0$  measurements in a box were averaged (in linear units), boxes with a high standard deviation were discarded, and RSS data quality flags were also used to exclude any rain, sea-ice, and land-contaminated data from the match-up dataset. Since DPR and GMI obtain near-simultaneous observations over a common ocean surface sub-swath, the two-year time series resulted in millions of co-located, clear-sky global ocean measurements over a wide variety of environmental conditions. This provides a unique Ku/Ka  $\sigma^0$  match-up dataset that is reported for the first time in this chapter. In addition, results were produced using two environmental suits, one using GMI WS and SST with ERA-5 WD and the other using all ERA-5 products (WS, WD, and SST). The differences were insignificant, except for some mean biases (DC-offsets) between the two results. Therefore, the results of the later combination were used in the final GMF to make it consistent throughout.

### 3.3: Geophysical Model Function for the Ocean Ku and Ka-Band PR Backscatter

The microwave ocean surface radar backscatter ( $\sigma^0$ ) at the GPM DPR incidence angle range ( $0^\circ$  to  $18^\circ$ ) is dominated by a quasi-specular scattering process, but towards the outer swath, the resonant (Bragg) scattering process becomes significant [49]. For both regimes, the  $\sigma^0$  is



directly related to the ocean surface wind vector (OVW), SST, and integral wave parameters [98]–[100], [102], [107]–[109]. The backscatter can be empirically modeled as a second-order Fourier series (higher-order terms are negligible),

$$\sigma_{dB}^{\circ}(f, p) = A_0 + A_1 \cos(\chi) + A_2 \cos(2\chi) + B_1 \sin(\chi) + B_2 \sin(2\chi) \quad (3.1)$$

where  $\sigma_{dB}^{\circ}(f, p)$  is the sea surface normalized radar cross section at a frequency ( $f$ ) and polarization ( $p$ ) in dB unit. The model coefficients  $A_0, A_1, A_2, B_1,$  and  $B_2$  are wind speed, EIA and sea-state dependent, and  $\chi$  denotes the wind direction relative to the radar azimuth look defined as,

$$\chi = \varphi_{wind} - \varphi_{radar} \quad (3.2)$$

where  $\varphi_{wind}$  is the meteorological wind direction (the direction where the wind is coming from), and  $\varphi_{radar}$  is radar azimuth look. Since the primary purpose of DPR is not OVW measurement, the azimuth look is not provided with the DPR standard data suite. For DPR, the cross-track azimuth look can be calculated as,

$$\varphi_{DPR} = \varphi_{flight} \pm 90^{\circ} \quad (3.3)$$

where  $\varphi_{flight}$  is the spacecraft's flight direction, and  $\varphi_{DPR}$  is the DPR azimuth look, both referring to the North. We calculated the spacecraft flight direction using the longitude and latitudes of the spacecraft subsatellite points according to [110]. This is illustrated in Fig. 3.2. Blue solid circles in the figure represent DPR footprints. The cross-track scanning direction reverse for yaw 0 and 180 orientations.

Accordingly, following Eq. 3.2,  $\chi = 0$  thus denotes the upwind specifying that the wind is blowing toward the radar look direction. Similarly,  $\chi = 180$  specifies the downwind, and  $\chi = 90$  and  $270$  indicate the crosswind directions. These particular directions have distinct backscatter characteristics, thus will be referenced repeatedly in the following sections. Since both Ku and Ka

PR onboard GPM operate at only horizontal polarization, all references to polarization are omitted hereafter.

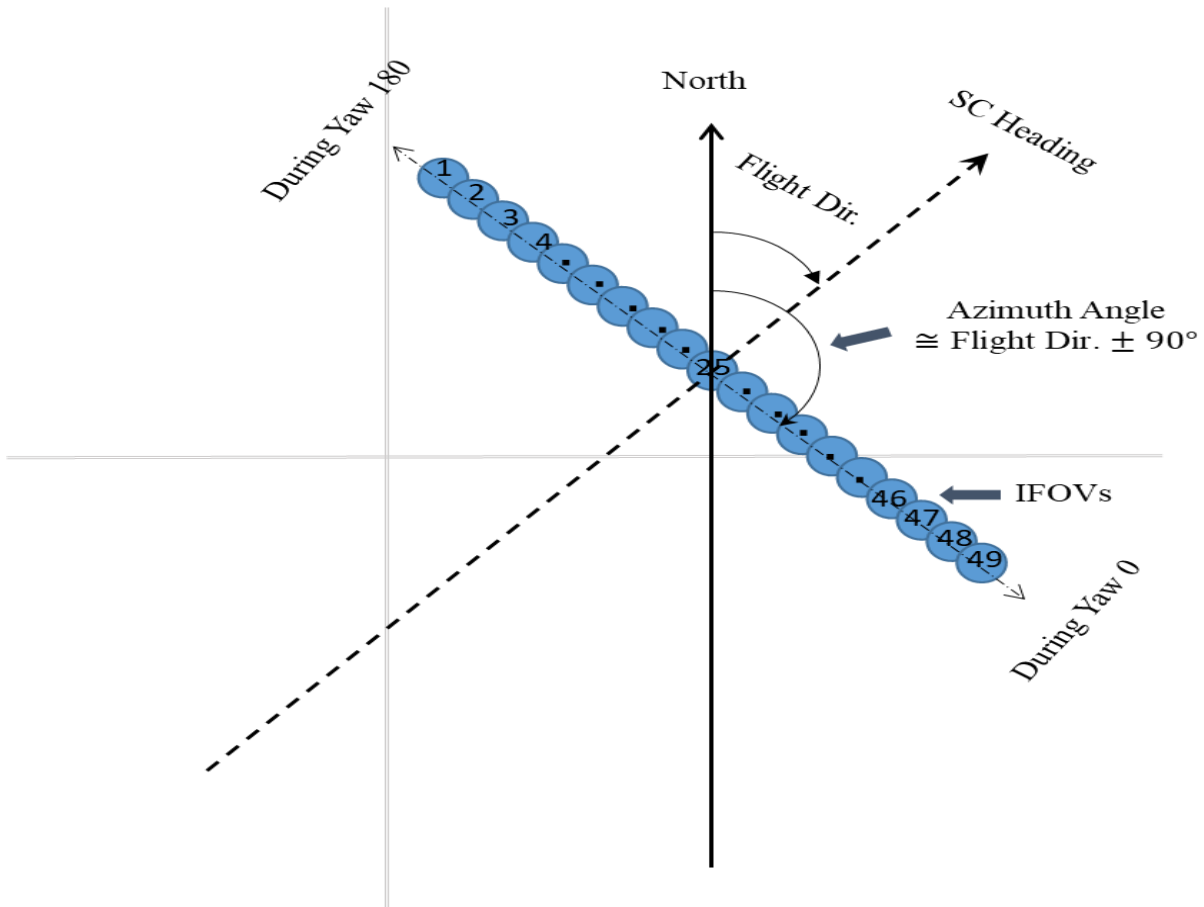


Figure 3.2: Spacecraft heading and DPR azimuth viewing angle.

Historically, the radar ocean backscatter GMF has been modeled as a truncated even Fourier series [25,26], but our initial analysis used both sine and cosine terms in Eq. 3.1 to examine if the symmetry property changes for lower EIA. However, after a comprehensive investigation, it was found that the sine terms were not statistically significant, and as a result, they were neglected. The  $\sigma^0$  azimuth anisotropy can be well approximated by even terms.

$$\sigma_{dB}^0(f, p) = A_0 + A_1 \cos(\chi) + A_2 \cos(2\chi) \quad (3.4)$$

It should be noted that Eq. 3.4 is the same expression used to model the ocean backscatter at moderate EIAs ( $20^\circ$ – $70^\circ$ ). However, a significant difference is that the  $A_1$  term is negative for  $EIA < 20^\circ$ , which results in a reversal of upwind and downwind asymmetry, i.e., higher downwind backscatter than the upwind backscatter.

We described the derivation of Fourier coefficients  $A_0$ ,  $A_1$  and  $A_2$ , and analyzed their properties for each angular beam (EIA) position in [92]. Here, to make the retrieval faster, we chose to make the GMF in tabular forms instead of using analytical functions. In this section, we describe the derivation of tabular GMFs for Ku- and Ka-band and analyze their dependence and sensitivity on incidence angle (EIA), wind speed (WS), azimuth or relative wind direction (WD), and sea surface temperature (SST).

### 3.3.1: Binning

The binning procedure to derive  $\sigma^0$  GMF is illustrated in Fig. 3.3 below. For each beam position, the total set of yearly matchup datasets is divided into 7 SST ranges with a sliding window of  $\pm 5^\circ C$ . Then for each of the SST ranges, the data were sorted in  $\pm 0.5 \text{ ms}^{-1}$  wind speed bins. Finally, the data were sorted into  $\pm 5^\circ$  relative wind direction bins for each WS bin, and corresponding bin averages and standard deviations were recorded. A conservative  $3\sigma$  filter was applied to each bin to remove outliers (the mean, STD, and  $3\sigma$  values were calculated in linear, not dB, units), and any bin with less than 300 boxes was not included in the analysis. The  $\sigma^0$  bin averages and STDs were computed on a yearly basis, and the final bin average and STD were calculated by averaging over two years (2019 and 2020). To have the working GMFs for retrieval, the bin averages were further resampled into  $0.1 \text{ ms}^{-1}$  WS and  $1^\circ$  RWD steps (no resampling was

applied for SST and EIA beam positions). The same approach for preprocessing, binning, and resampling was used to derive Ku- and Ka-band GMFs.

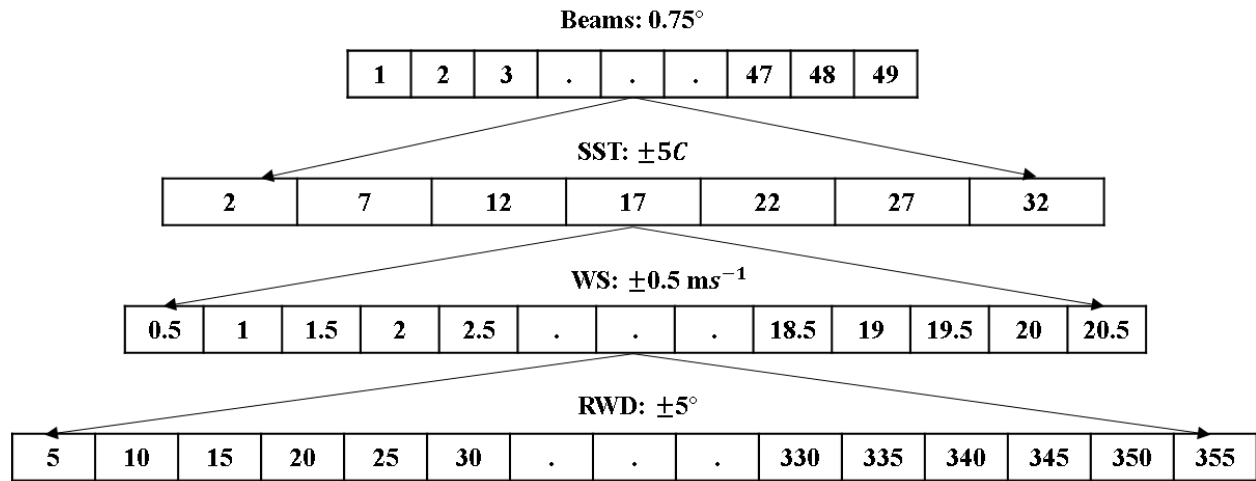


Figure 3.3: Binning procedure for  $\sigma^0$  geophysical model function

### 3.3.2: Wind Speed and Incidence Angle Dependence of $\sigma^0$

The mean  $\sigma^0$  at a particular azimuth is mainly a function of wind speed (WS) and earth incidence angle (EIA) and, to some extent, of sea surface temperature (SST). The WS dependence of mean  $\sigma^0$  is illustrated in Figure 3.4 using a log-log plot for six PR beams and three relative azimuth positions at an averaged SST. At the higher EIA beam positions,  $\sigma^0$  monotonically increases with wind speed, whereas it monotonically decreases for lower EIAs near the nadir. For the middle EIA beam positions, the  $\sigma^0$  dependence is not monotonic because two different scattering mechanisms are involved. Namely, the near nadir backscatter is dominated by quasi-specular scattering that decreases  $\sigma^0$  with increased ocean roughness, but as EIA increases, Bragg scattering gradually becomes significant that increases  $\sigma^0$  with WS. The Ku-band results are

consistent with [32], [49], [95], [97]–[100], [102], except for a slight calibration bias between TRMM PR and GPM KuPR.

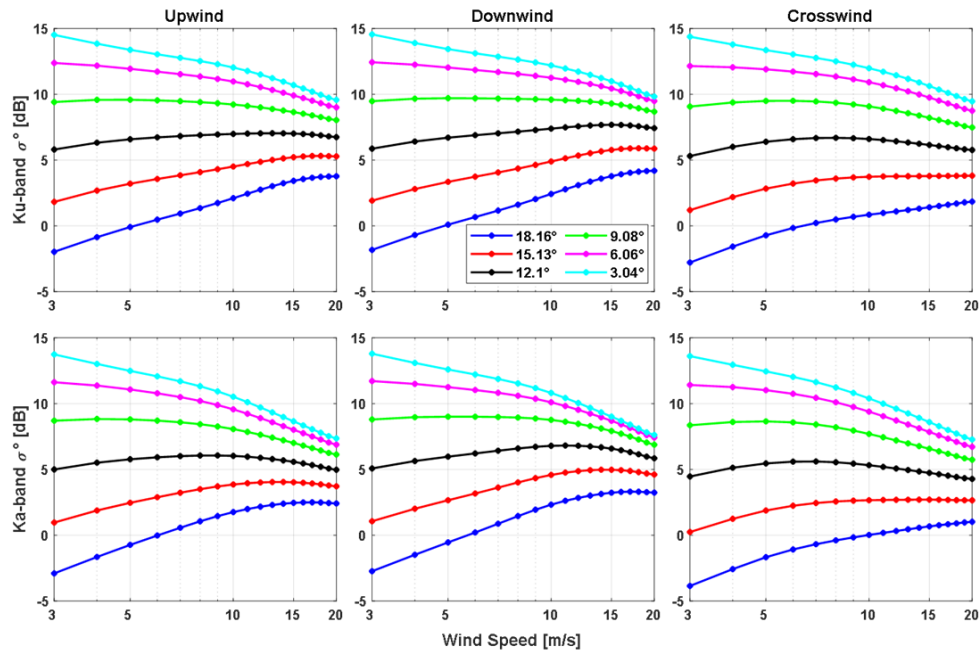


Figure 3.4: Mean value of binned KuPR (top panel) and KaPR (bottom panel)  $\sigma^0$  as a function of wind speed for different earth incidence angle  $\theta$  for upwind (left), downwind (middle), and crosswind (right) relative wind directions.

The mean values of binned average  $\sigma^0$  for Ku and Ka bands are shown in Figure 3.5 as a function of EIA for different wind speeds. The  $\sigma^0$  monotonically decreases with increasing incidence angle from nadir to  $18.2^\circ$ . Additionally, the  $\sigma^0$  decreases monotonically with wind speed at EIAs near the nadir, but  $\sigma^0$  increases monotonically with wind speed near EIA  $18.2^\circ$ , with a transition in the middle where  $\sigma^0$  becomes relatively insensitive to WS. For KuPR, this transition occurs over EIA  $9^\circ$ – $10^\circ$ , whereas, for KaPR, it occurs over EIA  $10^\circ$ – $11^\circ$ . Additionally, these transition regions vary with the relative azimuth look for upwind/downwind/crosswind directions, as shown for KuPR in Figure 3.5. This EIA range of reduced  $\sigma^0$  variability is useful for the radar inter-calibration between these kinds of instruments.

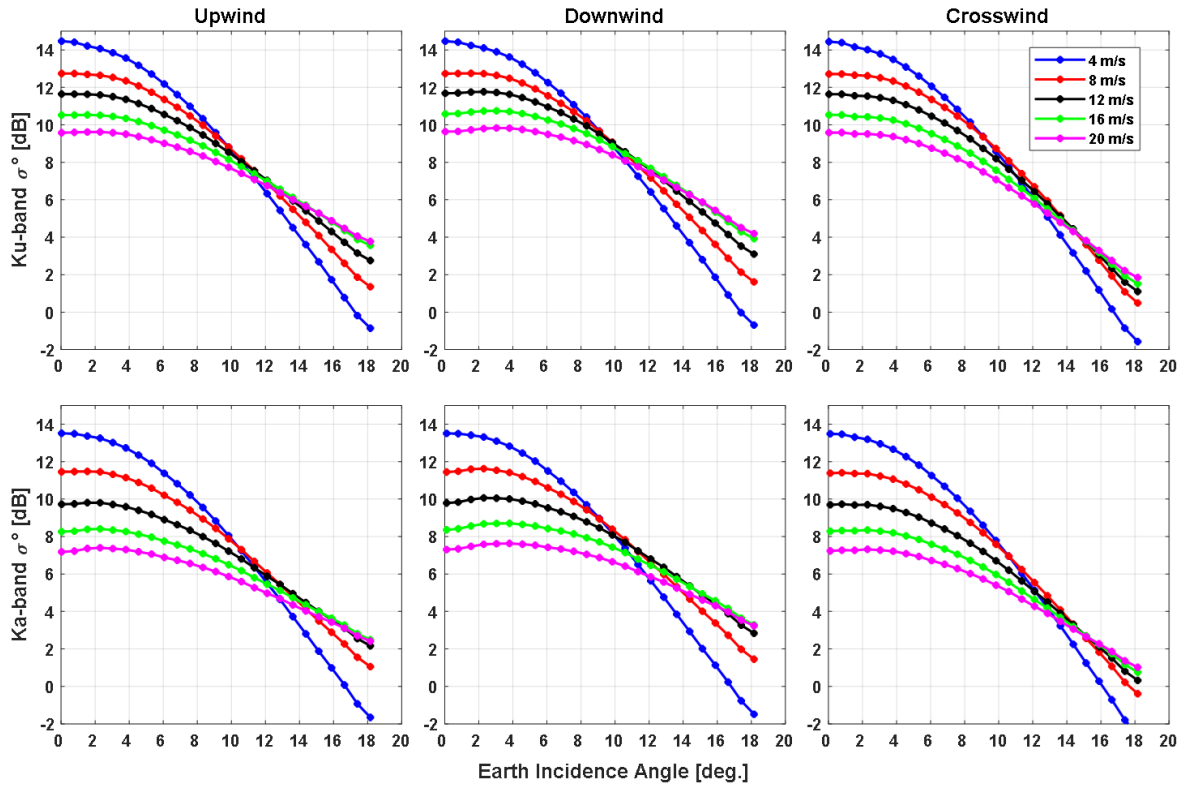


Figure 3.5: Mean value of binned KaPR (top) and KuPR (middle)  $\sigma^0$  as a function of earth incidence angle  $\theta$ , for different wind speeds

While these results (presented in Fig. 3.4 and 3.5) are qualitatively similar for Ka PR, there are small differences between Ku and Ka bands, and these differences are also a function of wind speed and incidence angle and can be 0.25 to 2.25 dB depending on the EIA and WS (not shown). Besides this, the WS sensitivity or  $\sigma^0$  gradient, defined as  $(\partial\sigma^0/\partial WS)$ , declines with WS at both bands. An important implication is the variation of the dynamic range of wind-roughened  $\sigma^0$  with EIA. This is shown in Figure 3.6, which compares the maximum wind-dependent variation (variation of  $\sigma^0$  for WS change of 1 m/s to 20 m/s) of the Ku band mean  $\sigma^0$  with that at Ka-band.

Although both have similar dynamic ranges for EIA  $\sim 9^\circ$ , Ka-band mean  $\sigma^0$  has a higher overall dynamic range for EIA  $< 9^\circ$ .

Therefore, based on these results, we conclude that the two GMFs are similar and are applicable for a WS range of 3–20  $\text{ms}^{-1}$  and all EIA beam positions.

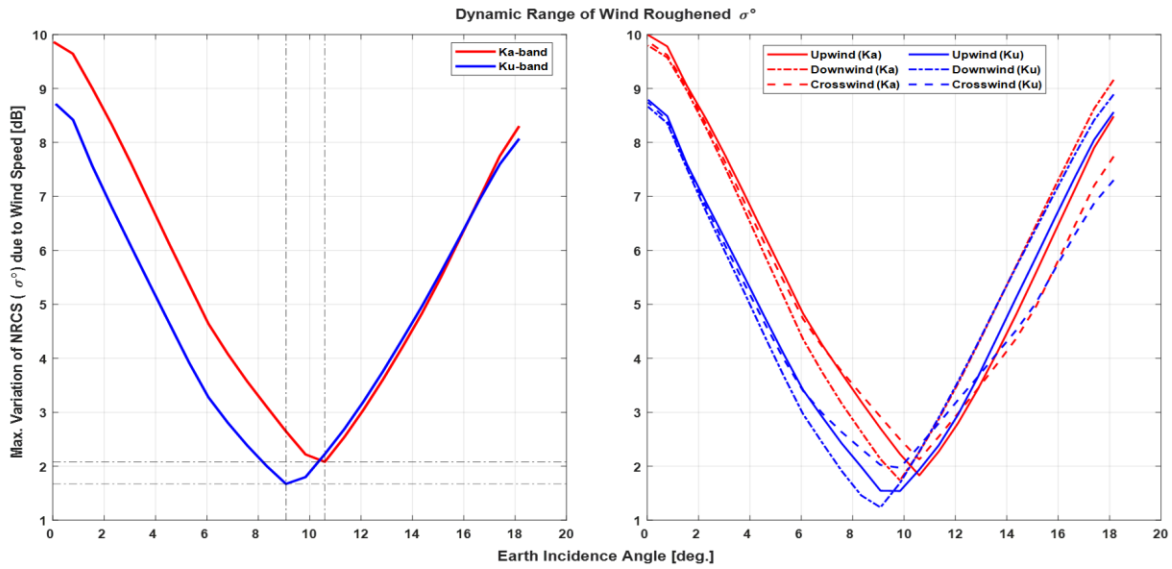


Figure 3.6: Wind speed sensitivity of Ka-band vs. Ku-band  $\sigma^0$  with EIA: the left-side Fig. compares the maximum variation of  $\sigma^0$  for WS change 1 m/s to 20 m/s at Ku-band (blue) with Ka-band (red) at averaged relative wind direction; the right-side Fig. plots the same, but for upwind (solid line), downwind (dashed-dot line), and crosswind (dashed line) directions.

### 3.3.3: Azimuthal Anisotropy of $\sigma^0$

When mean,  $\langle \sigma^0 \rangle$ , over all relative wind direction, are subtracted from each bin, the  $\sigma^0$  directional anisotropy is found, which is a function of WS, relative wind direction for a given EIA (beam position). Mathematically, it can be expressed as follows,

$$\sigma^0 - \langle \sigma^0 \rangle = \sigma^0_{(residual)} = A_1 \cos(\chi) + A_2 \cos(2\chi) \quad (3.5)$$

where the  $A_1$  and  $A_2$  coefficients measure upwind-downwind, and upwind-crosswind asymmetry, respectively.

Figure 3.7 shows the  $\sigma^0$  residual (anomaly) of the KuPR (top panel) and KaPR (bottom panel) as a function of relative wind direction for three different EIAs ( $18^\circ$ ,  $16^\circ$ , and  $14^\circ$ ) and WS (6, 10, and 14 m/s). The symbols are the residual of the measured bin average, and the solid lines are the corresponding Fourier fit (Eq. 3.5, shown just for comparison). The bi-harmonic directional signal increases with both WS and EIA, and the Ka-band anomaly is higher than Ku-band for the same EIA and WS. Generally, the Fourier model is in excellent agreement with the empirical measurements for both the band, except for the lower EIAs ( $EIA < 6.8^\circ$ ), where the quality of the model fit is somewhat lacking (not shown).

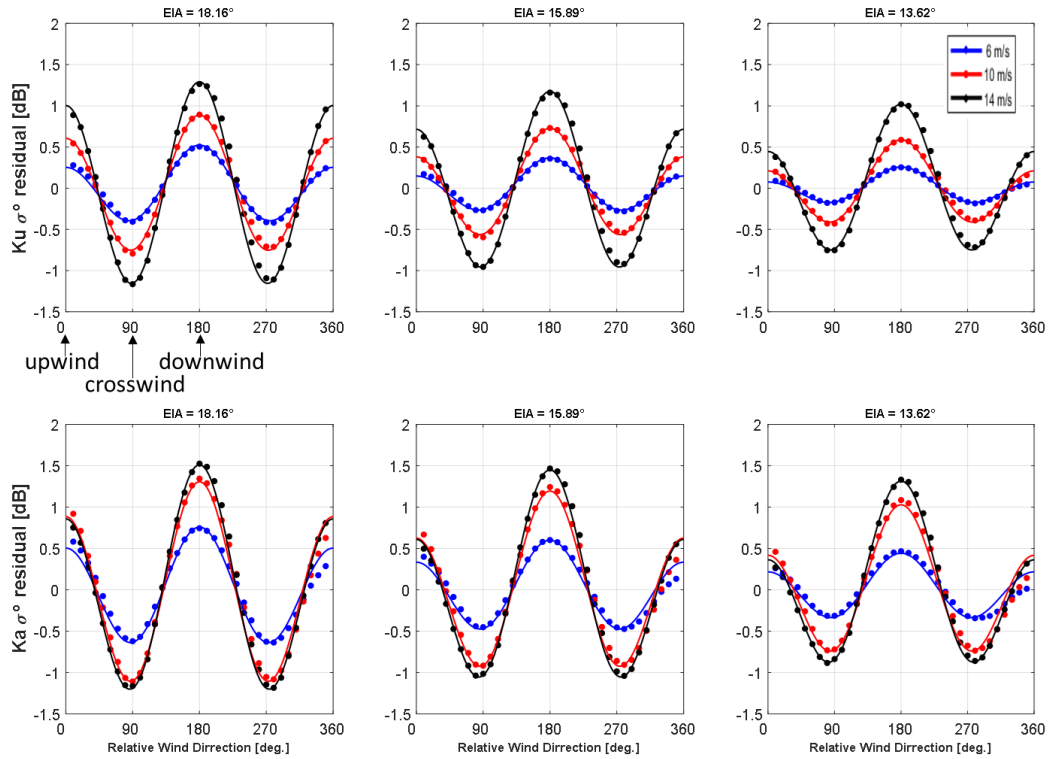


Figure 3.7: KuPR (top panel) and KaPR  $\sigma^0$  (bottom panel) directional anisotropy (in dB) as a function of relative wind direction ( $\chi$ ) for three different WS values: 6 m/s (blue), 10 m/s (red), and 14 m/s (black) at different earth incidence angles (indicated at the top of each figure). The symbols are bin average, while the solid lines represent their second-order Fourier fits.



### 3.3.3.1: *Upwind and Downwind Asymmetry of $\sigma^0$*

One of the distinct features of the  $\sigma^0$  WD anisotropy at low EIA is that it has an opposite upwind/downwind asymmetry compared to the conventional scatterometers that operate at moderate incidence angles ( $30^\circ$ – $70^\circ$ ). As shown in Fig. 3.8, DPR measures a higher  $\sigma^0$  from the downwind direction than that from the upwind direction, and  $2A_1$  is the measure of the peak-to-peak upwind/downwind asymmetry. The differences between downwind and upwind  $\sigma^0$  measurements, separately for both KuPR and KaPR as a function of WS: 3–20 m/s, are shown in Fig. 3.8 for six different EIAs:  $3^\circ$ – $18^\circ$ , and it is noted that for all EIAs, the measured  $\sigma^0$  asymmetry increases with WS of 6–16 m/s. Chu et al. [111] also presented similar results for TRMM KuPR, and Mouche et al. [112] reported the same trends of asymmetries for a C band radar at low incidence angles. Yurovsky et al. [113] showed that, at Ka-band, the upwind-downwind asymmetry disappears at an incidence angle of  $32^\circ$ , becomes positive above it, and the  $\sigma^0$  becomes unimodal with relative wind direction for a high incidence angle ( $> 70^\circ$ ) when the downwind  $\sigma^0$  becomes even lower than the crosswind  $\sigma^0$ . Here, for incidence angle  $\leq 18^\circ$ , we confirm that both Ku- and Ka-band has negative upwind-downwind asymmetry and additionally report the new information that Ka-band has a significantly higher downwind-upwind asymmetry than the Ku band. For example, at EIA  $\sim 12^\circ$ , the Ku band asymmetry is about 0.7 dB for a WS of 15 m/s, while it is  $\sim 1$  dB for Ka-band for the same EIA and WS.

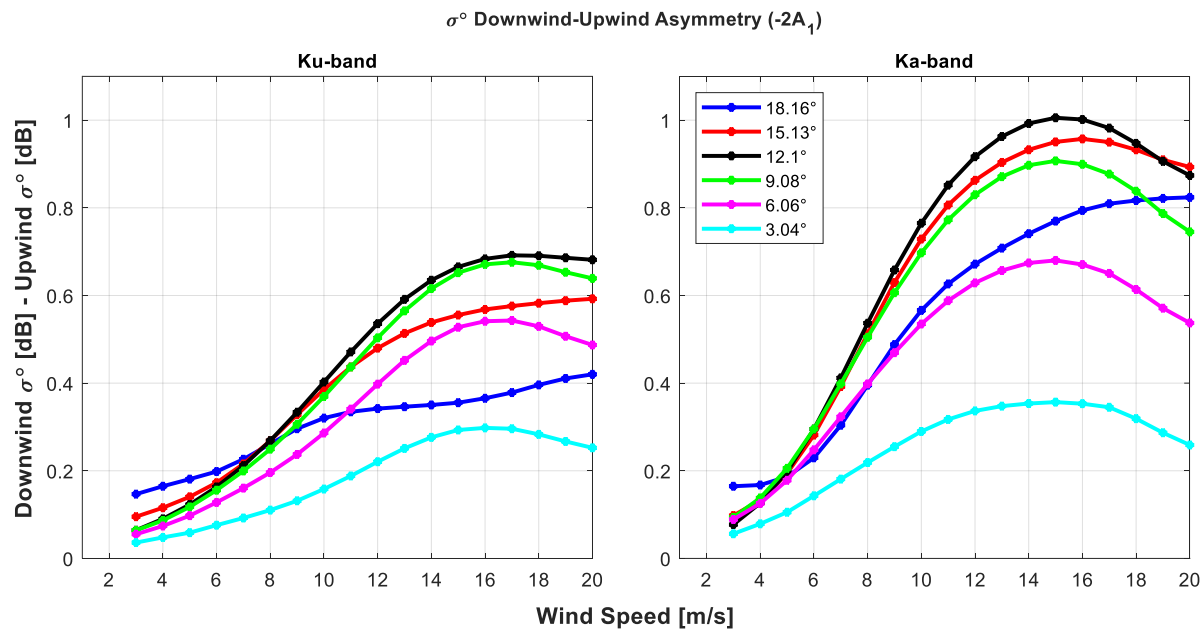


Figure 3.8: Peak-to-peak KuPR (left) and KaPR (right)  $\sigma^0$  downwind/upwind asymmetry (in dB) as a function of WS at different EIAs.

### 3.3.3.2: Downwind and Crosswind Anisotropy of $\sigma^0$

For scatterometers operating at moderate EIAs, the  $A_2$  the coefficient in Eq. 3.2 and 3.5, usually defines the peak-to-peak (upwind to crosswind) anisotropy of  $\sigma^0$ . However, for this low EIA range, since  $A_1$  is negative and not negligible, backscatter response at the downwind direction is the sum of  $A_1$  and  $A_2$ . Therefore, the peak-to-peak anisotropy for this EIA range is defined downwind to crosswind, which is  $> 2A_2$ . Figure 3.9 shows the peak-to-peak  $\sigma^0$  anisotropy for Ku and Ka bands as a function of WS for different EIAs.

As shown, the downwind to crosswind asymmetry of  $\sigma^0$ , which defines the overall directional sensitivity of radar backscatter, increases with wind speed for  $WS > 6$  m/s at all incidence angles and monotonically increases with incidence angles. Again, the Ka-band downwind to crosswind anisotropy was also found to be larger than the corresponding Ku-band directional anisotropy for

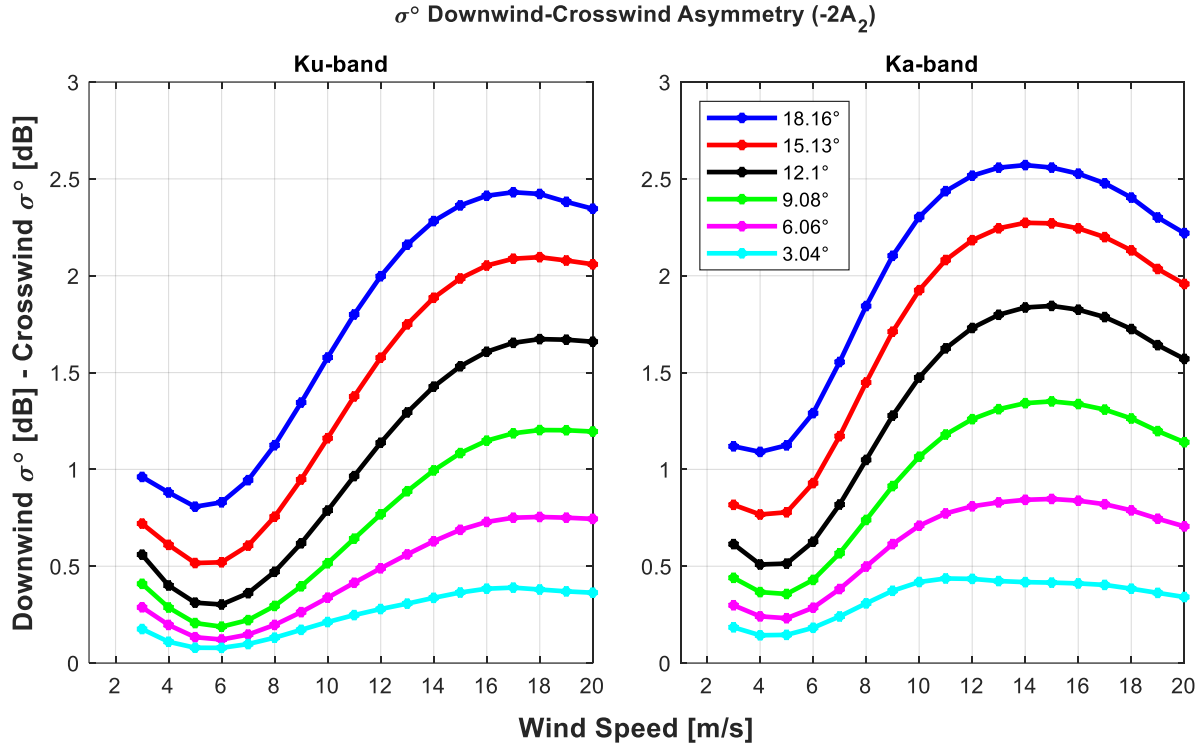


Figure 3.9: Peak-to-peak KuPR(left) and KaPR (right) downwind/crosswind  $\sigma^0$  anisotropy (in dB) as a function of WS at different EIAs.

low to moderate WS range. Conversely, the saturation of directional anisotropy at the Ka-band occurs at relatively lower WS. This is perhaps due to the larger impacts of wave breaking and sea foams on the Ka-band  $\sigma^0$  for relatively lower wind speeds, as reported in recent literature [20], [21-22].

Figure 3.10 presents the DPR wind speed, directional sensitivity, and corresponding uncertainty as a function of the beam positions over the 245 km swath covering an EIA range of  $-18^\circ$  to  $+18^\circ$  through the nadir. As shown, although nadir and near beam positions have significantly higher wind speed sensitivity than the outer swath (as shown in Fig. 3.10a), the directional sensitivity decreases (shown in Fig. 3.10b), and the measurement uncertainty increases (see Fig.

3.10c) as incidence angle decreases towards the nadir. Therefore, wind direction retrieval performance degrades near and over nadir beam positions. In addition, the transition region near EIA  $\sim 10$  (beam positions  $\sim 7-12$ ) also provides poor WS retrieval. Besides the azimuth diversity, these constraints also make the complementary passive counterparts essential for OVW retrieval.

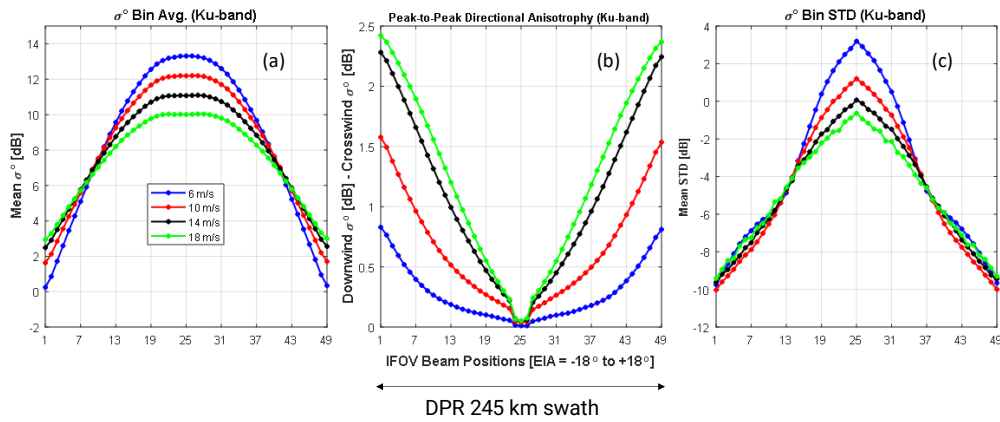


Figure 3.10: PR sweet swath for OVW retrieval

### 3.3.4: Sea Surface Temperature Dependence of $\sigma^0$

At low microwave frequencies (1–8 GHz), sea surface temperature affects the dielectric constant of sea water and the resulting Fresnel reflection coefficient; however, this effect is weak at Ku and Ka bands [114]. On the other hand, SST also affects the surface tension and viscosity of the sea water, both of which control the amplitude of the capillary wave spectral region of the sea surface roughness. Surface tension dominates the capillary wave spectrum for the low wind speed regime ( $\sim WS < 6$  m/s). In contrast, wave breaking occurs for higher WS, and viscosity plays a significant role in controlling the roughness. Thus, surface tension and viscosity, which tend to reduce surface roughness, decrease with increasing SST. As a result, ocean  $\sigma^0$  increases with SST.

V-polarized signals exhibit more significant dependencies on SST than H-pol signals [115]. Since GPM DPR measurements are both H pol, this paper presents only SST impacts on H pol at low incidence angles; however, for these low EIA's, the polarization effect is not expected to be significant.

In previous research [115], it was concluded that the SST has a small but significant effect on the observed ocean  $\sigma^0$  at the Ku band; therefore, the SST effects were explicitly included in the development of the four-dimensional (4D) Ku- and Ka-band  $\text{GMF} = f(\text{WS}, \text{WD}, \text{EIA}, \text{SST})$ . A qualitative assessment of the impact of SST on the GMFs is presented below.

The dependence of  $\sigma^0$  on SST was empirically characterized for both Ku- and Ka-bands as a function of EIA and WS using the following statistical procedure. First, the  $\sigma^0$  values, in linear power ratio units, were bin averaged (over all WS and WD) in 1 C steps of SST 0–30 C. Next, the binned averages were normalized to the corresponding  $\sigma^0$  values at 15 C, and the results are presented in Fig. 3.11. Figure 3.11 shows an approximately linear dependence of the relative  $\sigma^0$  on SST for all EIA beam positions under consideration at both frequencies. However, the Ka band's SST dependency is significantly stronger ( $> 2 \times$  slopes). For example, for an EIA =  $9^\circ$ , the overall variation of mean  $\sigma^0$  with SST over the range 0–30 C is  $< \pm 5\%$  at Ku, whereas it is  $> \pm 10\%$  for Ka. This is expected because the Ka-band backscatter is more sensitive to the density of the small-scale spectrum of the capillary waves and the impact of the wave breaking.

Next, these SST impacts are presented for WS values of 4, 8, and 12 m/s in Figure 3.12 for an EIA of  $9.8^\circ$ . Here, the results are like Figure 3.11 (averaged over all WS); however, there is also a slight WS dependence, as noted by the separation of the curves. This is especially notable at the higher and lower EIA.

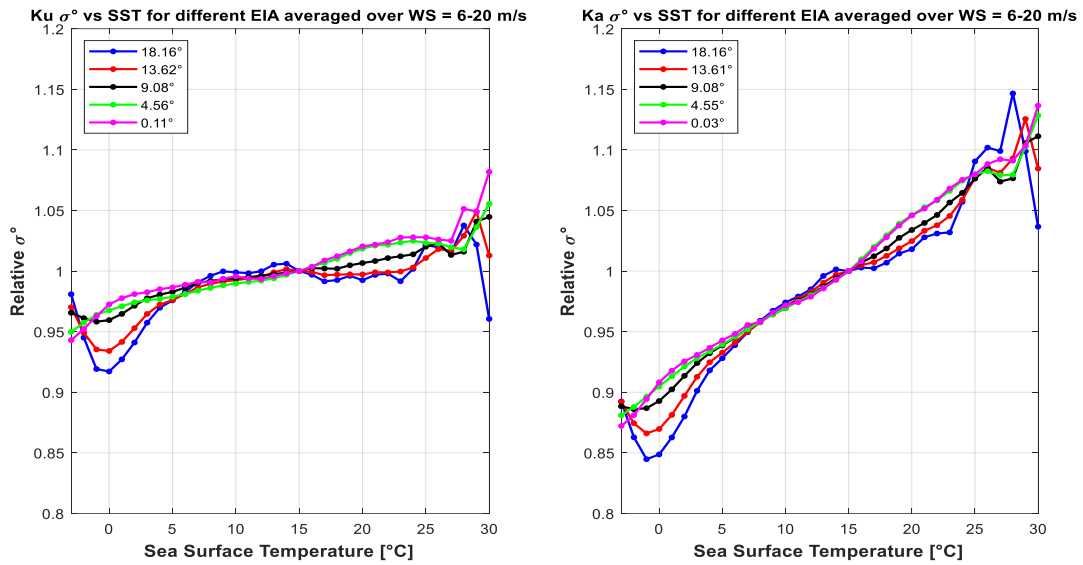


Figure 3.11: SST dependence of KuPR and KaPR  $\sigma^0$  at different EIA. Relative  $\sigma^0$  here indicates  $\sigma^0 / \sigma^0(@15C)$  ratio.

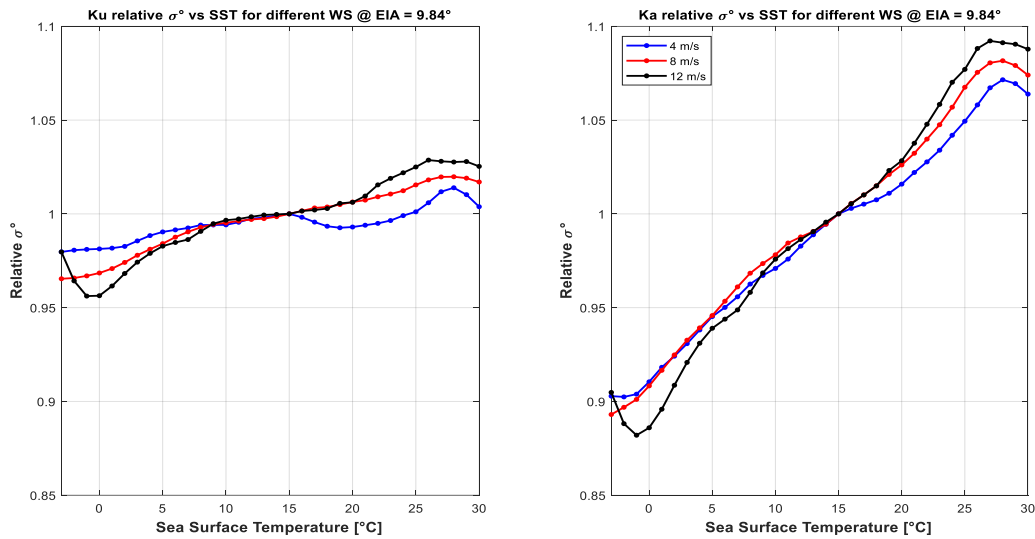


Figure 3.12: SST dependence of KuPR and KaPR  $\sigma^0$  at different EIA. Relative  $\sigma^0$  here indicates  $\sigma^0 / \sigma^0(@15C)$  ratio.

### 3.4: Discussion

The dual-frequency precipitation radar (DPR) onboard the GPM core satellite provides coincident Ku and Ka-band  $\sigma^0$  measurements over a wide near-nadir EIA range. This study leveraged the unique opportunity to investigate near-nadir ocean surface backscatter characteristics using measurements from two Ku and Ka-band radars on the same satellite that provided an excellent dataset to derive the corresponding backscatter GMFs. This is unprecedented, and the results are significant because the data used was reliably large, and all the measurements were precisely collocated in space and time. More importantly, the same surface truth data (WS, WD, and SST) and the same data analysis procedure were applied to characterize the wind vector and SST dependency of Ku- and Ka-band radar backscatter for a full EIA range of  $\pm 18^\circ$ . Although the Ku-band results are consistent with the previous studies, the comparison with Ka-band is somewhat unique. Both GMFs were thoroughly explored, and results were presented in parallel so one can easily compare critical characteristics at both bands for utilization in scatterometry and other ocean science applications from space.

The trends of WS-only dependency of Ku- and Ka-band radar backscatter at the EIA ranges under consideration were shown to be similar in the way that ocean surface radar backscatter increases (for higher EIA) and decreases (for lower EIA) monotonically with WS, but the slope of increase flattens as the WS increases. The difference of mean  $\sigma^0$  between the Ku- and Ka-band depends on both WS and EIA, and within around 2 dB for WS 1–20 m/s and EIA 3–18°. The difference is reduced with increasing EIA, and with WS, it is lower at moderate WS but increases at both higher and lower WS. However, the Ka-band ocean radar backscatter's directional sensitivity was higher than Ku-band directional sensitivity for low to moderate WS regimes. This

is particularly significant in path attenuation correction, radar calibration, and in considering future missions for ocean wind vector remote sensing at Ka-band. However, it was also shown that the saturation of directional anisotropy at the Ka-band occurs at relatively lower WS, which might limit the use of the Ka-band for remote sensing of higher WS.

Moreover, the SST effects were shown to be substantially higher at Ka-band than that at Ku-band. In recent years, the SST impact on Ku-band GMFs and subsequent wind retrieval have raised a concern. As a result, different ways of correcting existing GMFs and developing fully SST-dependent GMFs have been undertaken. The SST dependency presented here for Ku-band GMFs is consistent with the developing literature, and the results presented for Ka-band are also consistent with theories.

The Fourier cosine series model used to develop conventional scatterometer GMFs was also shown to apply to radar backscatter models at low EIA. However, the distinct upwind and downwind asymmetry was also made clear for both bands. Therefore, this chapter provides the basis of the active part of the combined active and passive ocean wind vector retrieval, as will be discussed in Chapters 4 and 5.



## CHAPTER 4: PASSIVE GEOPHYSICAL MODEL FUNCTION

### 4.1: Introduction

In this chapter, we describe the procedure for developing a passive geophysical model function (GMF) which is a physics-based empirical relation between a linear combination of brightness temperatures ( $T_B$ s) and ocean surface wind speed (WS), relative wind direction ( $\chi$ ), and sea surface temperature (SST).

### 4.2: Radiative Transfer

The radiative transfer theory (RTM) provides an estimate of the total top of the atmosphere apparent brightness temperature ( $T_B$ ) as a function of geophysical parameters at the input of the radiometer receiver. From RTM, the  $T_B$ , measured with signal frequency ( $f$ ), polarization ( $p$ ), earth incidence angle ( $\theta$ ), and azimuth look angle ( $\Phi$ ), can be expressed as [116], [117],

$$T_B(p, f, \theta, \Phi, \dots) = \tau E T_S + T_{BU} + \tau R T_{BD} + \tau^2 R T_{BC} + \Omega_{OVW}(\tau R T_{BD} + \tau^2 R T_{BC}) \quad (4.1)$$

where  $T_{BU}$  and  $T_{BD}$  are upwelling and downwelling atmospheric brightness temperatures, respectively, and given by,

$$T_{BU} = \int_0^\infty \tau(z, S) \alpha(z) T(z) dz \quad (4.2a)$$

$$T_{BD} = \int_0^\infty \tau(0, z) \alpha(z) T(z) dz \quad (4.2b)$$

where  $T(z)$  and  $\alpha(z)$  are the atmospheric temperature and absorption profile along the viewing path  $z$ .  $\tau(z_1, z_2)$  is the atmospheric transmittance between the two locations  $z_1, z_2$ , and related to the atmospheric absorption coefficient  $\alpha(z)$  by,

$$\tau(z_1, z_2) = e^{-\left(\int_{z_1}^{z_2} \alpha(z) dz\right)} \quad (4.3)$$

The transmissivity  $\tau$  in Eq. 4.3 is given as the total atmospheric transmittance between the ocean surface and the satellite altitude  $S$  [*i. e.*,  $\tau \equiv \tau(0, S)$ ].  $T_S$  in Eq. 4.1 represents sea surface temperature (SST) in Kelvin. The  $E$  and  $R$  indicate the ocean surface emissivity and reflectivity, respectively, and are related to each other by Kirchhoff's law,

$$E + R = 1 \quad (4.4)$$

Therefore, the first term in Eq. 4.1 represents the ocean surface emission at surface temperature  $T_S$ , that is transmitted through the Earth's total atmosphere and collected by the radiometer antenna. In the second term,  $T_{BU}$ , represents the part of the atmospheric brightness temperature that travels upward from location  $z$  to radiometer altitude  $S$ . The other part of the atmospheric emissions,  $T_{BD}$ , travels downwards through the atmosphere and gets reflected by the ocean surface.  $T_{BC}$  in the third term of Eq. 4.1 is cosmic background temperature from deep space, which passes through the whole atmosphere before getting reflected by the ocean surface. It is constant and equal to 2.7 K for the frequency channels under consideration [118]. Thus, the third and fourth terms represent the total reflection by specular (smooth) ocean surface. However, the ocean surface in reality is not fully specular -- winds roughen it, and the roughness increases reflection. Here comes the ocean vector wind (OVW) modification factor  $\Omega_{OVW}$ , which takes account of this additional diffuse reflection due to wind-roughened surface scattering [117].

Ocean surface local winds generate small-scale gravity-capillary waves over large-scale gravity waves, which cause Bragg scattering (diffraction) of the downwelling atmospheric and cosmic radiation. According to Kirchhoff's rule (Eq. 4.4), it also changes the ocean surface emissivity,  $E$ , and these effects are anisotropic with wind direction relative to the sensor azimuth

look  $\Phi_{look}$ , called relative wind direction ( $\chi$ ). The relative wind direction is defined as the ocean surface wind direction relative to the sensor (GMI in this case) azimuth look ( $\Phi_{look}$ ).

$$\chi = \Phi_{wm} - \Phi_{look} \quad (4.5)$$

where the wind direction ( $\Phi_w$ ) is inferred in the meteorologic convention. In meteorologic convention, the wind direction  $\Phi_{wm}$  is defined clockwise from north to the direction from which it is blowing. The reflection symmetry property of Maxwell's Equation yields that ocean surface emissions of both vertical and horizontal polarization signals are an even and periodic function of  $\chi$ . Thus, it can be expanded using even harmonic series of the following form (the higher order terms are negligible) [117],

$$E(p, f, \theta, \Phi, \dots) = E_0(WS, SST, Sal) + E_1(WS) \cos(\chi) + E_2(WS) \cos(2\chi) \quad (4.6)$$

Similarly, the corresponding brightness temperature,  $T_B$ , from Eq. 4.1, for a given frequency channel, and a certain earth incidence angle,  $\theta$ , can be represented as [119],

$$T_{Bp} = C_{p0}(\tau, WS, SST, Sal) + C_{p1}(\tau, WS) \cos(\chi) + C_{p2}(\tau, WS) \cos(2\chi) \quad (4.7)$$

where the DC coefficient,  $C_{p0}$ , is the isotropic brightness temperature (azimuth independent) that depends on wind speed, sea surface temperature, sea surface salinity, and atmospheric transmissivity for a given earth incidence angle at a certain frequency for rain and ice-free ocean surface. The first and second harmonic coefficients  $C_{p1}$  and  $C_{p1}$  representing the upwind-downwind and upwind-crosswind asymmetry, the brightness temperature, respectively depend on wind speed and atmospheric transmissivity.

## 4.3: Methodology

### 4.3.1: Matchup Dataset, Pre-processing, and Binning

The GMI Level 1 BASE (L1BASE) brightness temperature ( $T_B$ ) data products from GPM V07 data suite in NASA GPM Precipitation Processing System (PPS) research data archive were used to develop a passive geophysical model function (GMF). For GMI, these are the same as the 1B  $T_B$  data product and are provided in multi-swath structures. These data are calibrated and geolocated and come with scan status, observation geometry, navigation data, and other quality flags. These quality flags were applied as the first screening over measurements. Then the measurements swaths were converted into regular latitude  $\times$  longitude grids of various resolutions, in particular, of  $0.25^\circ \times 0.25^\circ$  and  $0.5^\circ \times 0.5^\circ$  spatial grids (equivalent to  $25 \text{ km} \times 25 \text{ km}$  and  $50 \text{ km} \times 50 \text{ km}$  resolutions at the equator) for performance comparisons. The measurements inside each grid box were averaged, and corresponding means ( $\mu$ ), standard deviations (STD), and the number of observations (N) inside each grid box were saved for the following processing stage. The same gridding averaging method was applied to the other associated variables, including time, incidence angle, satellite azimuth angle, etc. As mentioned in Chapter 1, only 10, 19, and 37 GHz dual-polarized channels were used, in different spectral combinations, because their robust wind vector signature.

Besides the  $T_B$  data, other collocated ancillary data, like wind speed (WS) and directions (WD), sea surface temperature (SST) were used for tuning the GMFs. In addition, other physical parameters such as cloud liquid water (CLW), water vapor (WV), rain, etc., were used for screening and quality control. For these, the European Centre for Medium-Range Weather Forecasts (ECWMF) 5th generation reanalysis (ERA-5) ancillary dataset was used, which provides

hourly estimates of the surface as mentioned above parameters on a 30 km over the Earth. In addition, it also provides the vertical profiles of atmospheric variables at 137 pressure levels from the surface up to a height of 80km. All ERA5 data were spatially interpolated into  $0.25^\circ \times 0.25^\circ$  and  $0.5^\circ \times 0.5^\circ$  grids to match the GMI grids for collocation purposes.

For rain information, GPM provides high-quality and high-resolution level 3 (L3) rain measurements, called the Integrated Multi-satellitE Retrievals for GPM (IMERG) [120]. It combines precipitation estimates from a constellation of microwave (MW) and microwave-calibrated infrared (IR) satellites and surface rain gauges to provide a global rain map every 30 minutes at  $0.1^\circ$  ( $\sim 10$  km) spatial resolution. We preferred to use IMERG rain information for rain flagging because of its superior reliability over IMERG data were also interpolated into  $0.25^\circ \times 0.25^\circ$  and  $0.5^\circ \times 0.5^\circ$  Earth grids to collocate with the corresponding GMI  $T_B$ s and ERA5 variables.

ERA5 rain and cloud liquid water (CLW) data products are also less reliable. Therefore, an alternative CLW data product was used, from the Remote Sensing System (RSS) [105]. The RSS data archive provides a daily map of oceanic parameters in regular  $0.25^\circ \times 0.25^\circ$  spatial grids (equivalent to  $25 \text{ km} \times 25 \text{ km}$ ). It uses GMI brightness temperature and radiative transfer model (RTM) to derive the data suite of oceanic parameters, including wind speed (WS), sea surface temperature (SST), water vapor (WV), rain rate (RR), and cloud liquid water (CLW). Besides CLW, we included all other variables as redundant for cross-checking purposes. All WS products used in this dissertation are neutral stability 10-m neutral equivalent winds. Therefore, WS will indicate 10-m winds if not otherwise explicitly mentioned.

All these variables were finally collocated within a temporal window of  $\pm 1$  hour. A conservative land mask was applied to remove the land and coastal area measurements. Rain, CLW, SST information were used at this stage to retain rain-, cloud-, and ice-free ocean data. In addition,  $T_B$  collocate box with high variances ( $>2$  K for V-pol and  $>3$  K for H-pol 10.65, 18.7, and 36 GHz channels) were discarded to ensure a homogenous ocean scene.

The ERA5 10-m wind direction used in this study holds oceanographic convention where the wind direction  $\Phi_{wo}$  is specified as the opposite, i.e., the direction towards which it is moving. Fig.4.1a illustrates this.

$$ERA5\ WD = \Phi_{wo} = \Phi_{wm} + 180^\circ \quad (4.8)$$

The sensor azimuth look is usually provided with a level 1 data product for wind measuring instruments. Since the primary purpose of GMI was not vector wind measurement, the look azimuth is not supplied with the L1BASE data. Although it is readily calculated from the known spacecraft sub-satellite points for each scan position (flight direction), we adopted the following simple way to compute it [121]. The satellite azimuth angle, defined as the clockwise looking down between the local pixel geodetic north and the direction of the satellite, is available in L1BASE data. Therefore, it can be related to the sensor azimuth view, as illustrated in Fig. 4.1b.

$$\Phi_{look} = \Phi_{sat} + 180 \quad (4.9)$$

where  $\Phi_{sat}$  is the satellite azimuth angle, which ranges from 0 to 360 degrees.

Using Eq. 4.5, 4.8, and 4.9, the relative wind direction can be calculated as,

$$\chi = \Phi_{wo} - \Phi_{sat} \quad (4.10)$$

Therefore, the relative wind direction for GMI was calculated as the ERA5 10-m wind direction relative to the GMI satellite azimuth look. The relative wind direction ranges from 0 to 360 degrees. Therefore, Eq. 4.10 holds the same for both yaw orientations of GMI (forward and aft).

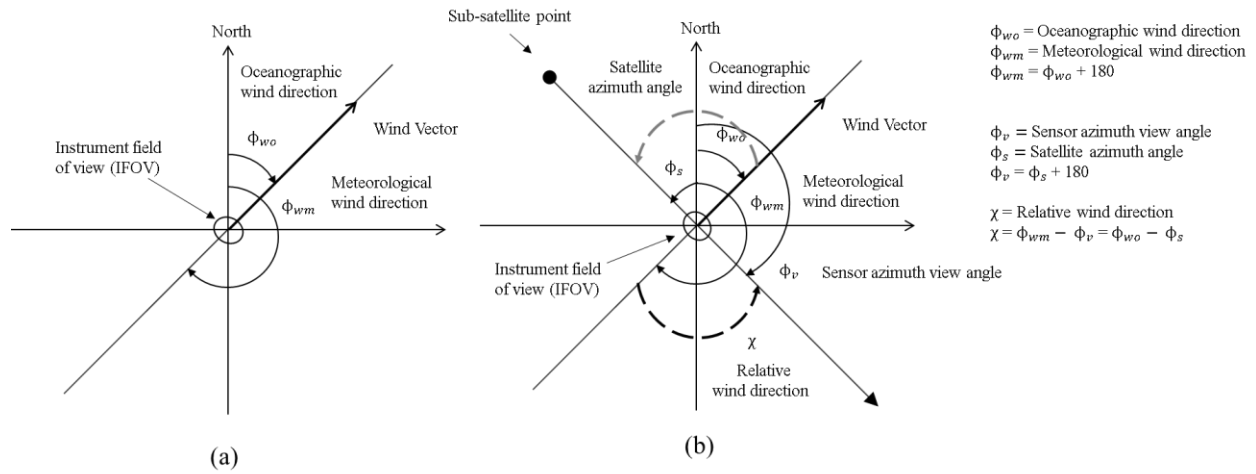


Figure 4.1: Illustration of (a) wind direction in oceanographic and meteorological convention and (b) relative wind direction. A thick black arrow indicates the wind vector, and the square box at the center of the Cartesian coordinate system represents a typical wind vector cell (WVC). Angles are depicted, and their interrelation is given in the caption on the top right.

The brightness temperature from the lower nine channels of GMI was first binned into 40 SST bins with SST ranges from -3 C to 36 C, and for each container, a sliding window of  $\pm 2$  C was used. However, due to sparse populations at significantly higher temperatures and to avoid possible ice contaminations, SST bins corresponding to  $<0$  C and  $>33$  C were not included in the analysis. Then within each SST bin, the  $T_B$ s were subdivided into wind-speed compartments from 0.5 to 20.5 m/s with a  $\pm 0.5$  m/s sliding window. Finally, the WS bins were further sorted into 73 relative wind direction bins corresponding to relative wind direction 5 to 355 degrees in  $\pm 5^\circ$  step. Relative wind direction bins for 0 and 360 degrees were extrapolated using a 2<sup>nd</sup> order fit. The binning scheme is illustrated in Fig. 4.2.

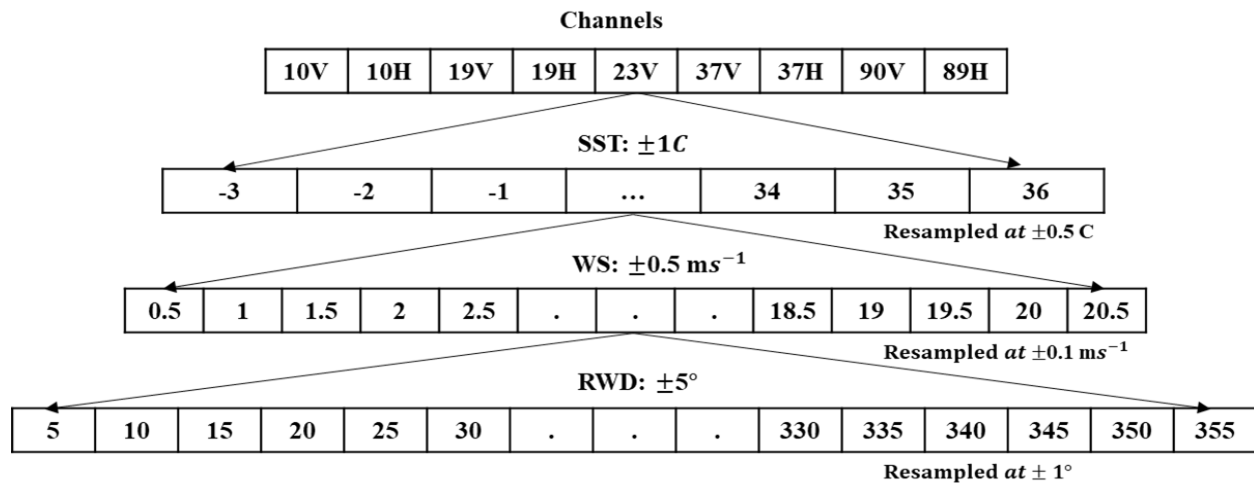


Figure 4.2: Binnig procedure for  $T_B$  and AV-H geophysical model function

#### 4.4: Brightness Temperature Signal

Sea surface temperature (SST) is the key element that comprises the most significant part of the  $T_B$  received by radiometers. Therefore,  $T_B$ s are strong function of SST and its variation. Figure 4.3 below shows the  $T_B$ s at nine frequency channels as a function of SST for three different WS, namely, 6, 20, and 14 m/s. The brightness temperature increases monotonically with SST for all WS at all nine frequencies. The SST signals are generally higher at H-pol channels (except for 10H) and increase with frequency for both polarizations. This is depicted in Fig. 4.4, which plots the same as Fig.4.3, with the mean removed.



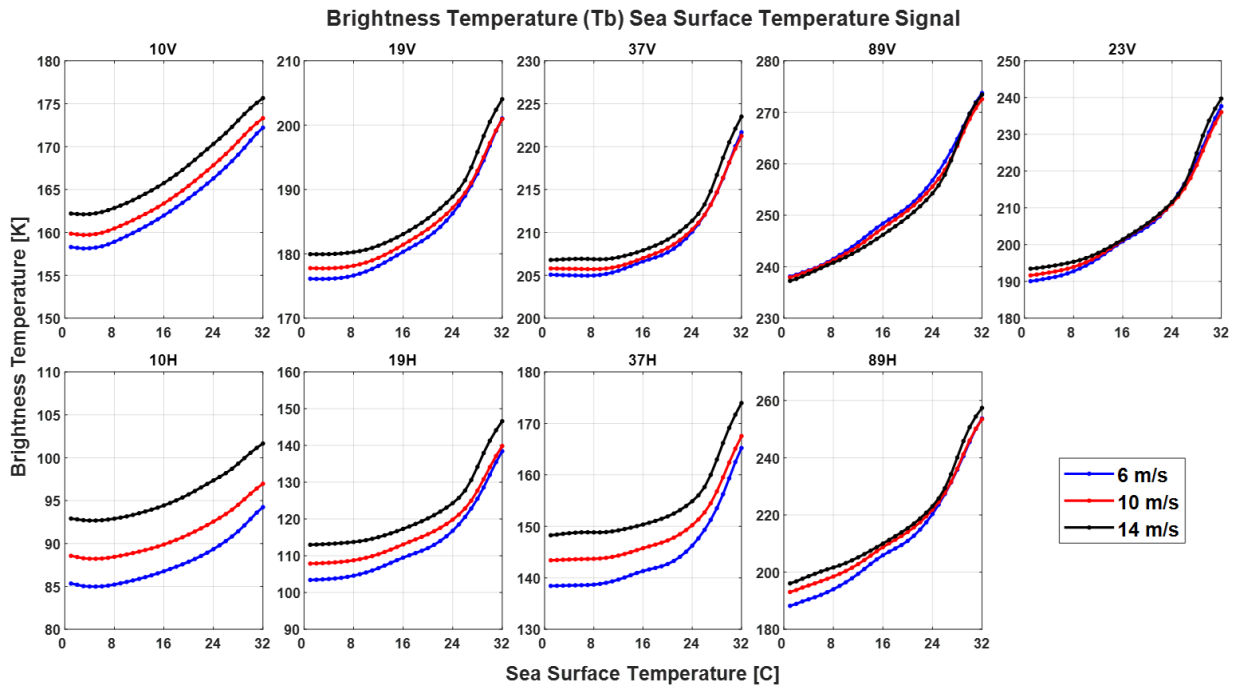


Figure 4.3: Sea surface temperature signature (SST) of GMI brightness temperature at nine lower frequency channels for wind speeds 6, 10, and 14  $\text{ms}^{-1}$ .

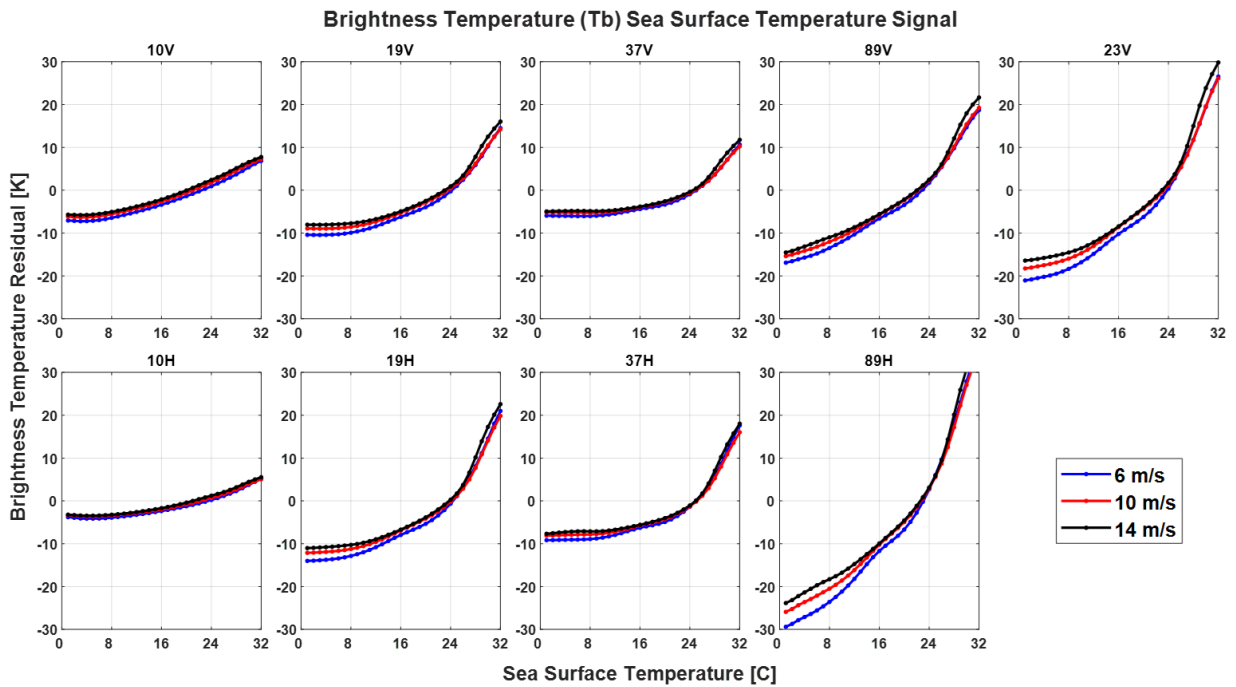


Figure 4.4: Sea surface temperature (SST) signal (with mean removed) of GMI brightness temperature at nine lower frequency channels for wind speeds 6, 10, and 14  $\text{ms}^{-1}$ .

Figure 4.5 below shows the brightness temperatures at nine frequency channels as a function of WS for four different SST, namely, 4, 12, 20, and 28C. As shown,  $T_B$ s also have a robust WS signature, especially in lower-frequency channels. H-pol channels have higher sensitivity than their V-pol counterparts. This is depicted in Fig. 4.6, which plots the same as Fig.4.5, with the mean removed. Figure 4.7 shows the brightness temperatures as a function of both WS and SST.

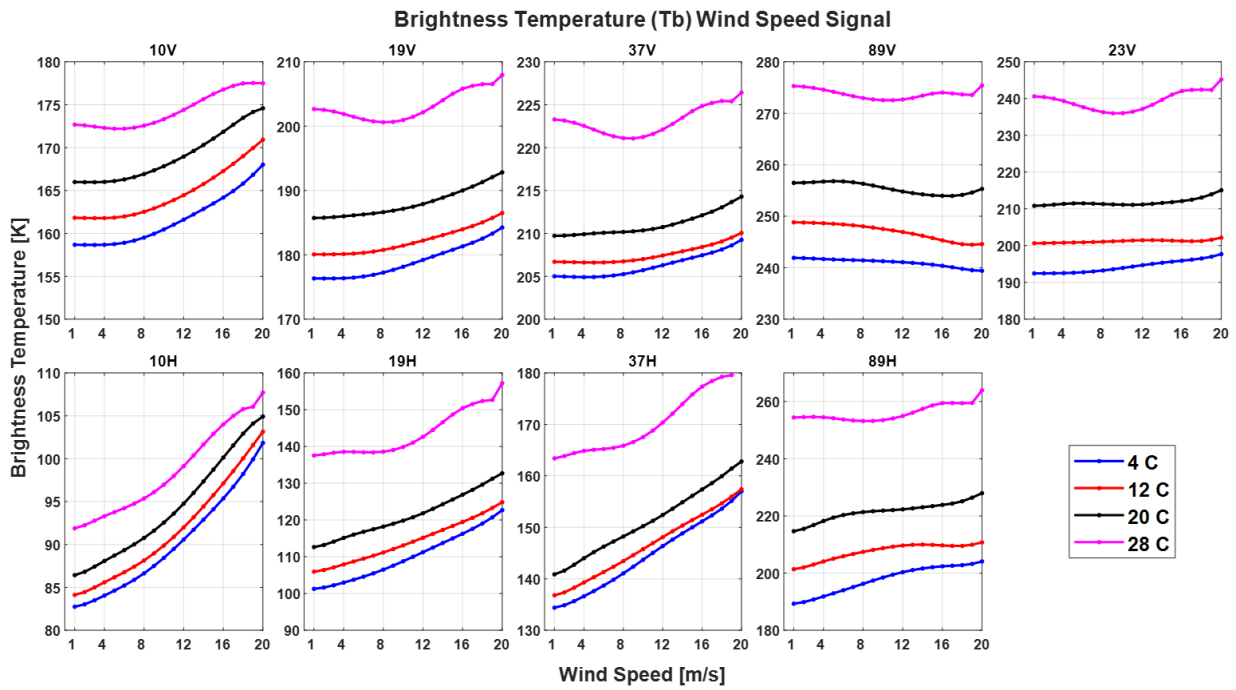


Figure 4.5: Wind speed (WS) signature of GMI brightness temperature at nine lower frequency channels for sea surface temperatures of 4, 12, 20, and 28 °C.

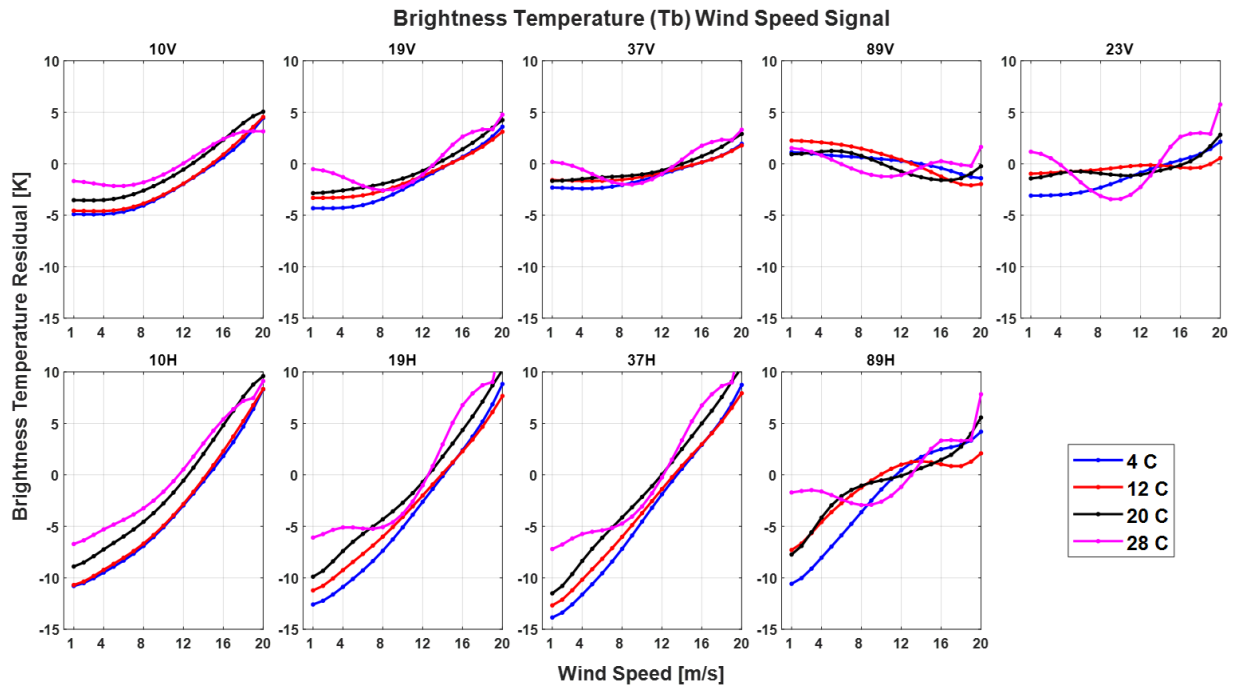


Figure 4.6: Wind speed (WS) signal (with mean removed) of GMI brightness temperature at nine lower frequency channels for sea surface temperatures of 4, 12, 20, and 28 °C.

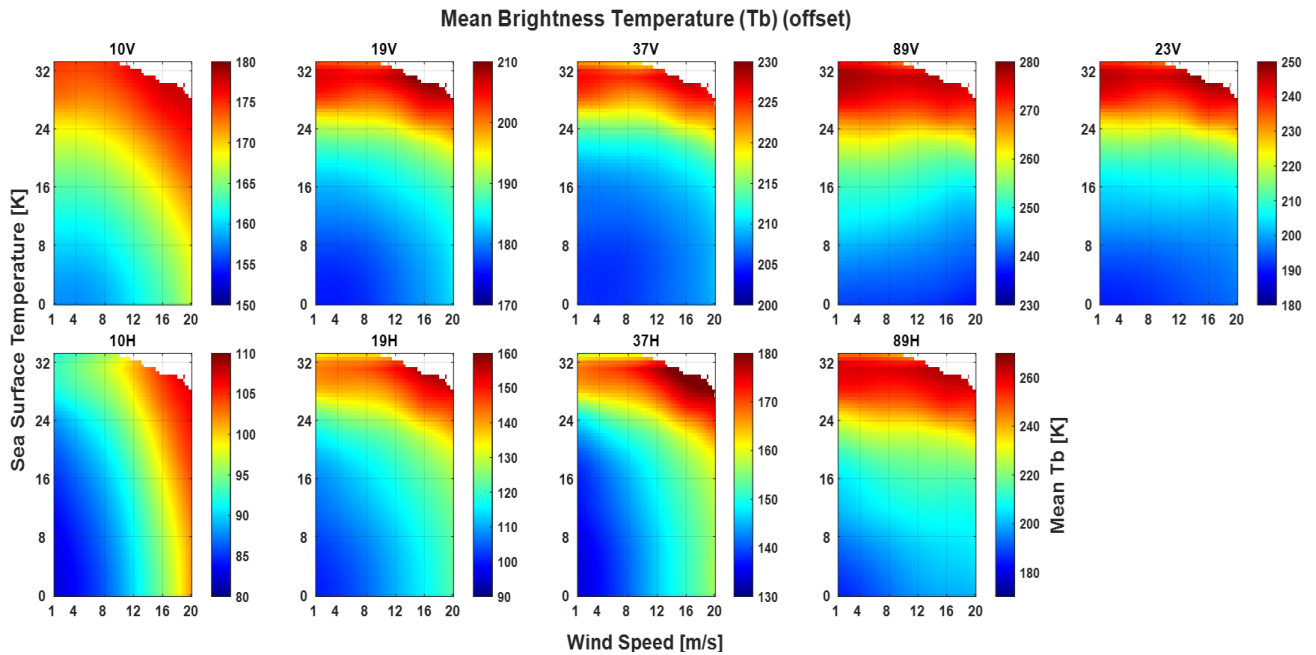


Figure 4.7: Wind speed (WS) signal and sea surface temperature (SST) dependence of GMI brightness temperature at nine lower frequency channels.

As described by [27], linearly polarized  $T_B$ s also have small but significant wind direction signals. Here, we present it for GMI channel frequencies in Fig. 4.8. Fig. 4.9 shows the directorial signals by removing the mean. As shown, the WD signals at V-pol channels are mainly dominated by first harmonics, while at H-pol channels, it is primarily by second harmonics. The directional signals are within the order of only a few K in all the channels.

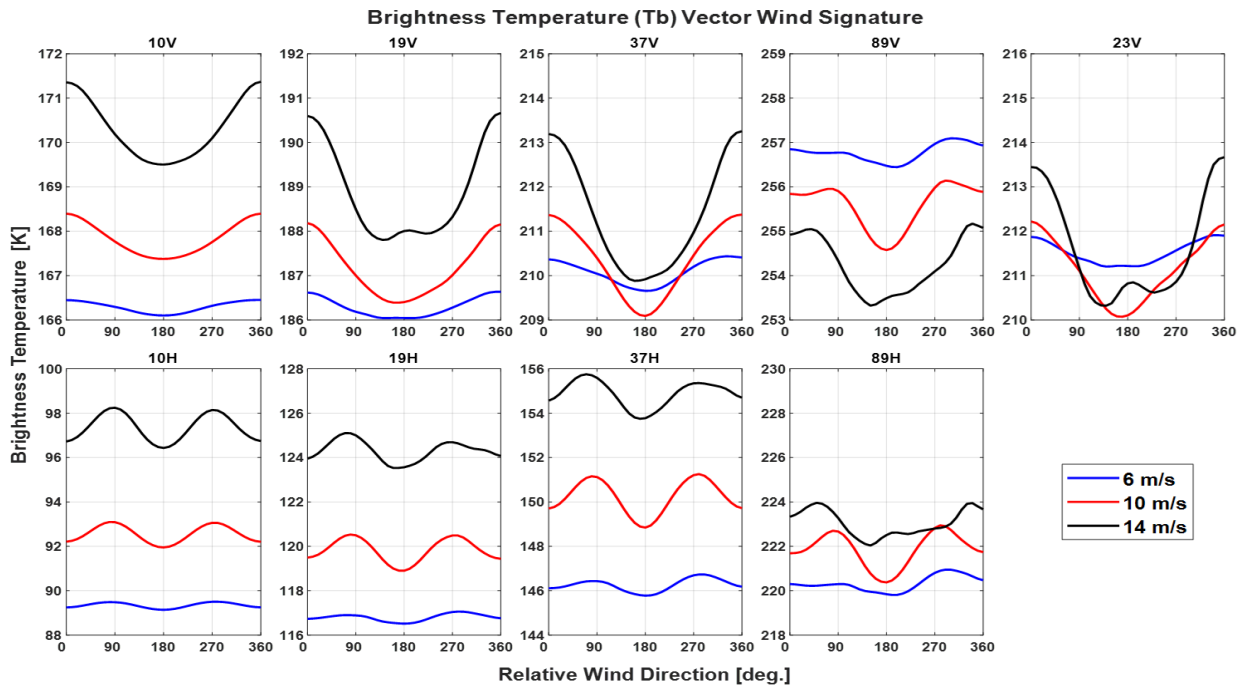


Figure 4.8: Wind direction (WD) signature of GMI brightness temperature at nine lower frequency channels for wind speed 6, 10, and  $14 \text{ ms}^{-1}$  at sea surface temperature of  $20 \text{ }^\circ\text{C}$ .

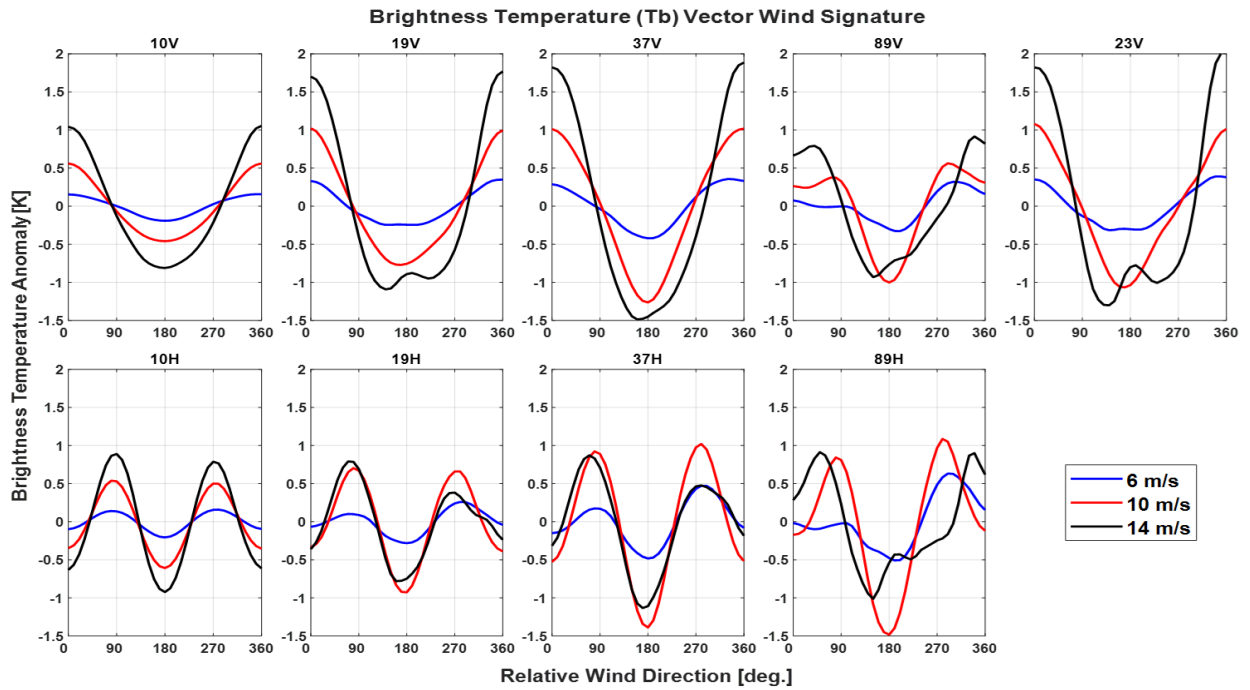


Figure 4.9: Wind direction (WD) signal (with DC terms removed) of GMI brightness temperature at nine lower frequency channels for wind speeds 6, 10, and 14  $\text{ms}^{-1}$  at sea surface temperature of 20  $^{\circ}\text{C}$ .

Figure 4.10 below presents the corresponding standard deviations of the binned average  $T_B$ s illustrated in Fig. 4.8. As shown, the statistical uncertainty is greater than the WD signals for all the channels, and the higher the frequency, the larger the effects. This is because atmospheric contaminations due to water vapor (WV) and cloud liquid (CLW) obscure these weak WD signals. Because of these contaminations and inherent measurement noise of the current radiometric systems (of the order of 1K), the WD retrieval from linearly polarized  $T_B$ s has not been possible. Polarimetric  $T_B$ s (3<sup>rd</sup> and 4<sup>th</sup> Stokes parameters), which are the differences in polarization ratios, are usually used for wind direction measurement in radiometer systems specialized for OVV purposes, like WindSat [122]. However, a linear weighted sum of horizontal and vertical pol  $T_B$ s expressed as  $AVH = (A * T_{BV} - T_{BH})$ , where “A” is an empirically derived coefficient, has been proved to provide an improved “ocean-signal” to “atmosphere-noise” ratio by mitigating the

overlying atmospheric influence [117], [123], [124]. This approach, called atmospheric clearing, forms the basis of our passive GMF. This is described in the next section.

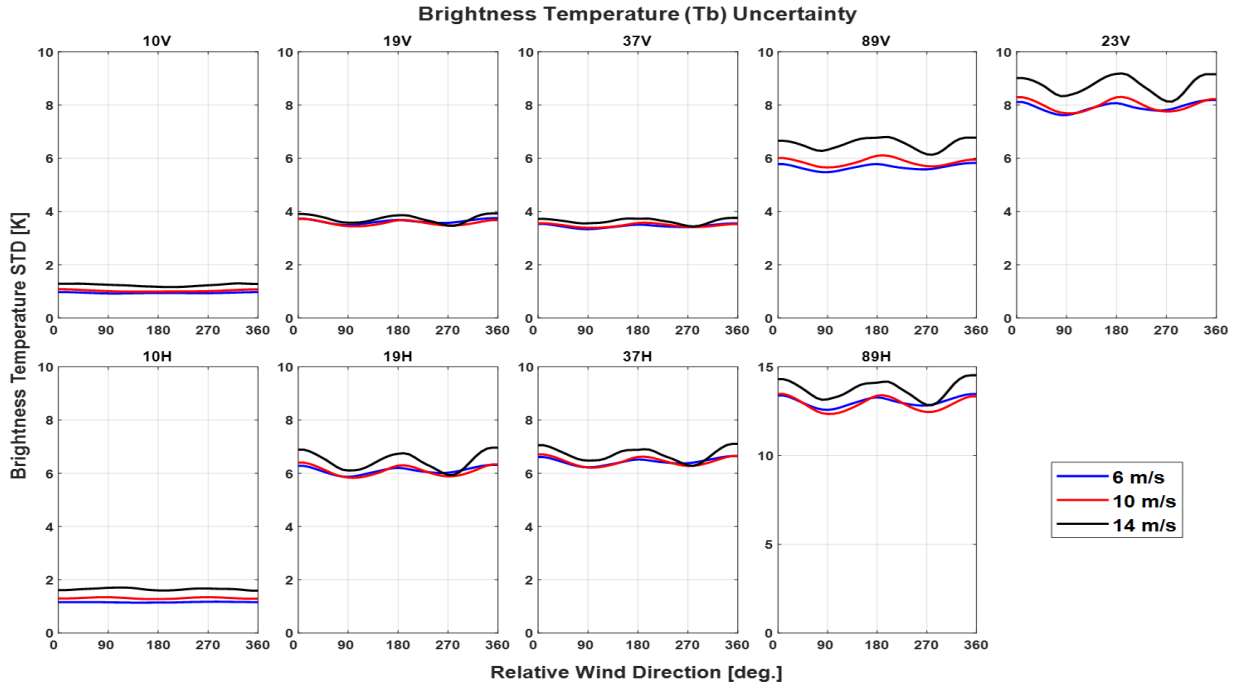


Figure 4.10: Standard deviations of GMI brightness temperature bins at nine lower frequency channels for wind speeds 6, 10, and 14  $\text{ms}^{-1}$  at sea surface temperature of 20  $^{\circ}\text{C}$ .

#### 4.5: Atmospheric Clearing

To mitigate the effects of atmospheric water vapor (WV) and cloud liquid water (CLW) on atmospheric transmittance, we used the linear combination of the linear polarized brightness temperatures (i.e., the modified 2<sup>nd</sup> Stokes parameters),  $A * T_{BV} - T_{BH}$  (to be called AV-H hereafter). Under clear sky conditions, the atmosphere can be assumed to be a single homogenous layer such that the atmospheric absorption  $\alpha(z)$  coefficient is a constant. The same assumption also results in a constant effective air temperature  $T_{eff}$  along the vertical profile, which is close to the surface temperature of the ocean,  $T_s$ , and remains constant along the vertical profile [29], [123].

$$T_{eff} \approx T(z) \cong T_s \quad (4.11)$$

$$a(z) \approx const = a$$

Thereby, Eqs. 4.2a and 4.2b simplify to

$$T_{BU} = T_{BD} = \alpha T_{eff} \int_0^S e^{-(\alpha.z)} dz = (1 - e^{-(\alpha.S)}) T_{eff} = (1 - \tau) T_{eff} \quad (4.12)$$

Substituting Eq. 4.12 into Eq. 4.1 results

$$T_B = T_{eff} - \tau^2 R T_{eff} + \tau R \Omega_{OVW} [(1 - \tau) T_{eff} + \tau T_{BC}] \quad (4.13)$$

Now, since the cold deep space brightness temperature,  $T_{BC}$ ,  $(1 - \tau)$ , roughness modification factor, are all very small numbers each; the combined effects of the third term in Eq. 4.13 is negligible and can thus be ignored. This results in a good approximation of  $T_B$

$$T_B \approx T_{eff} - \tau^2 R T_{eff} \quad (4.14)$$

For V- and H-polarized  $T_{BS}$ ,

$$T_{BV} \approx T_{eff} - \tau^2 R_V T_{eff} \quad (4.15a)$$

$$T_{BH} \approx T_{eff} - \tau^2 R_H T_{eff} \quad (4.15b)$$

We can derive a polarimetric reflectivity ratio 'A' such as:

$$A = \frac{R_H}{R_V} = \frac{T_{BH} - T_{eff}}{T_{BV} - T_{eff}} \approx \frac{T_{BH} - T_s}{T_{BV} - T_s} \quad (4.16)$$

Eq. 4.16 then provides a linear combination of  $T_{BS}$  such that:

$$AT_{BV} - T_{BH} = (A - 1) T_{eff} \approx (A - 1) T_s \quad (4.17)$$

The partial derivative of this combination with respect to the atmospheric transmittance turns out to be 0.

$$\frac{\partial(AT_{BV} - T_{BH})}{\partial\tau} \approx 0 \quad (4.18)$$

Therefore, the linear combination V- and H-pol brightness temperature,  $AV - H$ , is found to be independent of changes in atmospheric transmissivity mainly caused by variations in atmospheric WV and CLW under rain free conditions. This is the basis of the passive GMF of this dissertation, which is much less impacted by atmospheric contamination, unlike  $T_B$  of the individual channel. Figure 4.11 below shows the A parameters for 10, 19, 37, and 89 GHz channels as function of SST and WS. The A value for 10 GHz channel ranges between 1.5 to 1.7, and it increases with increasing frequency of the channels.

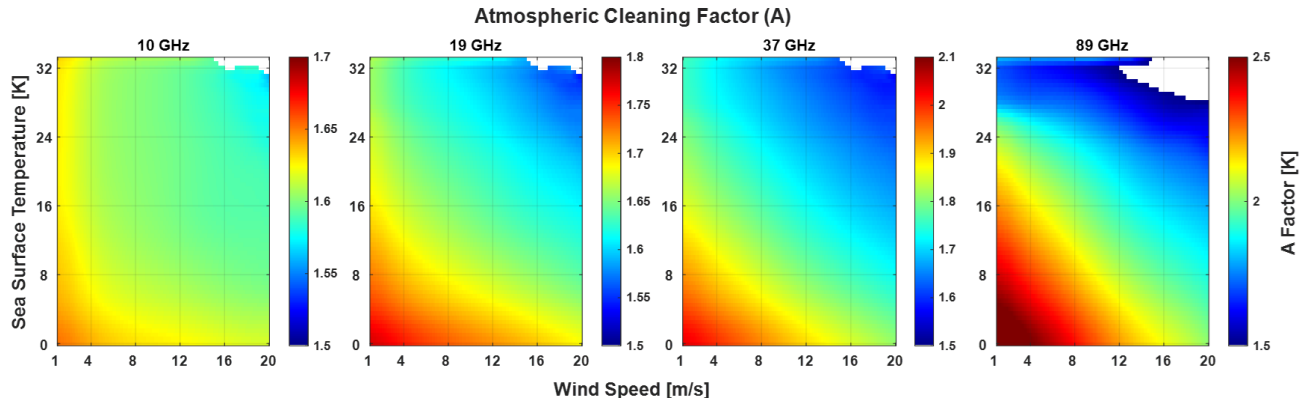


Figure 4.11: Atmospheric clearing factor (A) for 10, 19, 37, and 89 GHz GMI channels as a function of wind speeds and sea surface temperature.

#### 4.6: AV-H Geophysical Model Function

AV-H can be empirically modeled as,

$$\begin{aligned} AVH &= A * T_{BV} - T_{BH} \\ &= C_0(WS, SST) + C_1(WS, SST) * \cos(\chi) + C_2(WS, SST) * \cos(2\chi) \end{aligned} \quad (4.19)$$

where  $C_0(WS, SST)$  is the DC offset (to be called AVH DC here after) that depends on WS and SST for a particular frequency channel. When the DC offset is removed from AV-H in Eq. 4.19



with a priori WS (to be retrieved from GMI  $T_{BS}$  by regression analysis that is described in the next section) and SST, the  $AVH_{anomaly}$ , defines the AVH GMF as follows,

$$AVH\ GMF = AVH_{anomaly} = (A * T_{BV} - T_{BH}) - C_0(WS, SST) \quad (4.20)$$

$$AVH\ GMF = C_1(WS, SST) * \cos(\chi) + C_2(WS, SST) * \cos(2\chi) \quad (4.21)$$

where  $C_1$  and  $C_2$  are generally WS-dependent coefficients; however, as will be shown later in this section, they depend on SST at higher and lower SST.

To derive AVH GMFs, we used a similar binning procedure for the  $T_{BS}$  in the previous section, except that we binned weighted combinations of  $T_{BS}$  (i.e., AV-H) instead of  $T_{BS}$  (individual  $T_B$  for V and H pol.). Then the mean, over the relative wind direction, was subtracted to find GMF (anomalies) in tabular forms. Finally, for computational efficiency of retrieval, the GMF comprised 3D matrixes, as a function of WS, RWD, and SST, for each frequency channel.

Figure 4.12 shows the AVH (top panels) for WS 6, 10, and 14 m/s for 10, 19, 37, and 89 GHz channels and their corresponding anomalies (bottom panels) as a function of relative wind direction. As shown, the anomalies are a monotonic function of WS and biharmonic with relative wind direction, as in the case of conventional scatterometer GMF. However, unlike scatterometer GMF, AVH GMFs are led mainly by first harmonics, which reduces the ambiguity problems as in the case of biharmonic scatterometer GMFs.

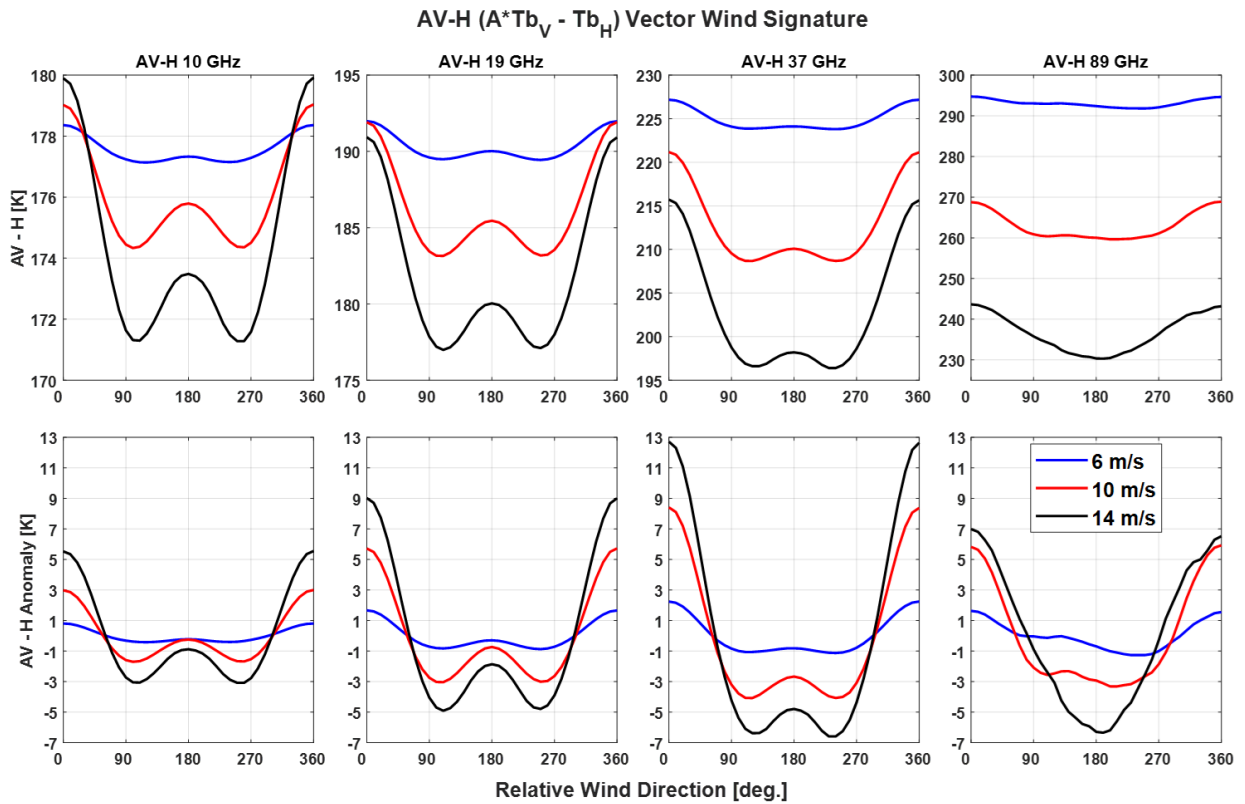


Figure 4.12: Wind direction (WD) signals of AV-H combinations at wind speeds 6, 10, and 14  $\text{ms}^{-1}$  and sea surface temperature of 20  $^{\circ}\text{C}$  for 10, 19, 37, and 89 GHz GMI channels as a function of relative wind direction.

Figure 4.13 shows the DC offset of the AVH channels as a function of both SST and WS. For all channels, except 10 GHz, the DC offset decreases with SST, while for 10 GHz channels, it decreases with SST for the lower SST but increases with higher SST. The mean values decrease almost linearly with WS for all frequency channels at all SST. These results are shown as a function of SST and WS individually in the top and bottom panels of Fig. 4.14, respectively. It should be noted that the DC offset is robust, but because it is a very large number (of order 100 - 200 K) with a large dynamic variability (between 50 K and 100 K) with SST and WS. This is a major concern for the development of a robust OVW retrieval algorithm that will be discussed further in future sections.

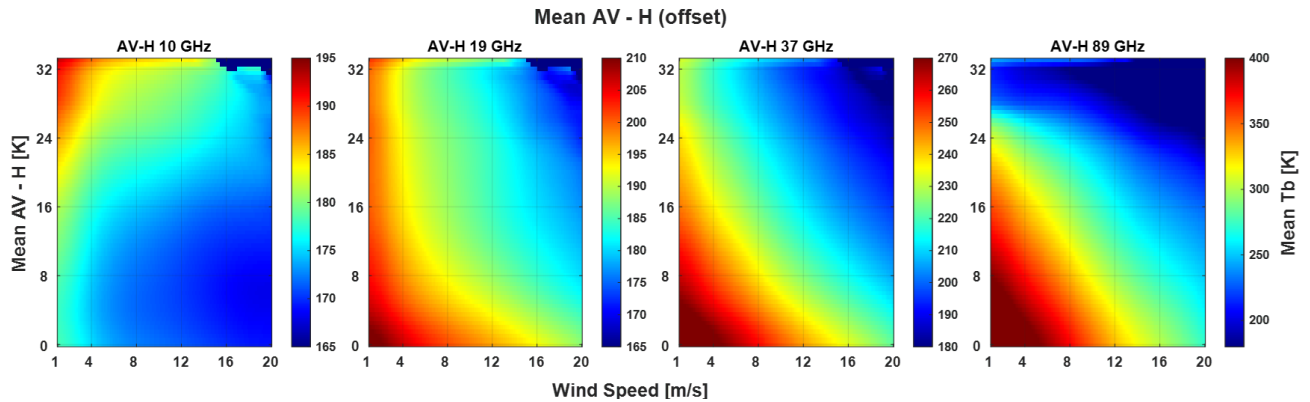


Figure 4.13: AV-H offset for 10, 19, 37, and 89 GHz GMI channels as a function of wind speeds and sea surface temperature.

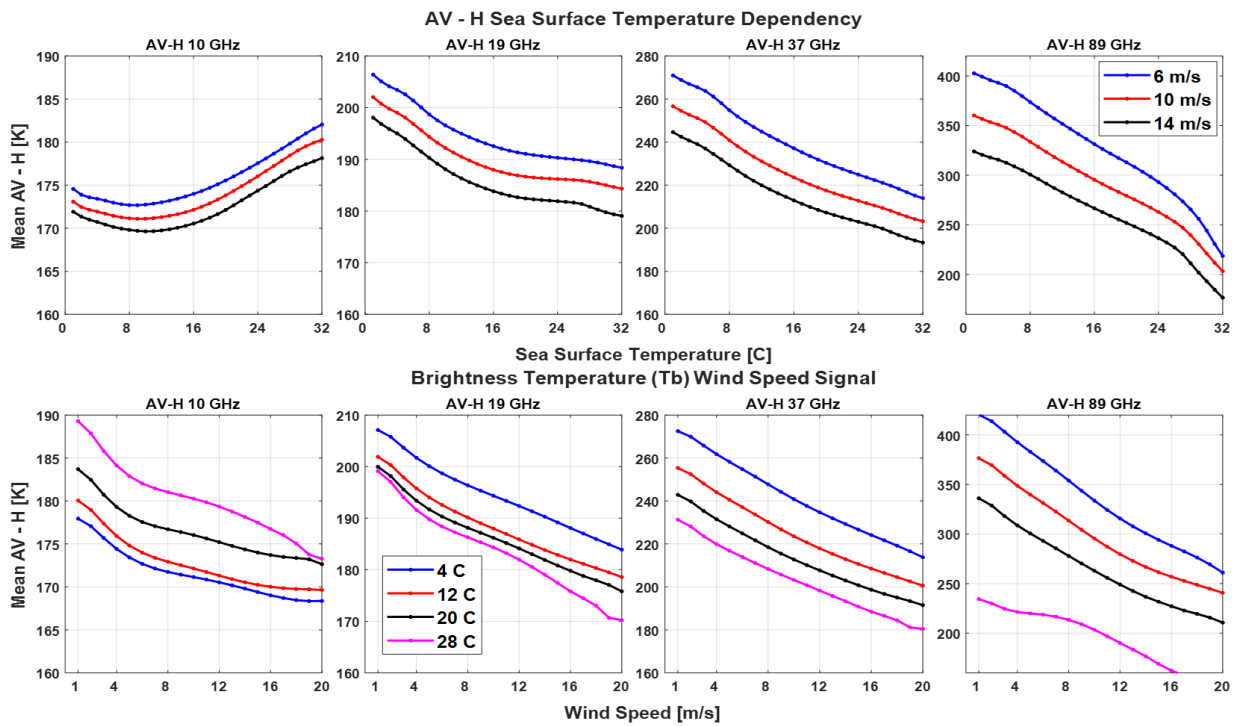


Figure 4.14: Sea surface temperature (SST) and wind speed (WS) dependence of AV-H offset for 10, 19, 37, and 89 GHz GMI channels. Mean AV-H are plotted as a function of SST (top) and WS (bottoms).

Now, Figure 4.15 depicts the STD of the AVH bins, corresponding to Fig. 4.12, as a function of relative wind direction for three different WS of 6, 10, and 14 m/s, at an SST of 20 C. As shown, the STDs are a small function of relative wind direction, WS and SST, and the mean STD increases with the frequency of the channels. It should be noted that STDs are too high for

the 89 GHz channel to be considered for WD retrieval purposes. However, the STDs are reasonable for other lower frequency channels considering their more robust WD signals, as shown in Fig. 4.12. This is illustrated in another way in Fig. 4.16 where the AV-H peak-to-peak directional signal and their uncertainty (mean STD) is presented as a function of WS. There are a few implications to notice. First, AV-H Peak-to-peak directional signal supersedes the uncertainty for moderate to higher WS regime for frequency channels other than 89 GHz. Therefore, WD retrieval from GMI channels 10, 19, and 37 GHz channels should be possible. For the 89 GHz channel, because the uncertainty  $\gg$  the WD signals, it is not included in our algorithm. Except for the high WS, the anomaly is not a function of SST; it is the only function of wind speed and direction.

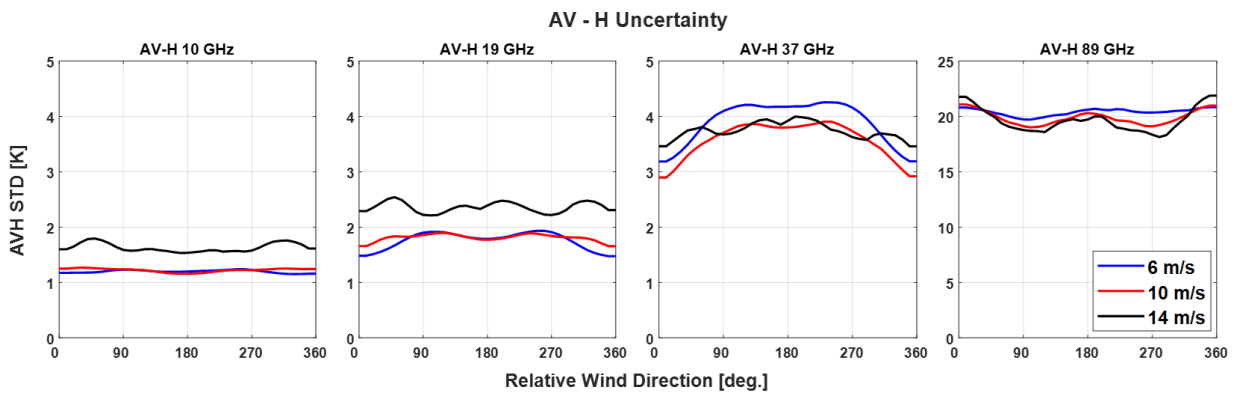


Figure 4.15: Standard deviations of AV-H bins at wind speeds 6, 10, and 14  $\text{ms}^{-1}$  and sea surface temperature of 20  $^{\circ}\text{C}$  for 10, 19, 37, and 89 GHz GMI channels as a function of relative wind direction.

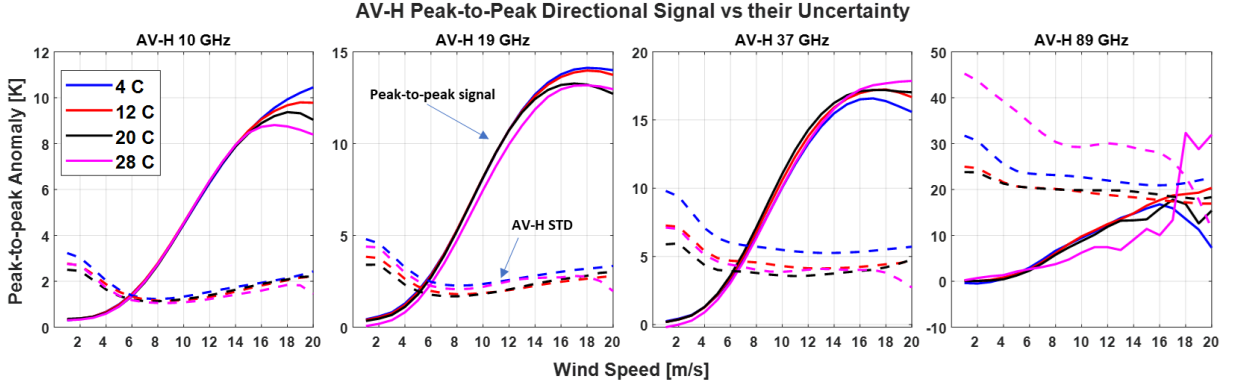


Figure 4.16: Peak-to-peak directional anisotropy and corresponding standard deviations of AV-H residuals at sea surface temperatures of 4, 12, 20, and 28 °C for 10, 19, 37, and 89 GHz GMI channels as a function of wind speed.

## 4.7: Wind Speed Retrieval Algorithm

### 4.7.1: Statistical Regression

A priori WS is required to determine the DC offset of AV-H. To obtain WS, we used a similar D-matrix algorithm by Connor and Chang [125] and Meissner and Wentz [126], [127] to retrieve WS from a linear combination of measured  $T_{Bn}$ , but under rain-free condition. The algorithm is given by,

$$WS = C_o + C_1 * T_{B1} + C_2 * T_{B2} + \dots + C_n * T_{Bn} \quad (4.22)$$

where  $T_{Bn}$  is the brightness temperature from nth channel, and the  $C_n$  coefficients are determined from regression analysis.

We evaluated different combinations of channels of GMI. The combination of all nine channels provided the best results for rain-free measurements. Therefore, our wind speed retrieval regression algorithm takes the following form.

$$\begin{aligned}
 WS = & C_0 + C_1 * T_{B10V} + C_2 * T_{B10H} + C_3 * T_{B19V} + C_4 * T_{B19H} + C_5 * T_{B22V} \\
 & + C_6 * T_{B37V} + C_7 * T_{B37H} + C_8 * T_{B89V} + C_9 * T_{B89H}
 \end{aligned}
 \tag{4.23}$$

The coefficients were found by fitting the  $T_B$  dataset to a linear model. 6 years (2015 to 2020) of  $T_B$  measurements were used, and the coefficients were determined in yearly basis, and the mean coefficients over the year was computed. The mean values of the coefficients are provided in Table 4.1 below.

Table 4.1: The Spectral Coefficients of GMI Wind Speed Retrieval Algorithm

Channels	Coefficients	Value
Const.	$C_0$	88.1816
10V	$C_1$	-0.9906
10H	$C_2$	1.2877
19V	$C_3$	1.2899
19H	$C_4$	-0.6525
23V	$C_5$	-0.0395
37V	$C_6$	-1.2328
37H	$C_7$	0.4376
89V	$C_8$	-0.0158
89H	$C_9$	0.0501

## CHAPTER 5: COMBINED ACTIVE AND PASSIVE OVW RETRIEVAL ALGORITHM

### 5.1: Introduction

Given set of observations within a wind vector cell (WVC), the purpose of the OVW retrieval algorithm is to obtain the best estimate of the ocean vector wind, using a previously derived or trained forward model function  $f$ .

$$y = f(x) \tag{5.1}$$

where  $y$  is the mean of the top-of-the atmosphere (TOA) observations over a WVC and  $x$  is the state variables (e.g., the vector wind at 10-m neutral height,  $U_{10}$ , and other geophysical variables,  $Q$ ). The forward model  $f$  is called the geophysical model function (GMF).

Therefore, for a given set of observations,  $y$ , and a well-tuned GMF, the problem in Eq. 5.1 is an inverse optimization problem. There are many well-known techniques for inversion, including analytical, statistical (such as Bayes' theory based), and least square approaches [45], [46], [64], [76]. However, the inversion procedure for OVW is highly non-linear [46], [61], [73], [128]–[130]. Consequently, the Bayesian non-linear optimization technique, mainly the maximum-likelihood estimation (MLE) technique, is usually used by the OVW community [65], [66]. This chapter discusses the MLE technique and the MLE-based combined active and passive (CAP) algorithm used for OVW retrieval.

### 5.2: Maximum Likelihood Estimation

The MLE is a Bayesian optimization technique that maximizes the likelihood of the “true” wind by minimizing a cost function. Generally, Bayes' theory relates the posterior probability of occurrence of a true state,  $x_t$ , for a given set of observations,  $y_o$ , as a function of the prior

probability of occurrence of the true state  $x_t$ , and the probability of the observation,  $y_o$ , for a known state,  $x_t$ , by Eq. 5.2.

$$P(x_t|y_o) = \frac{P(y_o|x_t) * P(x_t)}{P(y_o)} \quad (5.2)$$

where,

$P(x_t|y_o)$  = the probability of occurrence of true state,  $x_t$ , given that the observation,  $y_o$ , has been recorded

$P(x_t)$  = the prior probability of an event  $x_t$

$P(y_o)$  = the probability of an event  $y_o$ , and

$P(y_o|x_t)$  = the probability of occurring the observation,  $y_o$ , for a given true state,  $x_t$

The probabilities  $P(x_t), P(y_o)$  are independent of each other and are set to constant for OVW retrieval from a particular instrument. Hence, the posterior probability,  $P(y_o|x_t)$ , can be fully characterized in terms of  $P(y_o|x_t)$ . However, it depends on the uncertainty associated with the observation itself and the uncertainty in the forward modeling (through GMF). It results,

$$P(x_t|y_o) \propto P(y_o|x_t) = \int P_o(y_t - y_o) \cdot P_f(y_t - f(x)) dy_t = P_{of}(y_o - f(x)) \quad (5.3)$$

where  $y_t$  is the true observation,  $P_o$  and  $P_f$  are the random errors associated with the observation and GMF respectively. For ocean surface, the central limit theorem, these random errors are Gaussian in nature [46], [131], [132], and therefore, Eq. 5.3 can be approximated as

$$P(x_t|y_o) \propto \exp\left[-\frac{1}{2} \{y_o - f(x)\}^T (O + F)^{-1} \{y_o - f(x)\}\right] \quad (5.4)$$

Here  $O$  and  $F$  are the covariant matrixes of  $P_o$  and  $P_f$ , respectively. Now, since maximizing  $P(x_t|y_o)$  is equivalent to minimizing  $-\ln([P(x_t|y_o)])$ , the maximum likelihood estimator (MLE) can be written as:



$$MLE = \{y_o - f(x)\}^T (O + F)^{-1} \{y_o - f(x)\} \quad (5.5)$$

$y_o$  in Eq. 5.5 represents the measurements, and the forward model,  $f(x)$ , represents the GMF.

The GMF is generally assumed to be perfect (say  $F \approx 0$ ), and measurements are assumed uncorrelated ( $O$  is thus a diagonal matrix). With these assumptions, the MLE for OVW is thus defined as,

$$MLE(OVW) = \frac{1}{N} \sum_{i=1}^N \frac{[Measurement - Model]^2}{Measurement\ variance} \quad (5.6)$$

where  $N$  is the number of available measurements in a WVC.

### 5.3: Retrieval Algorithm

The procedure for the combined active-passive (CAP) OVW retrieval is outlined in Fig. 5.1. The basis of this algorithm is the MLE inversion, which is defined as,

$$MLE(OVW) = \left[ \sum_{i=1}^M \left( \frac{1}{N} \sum_{j=1}^{NB} \frac{[\sigma_{meas,ij}^0 - GMF_{\sigma_{ij}^0}(EIA, SST)]^2}{var\sigma_{meas,ij}^0} \right) \right]_{n \times n} \quad (5.7)$$

$$+ \left[ \sum_{k=1}^L \left( \frac{[(AV - H)_{meas,k} - GMF_{AVH,k}(SST)]^2}{NEDT_k} \right) \right]_{n \times n}$$

The first term in Eq. 5.7 is the active part of the MLE, which consists of GPM Ku- and Ka-band GMFs and measurements.  $M$  represents the number of bands, and  $NB$  indicates the number of beams for each band used in the algorithm.  $M=2$  for DPR, and there are 49 beam positions with corresponding Earth incidence angles (EIA) for each band. We evaluated the performance of all the beams, but considering directional sensitivity, we selected 18 outer beam positions from each

side of the swath for our wind direction retrieval algorithm. So,  $NB = 36$ . Two versions of GMFs were used for DPR for performance evaluations; one used the SST information as a priory, called the SST dependent DPR GMF, and the other was SST independent (tuned and used in retrieval without giving SST information, can be termed as SST averaged). Since the absolute values of  $\sigma^0$  at both bands are different due to a spectral difference, the MLE at each band is first normalized to its 2D global maximum. Then the normalized MLE is added for both bands and normalized in a similar way before adding it to its passive counterpart resulting from the second term. The subscript  $n$  signifies this normalization process. The passive equivalent MLE in the second term follows a similar procedure. For every frequency channel, the distance between the AV-H measurements (linear combination of V- and H-pol  $T_B$ s as defined in Chapter 4) and its GMF is normalized by the on-orbit noise equivalent delta temperature (NEDT) of the individual channel. Because the spectral response of different frequency channels is significantly different, the MLE of each channel is normalized to its maximum value before summing up. Various combinations of 3 lower frequency channels (10, 19, and 37 GHz) were used, and the retrieval performance of each combination was evaluated. Therefore, the values of L range between 1 and 3. Finally, since the  $\sigma^0$  and the  $T_B$ s are different quantities, normalized values of active and passive MLEs were added to find the combined MLE. The combined MLE was transformed in dB space to obtain the cost function described as follows.

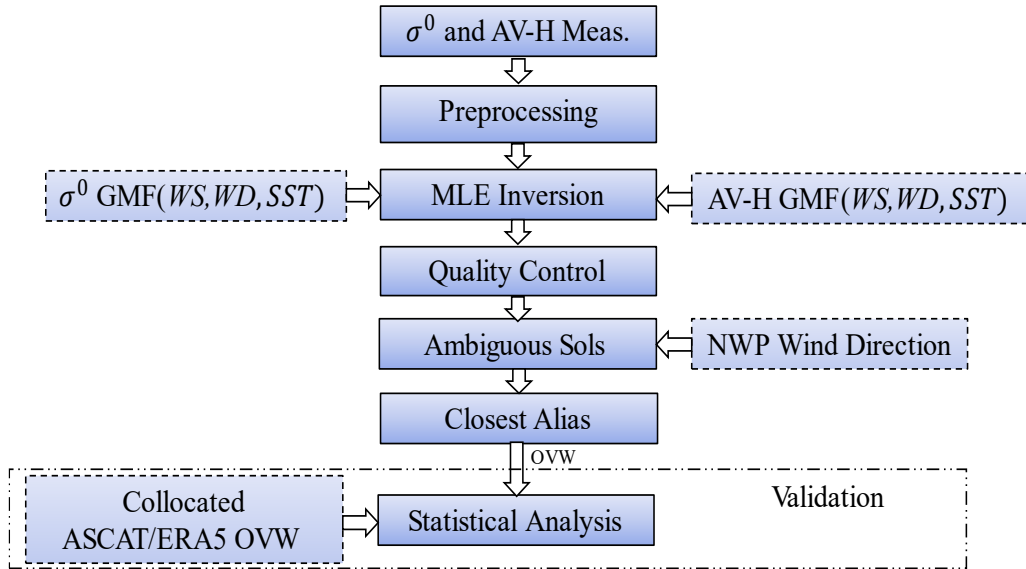


Figure 5.1: Combined active and passive OVW retrieval algorithm.

The MLE surfaces for a typical WVC are shown in Fig. 5.2 for KuPR (top left panel), KaPR (top right panel), -and 3 AVH channels (bottom panels). For each panel, the color scale represents the cost function normalized residuals in dB, and the x- and y-axes are the relative WD ( $0^\circ \leq \chi \leq 360^\circ$ ) and WS ( $1 \leq WS \leq 20$  m/s), respectively. Note, the top panels plot the MLE residual as a function of wind direction relative to PR azimuth look (same for both PR), while at the bottom panels, it is relative to GMI azimuth look, which is around  $\sim 75^\circ$  off for the same WVC. The DPR MLE comprises  $\sigma^0$  measurements from multiple PR beams present for that particular WVC. As shown, the minima (blue) show the loci of possible solutions, which are unrealistically extended in both directions, for both DPR and AVH combinations. Therefore, when used individually, an unambiguous vector wind is not possible from either of these. However, the complementary active and passive combinations reduce this ambiguity significantly when added together. This is illustrated for the same WVC in Fig. 5.3. The AVH MLE surfaces were translated circularly to

match the relative wind direction with DPR and then added together, which forms the combined MLE surfaces presented in the bottom panels for different spectral combinations.

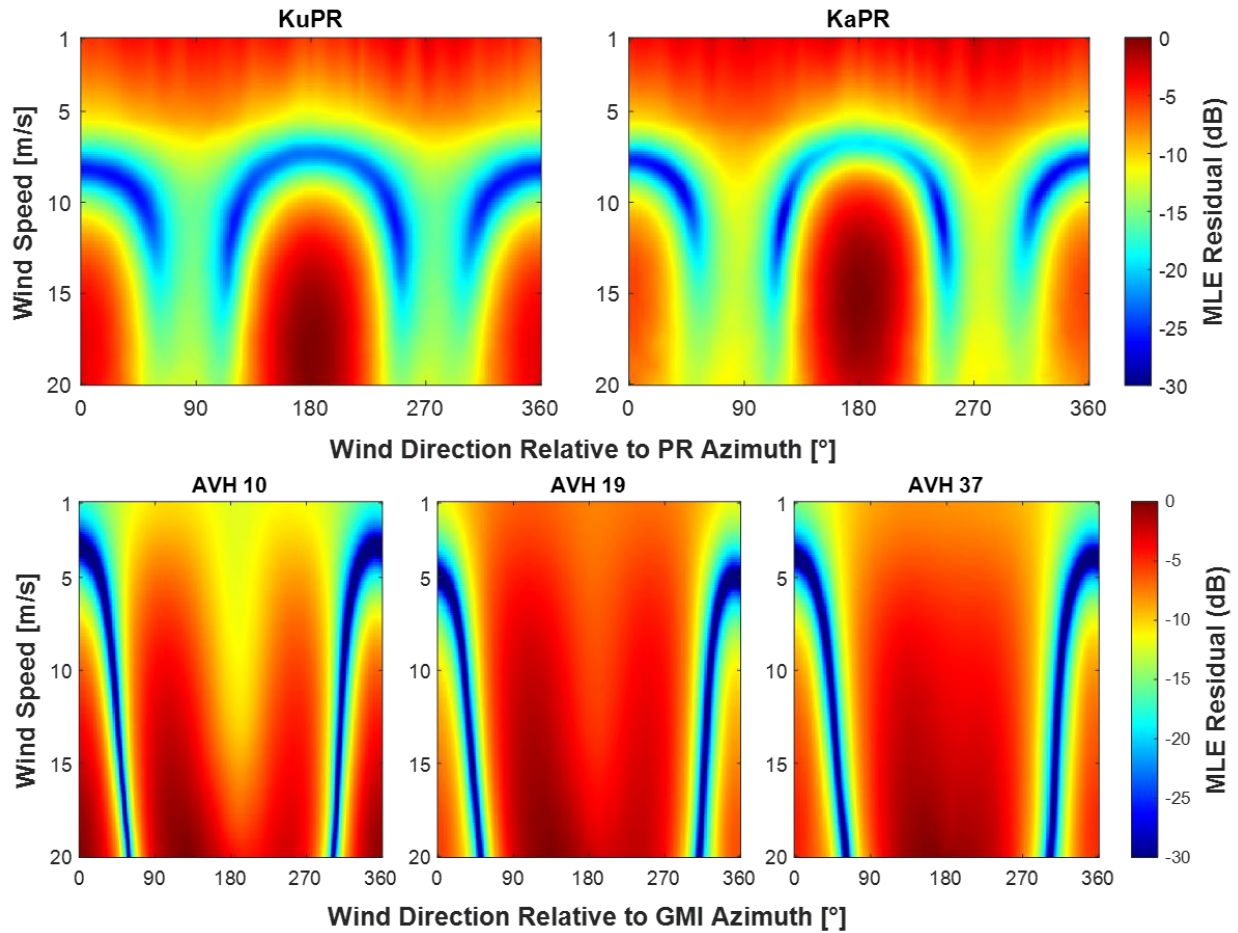


Figure 5.2: Example MLE surfaces -- active (top) and passive (bottom)

The left-most Fig. 5.3 in the bottom panels represents the MLE of spectral combinations of 10 GHz AVH and KuPR  $\sigma^0$  measurements. The next one adds 19 GHz AVH to this. The third on the bottom panel presents the combined MLE from Ku- and Ka-PR, 10 and 19 GHz AVH  $T_B$ s. The fourth one (the rightmost in the bottom panel) adds the 37 GHz AVH  $T_B$ s to the previous combination. The two dark blue contours are the MLE residual minima corresponding to the two

most probable solutions (aliases). Because of the biharmonic nature of the GMFs, ambiguities are inherent in GMF inversion. Typically, two to four aliases occur within the range of  $360^\circ$ . Thus, for a given WVC, the OVW retrieval results in up to four-possible wind vectors, of which one is the correct choice. This wind vector ambiguity structure is very similar to that produced by multi-azimuth wind-measuring satellite scatterometers,

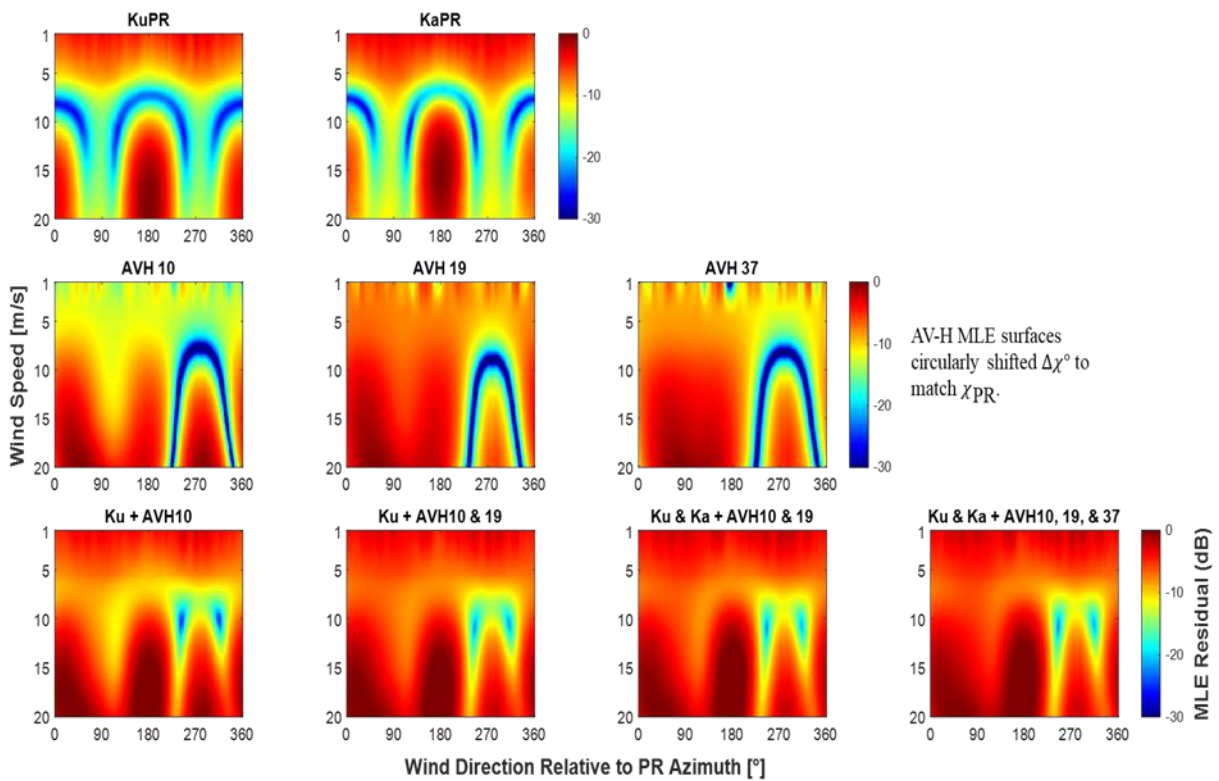


Figure 5.3: Example MLE surfaces -- active (top row) and passive, which are circularly shifted to match the azimuth with active counterpart (middle row), and different combination of active and passive MLE (bottom row); the leftmost is the combination of Ku-band PR and 10 GHz AV-H, the next is the same except it adds the 19 GHz AV-H MLE. The following one (3<sup>rd</sup> row, 3<sup>rd</sup> column) adds Ka-band MLE with the previous one, and finally, the rightmost on the bottom panel shows the combination of MLEs from Ku- and Ka-band, and 10,19, and 37 GHz AV-H MLEs.

Next, the cost function for each of the above-mentioned combinations was evaluated using the similar algorithm used by NASA JPL for QuickScat and RapidScat wind processing [65], [133], [134]. In that algorithm, the minimum along WS for each wind direction is located, which

gives a 1D cost function as a function of relative wind direction. Then the likelihood of each possible WD solution was computed by converting the objective function to pseudoprobability function as.

$$P(U, \chi) = \frac{1}{k} \exp[-F_{obj}(U, \chi)] \quad (5.8)$$

where  $P(U, \chi)$  represents pseudoprobabilities of a finite set of relative wind directions,  $\chi$ , for an averaged WS  $U$ , and  $F_{obj}(U, \chi)$  is their objective function, and  $k$  is a constant that depends on the instruments.

Figure 5.4 illustrates the procedure for the same WVC presented earlier. Panel (a) represents one of the combined MLE surfaces from Fig 5.3. The solid blue line in Fig. 5.4b represents the cost function found along the loci of WS minima. The corresponding WS is depicted in the same Fig. by black dots (right side y-axis), and the average of these WS is recorded as the average WS found from MLE, as represented by a straight yellow line parallel to the x-axis. The subpanel (c) in the same Fig. presents the relative prominences of the ambiguities as found from the objective function and the peaks of its probability density function as determined from Eq. 5.8. Black vertical lines present the relative probabilities of relative wind direction,  $\chi$ , for an averaged WS  $U$ . The highest relative likelihood is associated with the first-rank solution (deepest minima), which would be the ideal instrument's true solution. However, in reality, the deepest minima, or the 1<sup>st</sup> rank solutions, are not always the true solutions, depending on instrument skill, which is defined as the percentage of the times the 1<sup>st</sup> rank solution is the true solution in a large number of retrievals. Therefore, a threshold in relative probability is usually set (1% for our case) to remove the directional noise that results in one to four most probable solutions, which are then subject to an ambiguity removal algorithm for determining the correct solution.

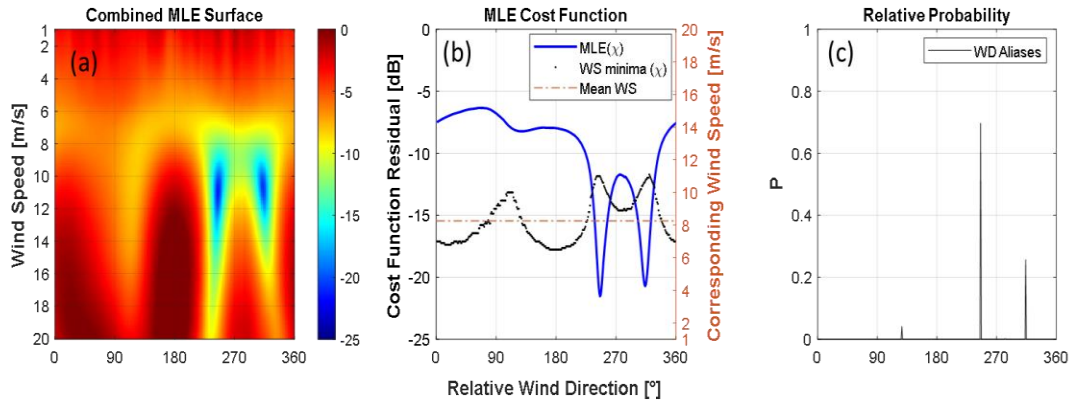


Figure 5.4: MLE cost function and probable solutions

### 5.3.1: Ambiguity Removal

The ambiguity removal algorithm aims to select the best candidate solution from a set of ambiguous or probable solutions based on spatial consistency constraints. Two main approaches that the OVW community mostly follow -- median filtering based AR techniques [65], [66], [134], [135], and two-dimensional variational ambiguity removal technique (2DVAR) [61], [129], [136]–[139].

In median filtering-based techniques, weighted cost function residual is nudged with Numerical Weather Prediction (NWP) model wind fields to select the most probable WD. The process is initiated with the ambiguity value closest to NWP wind vector field and then the selection is iteratively adjusted for each WVC to match the direction closest to the median WD of the surrounding WVCs. The process continues until the selections converge, resulting in the final WD solution.

In 2DVAR AR technique, the observations and NWP background information are merged through a two-dimensional variational technique, like those employed in meteorological data assimilation, to produce an ‘analysis’ wind field. Then, for every WVC, the closest ambiguity to the ‘analysis’ field is chosen as the final WD candidate. So, 2DVAR accounts for background error.

However, in this dissertation, the closest solution to the surface truth reference (ERA5 NWP and ASCAT wind filed) was selected to evaluate the performance of the CAP retrieval algorithm. This is illustrated in Fig. 5.1.



## CHAPTER 6: RESULTS AND DISCUSSION

### 6.1: Introduction

In this chapter, we compare the wind speed and direction retrieval results with ERA5 and ASCAT-B winds. ASCAT-B is a C- band scatterometer that flies onboard the European Organization for the Exploitation of Meteorological Satellites (EUMETSAT) MetOp-B satellite; and provides wind vector measurements over the ocean [140]. ASCAT is on a polar non-sun synchronous orbit and, thus, provides regular collocations with GPM.

### 6.2: Validation

#### 6.2.1: Validation Matchup Dataset

The match-up dataset consisted of 1-year (2021) of independent (not used in GMF development) DPR and GMI datasets, which were spatially and temporally collocated with independent “surface truth” OVW observations. These independent OVW's were from near concurrent (within  $\pm 30$  min) ocean winds from the ERA5 reanalysis NWP and from ASCAT scatterometer retrievals onboard MetOp-B satellite. The ASCAT Version 2.1 daily gridded wind product (on a  $0.25^\circ$  longitude x  $0.25^\circ$  latitude grid) from the Remote Sensing System (RSS) [141] were used. The corresponding ERA5 products were resampled to the same grid resolution, and the GMI and DPR data gridding and retrieval were also performed with the same spatial resolution (25 km). The temporal collocation window was set to  $\pm 30$  min, and all regular quality flags (including land, ice, and rain), similar to the ones used for GMF development in Chapters 2 and 3, were used. Since the GPM is in a non-sun synchronous inclined orbit ( $65^\circ$  inclination), and MetOp-B is in a sun-synchronous polar orbit ( $98.7^\circ$  inclination), GPM crosses MetOp-B in every orbit, which facilitates frequent collocation.

Retrieval and validation were performed for collocated DPR and GMI swath (~245 km central swath of GMI). One year of such GPM-ASCAT collocations resulted in about 0.87 million of 25 km boxes that covers the full dynamic range of possible oceanic states. Figure 6.1 shows the geographical distributions of the validation dataset with associated longitude and latitudinal histograms.

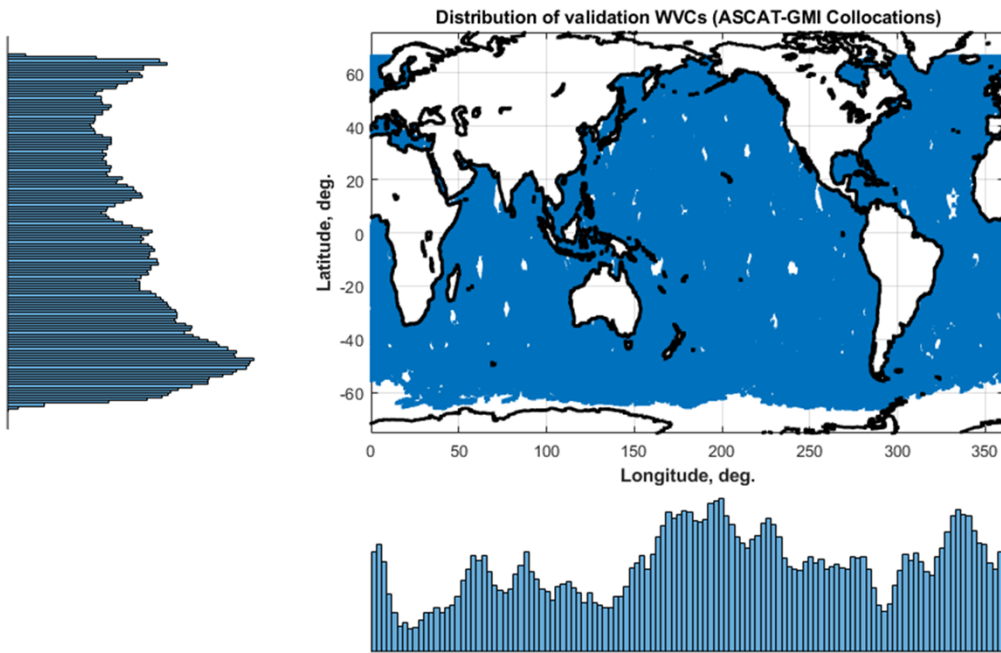


Figure 6.1: Distribution of validation dataset

### 6.2.2: Wind Speed Validation

The wind speed for the collocated data set was computed from the regression analysis of a linear combination of GMI  $T_{BS}$  from 9 lower frequency channels. Figure 6.2 compares the retrieved WS with the collocated WS from ERA5 (top panels) and ASCAT-B (bottom panels), where a  $2\sigma$  filter was used to remove the outliers. From the leftmost panels, it is seen that there is a very high correlation between the retrieved winds, as evidenced by the high correlation ratio

( $>0.96$ ). The color in the scatter plot shows the density of the WS in the validation dataset, and the black dashed dot line is a 45-degree reference line for visual convenience. The differences between the retrieved WS and the ERA5 and ASCAT WS are shown as the histogram of the differences at the middle top and bottom panels, respectively. As shown, the difference with ERA5 is almost 0 mean Gaussian distribution with an STD less than 1 m/s. On the other hand, the STD of differences with ASCAT winds is somewhat superior. However, there is a slight mean bias of  $\sim 0.25$  m/s between ASCAT WS and retrieved WS. ERA5 WS (separate and independent dataset) was used for tuning the algorithm, and this might have favored not having a systematic bias. However, the uncertainty is in better agreement with ASCAT. The rightmost panels in the same Fig. present the root mean square error (RMSE) as a function of ERA5 (top panel) and ASCAT (bottom panel) WS. As observed, RMSE increases with WS for  $WS > 6$  m/s. This WS was used to find the AVH DC offset as required by the MLE algorithm described in Chapter 5.

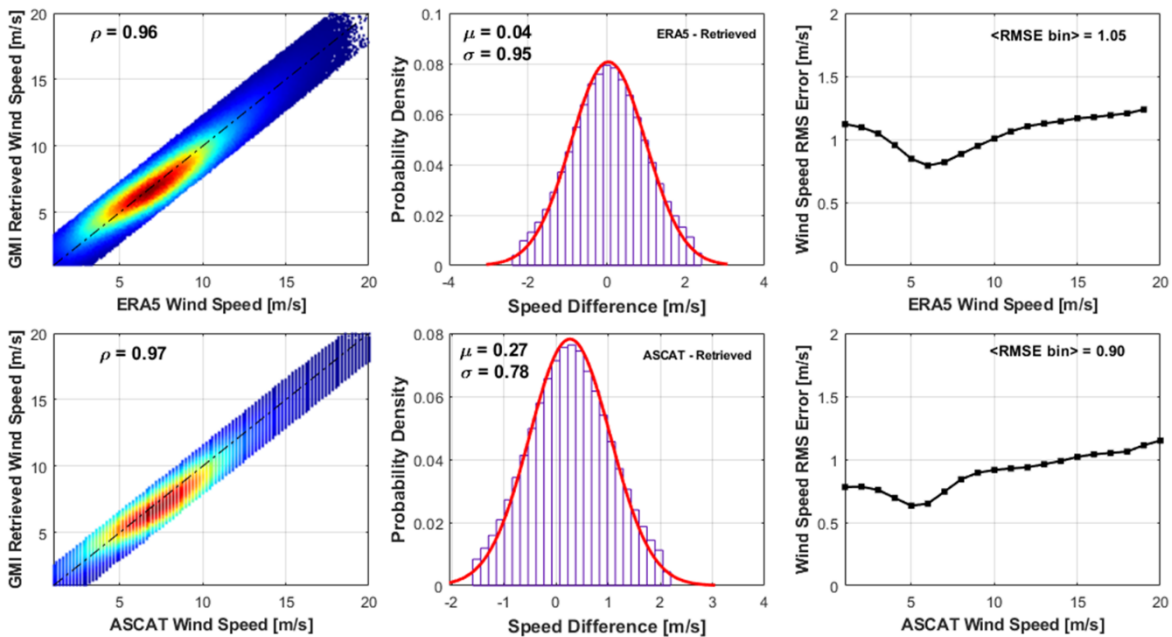


Figure 6.2: GMI wind speed retrieval performance

Figure 6.3 presents the same results as Fig. 6.2; except now, the WS was found by averaging the MLE cost function. As shown, the MLE WS results are much inferior to the WS found from GMI regression analysis. There is a significant systematic bias (order of  $\sim 0.5$  m/s) and significantly higher uncertainty. This is mainly due to the DPR transition region in the middle of the swath locations, where  $\sigma^0$  becomes insensitive to WS. That affects the accuracy of the overall combined (CAP) algorithm. However, the results are within the science requirements (STD < 2 m/s) for WS measurements. Nevertheless, since the GMI retrieved WS is superior to the CAP WS, we recommend considering the GMI WS as the magnitude of the retrieved OVW.

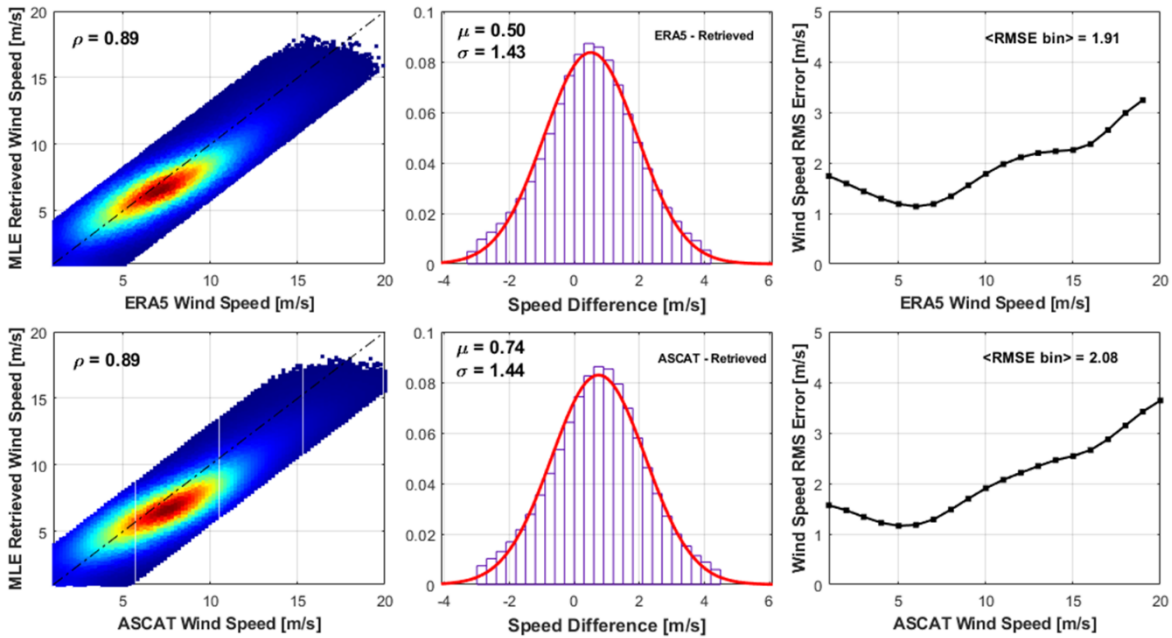


Figure 6.3: MLE wind speed retrieval performance

### 6.2.3: Wind Direction Validation

The wind direction validation results are presented in Fig. 6.4 similar to the previous section. The left column shows the scatter diagrams between the retrieved WD solution closest to the surface truth reference – ERA5 for the top panel and ASCAT for the bottom panel. As

indicated, the correlation coefficient with both references is  $> 0.7$ . The color on the scatter plots represents the density of WD in the validation dataset, where we see the domination of trade winds (easterly) around the tropical area and the westerlies in extra-tropics (around the latitude  $60^{\circ}\text{S/N}$ ). The histogram in the middle panel indicates the differences between the retrieved WD closest to the surface truth and the surface truth WD. As shown, the WD errors are also Gaussian with a small mean (less than 1 degree) and STD  $\sim 30$  degrees. This is somewhat higher than the science requirement of the standard scatterometer missions ( $< 20$  degrees) [54]. However, the error statistics follow a similar trend with WS in that the mean RMS error decreases as increasing WS, as shown in the leftmost panels of the figure. For  $\text{WS} < 4$  m/s, the error is constantly highest ( $\sim 35$  degrees). This is true and the results are similar for all standard scatterometers and polarimetric radiometers for the low WS range. Then the error rapidly reduces with increasing WS, and it reduces to  $< 25$  degrees for  $\text{WS} > 10$  m/s, then it slowly reduces with WS for higher WS. However, for  $\text{WS} > 15$  m/s, the number of points reduces significantly, and the numerical weather model underestimates the WS for that range. This poses challenges in both for developing GMFs and for validation, as evidenced by the rightmost top panel, where it is seen that the WD RMS error (RMSE) increases for  $\text{WS} > 17$  m/s, while it is still either decreasing or constant in comparison with ASCAT as shown in the bottom panel of the same Fig.

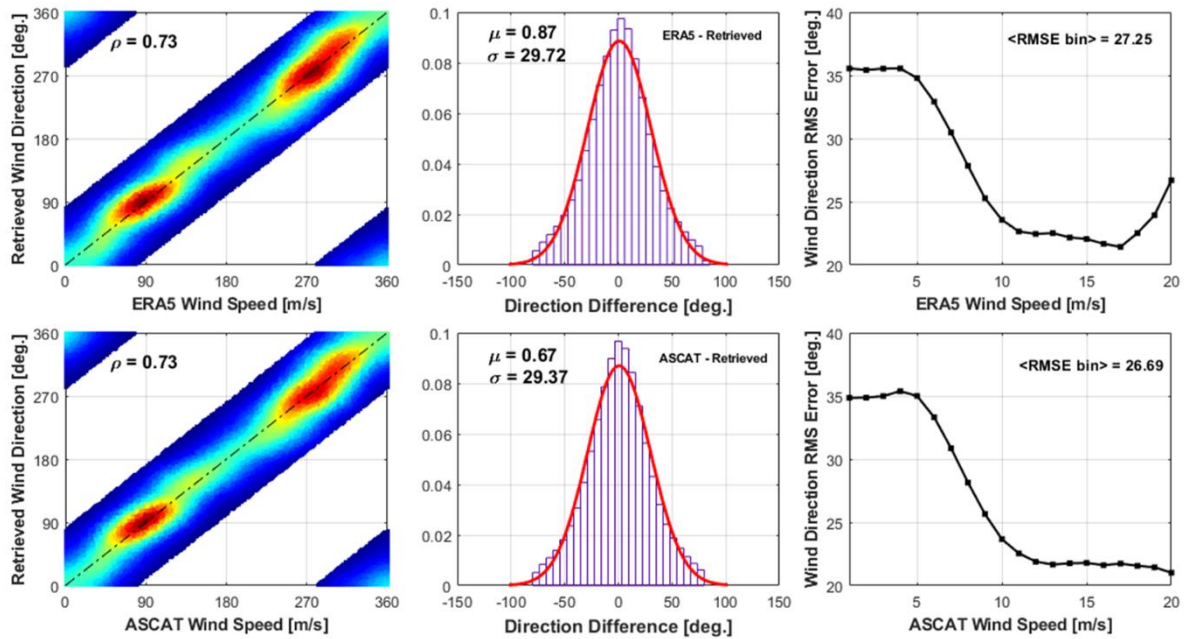


Figure 6.4: Wind direction retrieval performance

Now, Fig. 6.5 compares the WD retrieval performance of different spectral combinations, namely, the Ku-band PR and 10 GHz AV-H (1<sup>st</sup> column); the Ku-band PR and 10 GHz and 19 GHz AV-H (2<sup>nd</sup> column), the Ku- and Ka-band PR and 10 GHz and 19 GHz AV-H (3<sup>rd</sup> column), and the Ku- and Ka-band PR and 10 GHz, 19 GHz and 37 GHz AV-H (4<sup>th</sup> column). The results are presented in the same way as the previous Figures, but top-to-bottom, such that the top panels show the scatter diagram between the closest retrieved WD and ASCAT WD, the middle panels (row 2) present the histogram of the differences, and the bottom panels present the RMSE as a function of ASCAT WS. As shown, all the active and passive spectral combinations provide almost similar results, with the 3<sup>rd</sup> combination, which combines the Ku- and Ka-band PR and 10 GHz and 19 GHz AV-H, giving the best results. The benefit of including the Ka-band is apparent, especially, it improves the retrieval performance for low to mid WS range. However, there seems to be no additional benefit in adding the 37 GHz channel for WD retrieval.

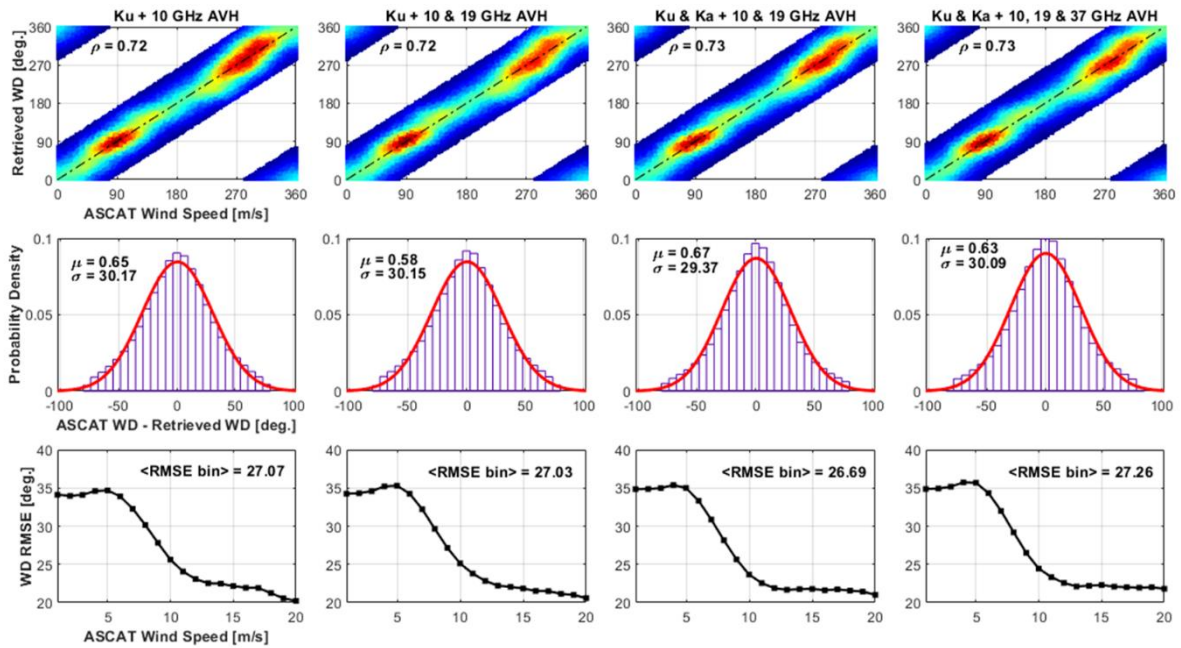


Figure 6.5: Wind direction retrieval performance comparison: (1<sup>st</sup> column) the left most is the combination of Ku-band PR and 10 GHz AV-H, (2<sup>nd</sup> column) the next is the same except it adds the 19 GHz AV-H; (3<sup>rd</sup> column) the following one adds Ka-band with the previous one, and finally, (4<sup>th</sup> column) the rightmost on the bottom panel, shows the combination of MLEs from Ku- and Ka-band, and 10,19, and 37 GHz AV-H.

Figure 6.6 compares the wind direction retrieval performance with SST-dependent DPR GMFs to the SST-independent counterparts. As expected, the consideration of SST as a separate GMF parameter provides superior results.

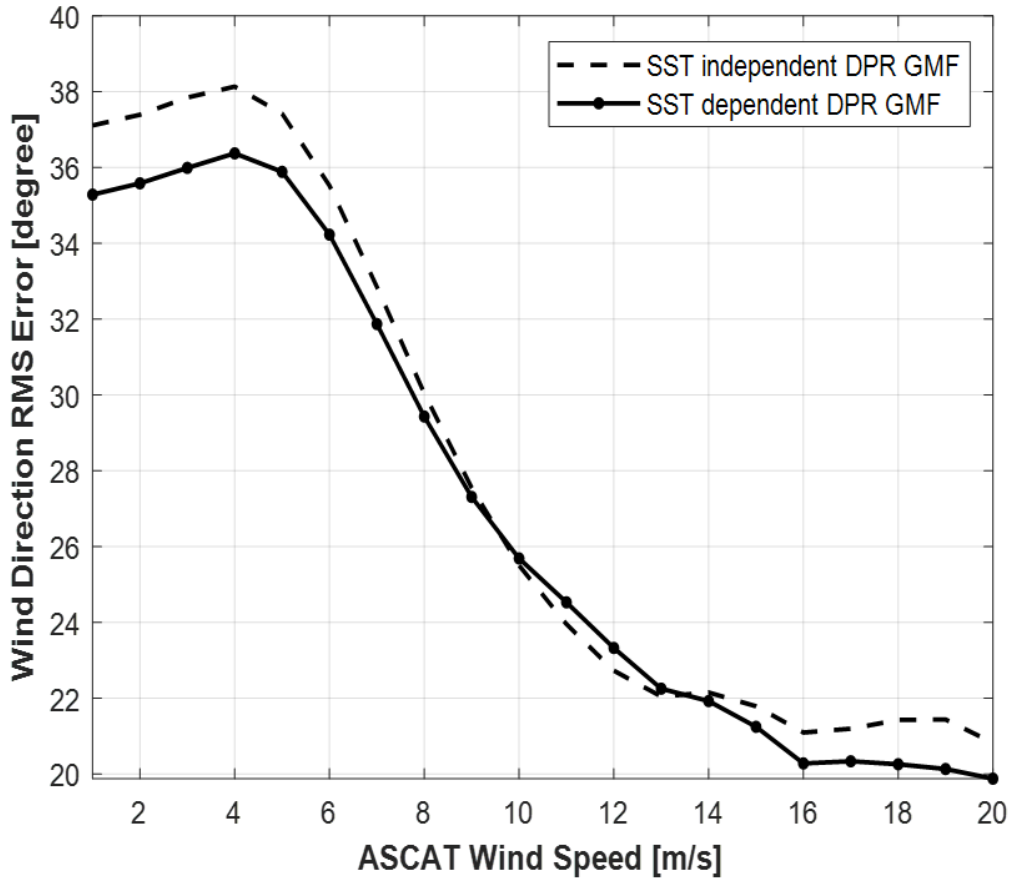


Figure 6.6: SST impact on OVW retrieval.

#### 6.2.4: Retrieval Skill

Finally, the retrieval skill, which is a measure of instrument noise, and is defined as[73],

$$\text{Skill} = \frac{\text{No of first ranked solutions are true solutions}}{\text{Total no of retrievals}} \quad (6.1)$$

For this study, the skills were calculated for the closest solutions. Figure 6.7 presents the ambiguity distributions and their percentage of being the closest solution (skills) in the order of their ranks. The top panel of Fig. 6.7 shows the number of ambiguities (probable solutions) in each retrieval in a set of around 0.87 million retrievals for the validation (2021 data set with 25 km resolutions after all filtering and quality control). As shown, 96% of WVCs in the validation dataset have two



solutions, 70% have three solutions, and 25% have four solutions. The maximum number of solutions was set to 4, although a small percentage of WVCs had more than four solutions with low probability. The bottom panel of the same figure shows the percentage of times the ambiguities were the closest solution. The 1<sup>st</sup> rank solutions were the closest solution for 45% of total retrievals. Therefore, the skill of the algorithm is 45%. The 2<sup>nd</sup> rank solutions were the closest solutions for 30% of the times, the 3<sup>rd</sup> rank was 21% times, and the 4<sup>th</sup> rank was only 5% times. Therefore, the ambiguities beyond the 4<sup>th</sup> rank were not significant. The threshold number of ambiguities thus misses only around 4% of true solutions.

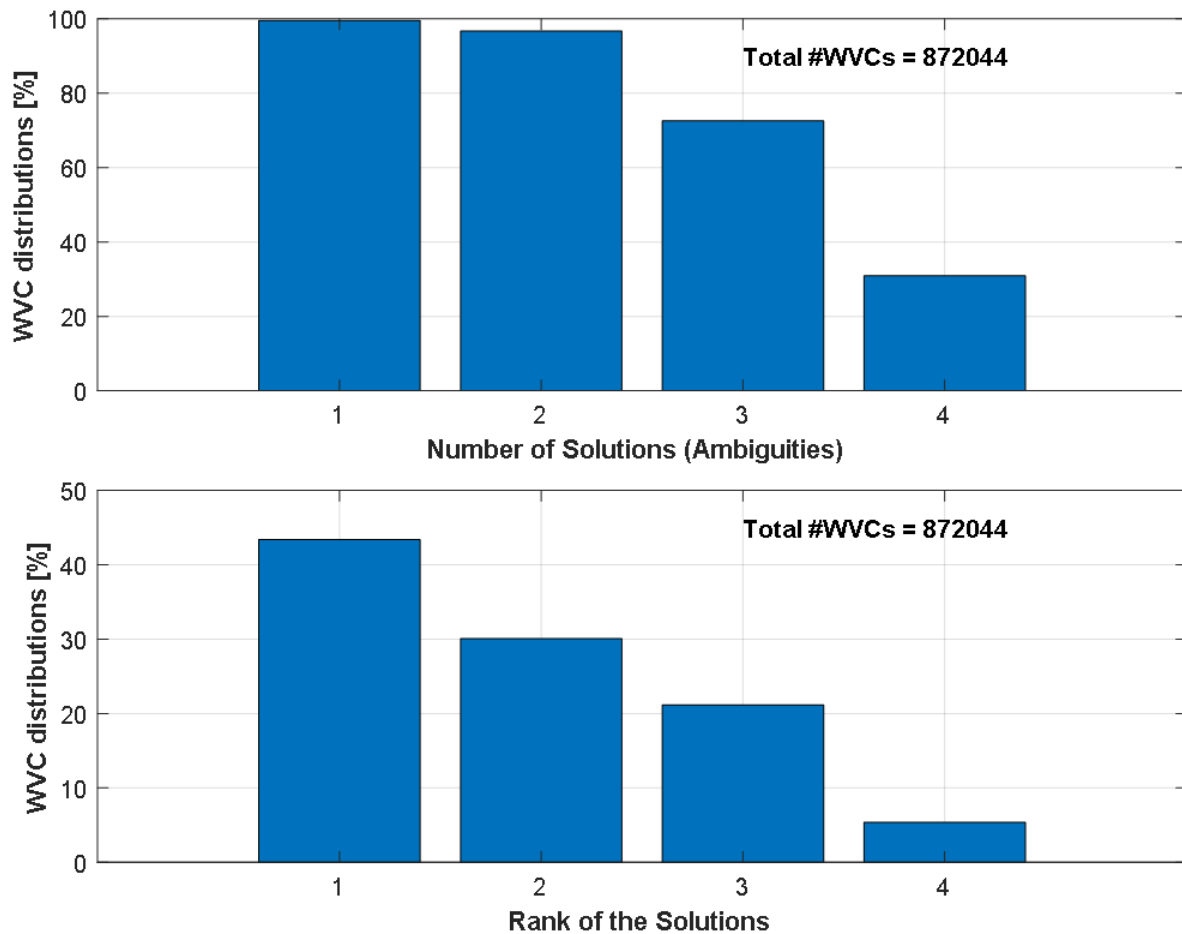


Figure 6.7: Retrieval skill and ambiguities

As expected, the skill also is a function of wind speed. This is depicted in Fig. 6.8. For a  $WS > 10$  m/s, the skill is greater than 50%, increasing with WS following the WD retrieval performance.

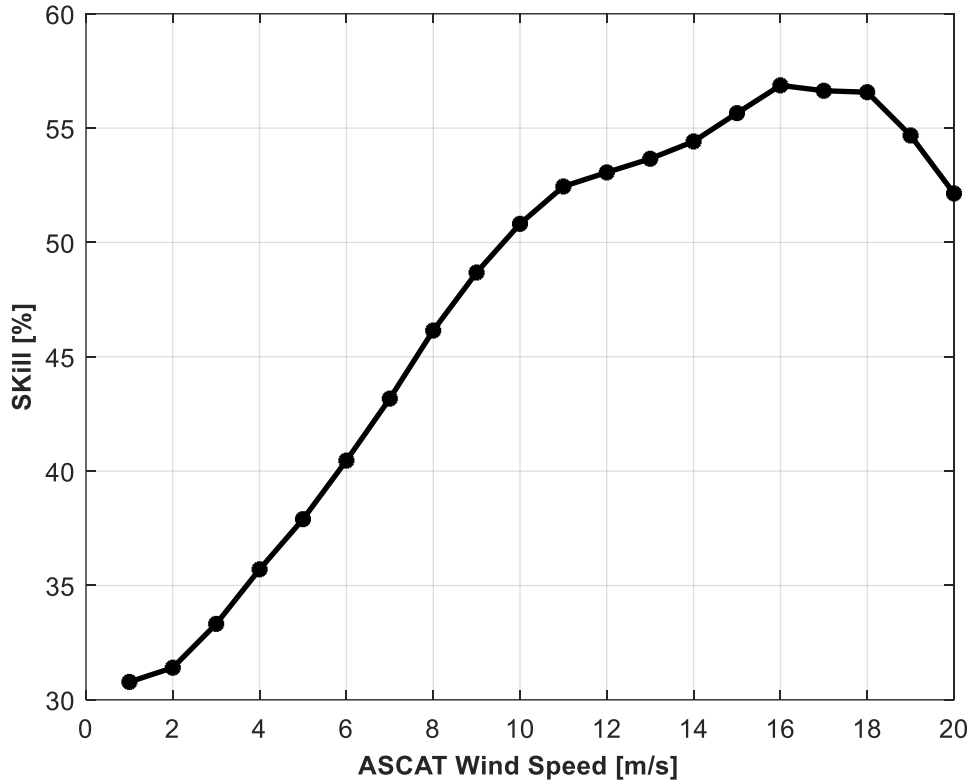


Figure 6.8: Retrieval skill vs wind speed

### 6.3: Discussion

The DPR/AVH OVW retrieval results were evaluated using 1 year of independent collocated OVW NWP and remotely sensed data. It is important to note that these independent OVW "surface truth" results were not used to tune the DPR nor GMI GMF's. A statistical analysis of the match-up dataset showed that the wind speed retrieval uncertainty is around 1 m/s with a

very small bias on the order of 0.2 m/s. For the wind direction, the Ku and Ka PR plus 10 and 19 GHz AV-H provides the best results with the overall mean RMSE ~27 degrees with either of ASCAT and ERA5, again with near 0 mean Gaussian error. Inclusion of 36 GHz AV-H did not apparently provide any additional benefit. Although, the WS retrieval performance satisfactorily meets the science requirements, the WD retrieval error is somewhat higher than the science requirements of WD retrieval ( $< 20$  degrees) for a standard scatterometer instrument. However, the trends of RMSE with WS are very similar to the standard scatterometers and polarimetric radiometer wind retrievals. Considering the diurnal capability and possibility of uninterrupted long-term data, these results are promising. Moreover, there are still rooms for improvement in the retrieval algorithm, which will be discussed in Chapter 7.

## CHAPTER 7: CONCLUSION AND FUTURE WORK

This chapter provides a summary of the dissertation, discuss the significance and limitations of the work, and suggest potential areas for future research and improvement.

### 7.1: Summary

In this dissertation, we investigated the feasibility of ocean vector wind (OVW) measurement from the GPM core observatory using a combined active and passive algorithm. For this, we first broadly analyzed the ocean surface backscatter characteristics of GPM DPR as function of WS, RWD, SST, and EIA over the range of nadir through  $\pm 18^\circ$ . This range of incidence angles has not been used for OVW purpose for any radar bands as it has not been considered optimal. But we demonstrated that both Ku- and Ka-band radars have a statistically significant OVW signature across most of the swath over the EIA range. This analysis resulted the active geophysical model functions at Ku- and Ka-band. To the best of our knowledge, it is the first-time use of a space-borne Ka-band radar for OVW measurement (scatterometry) purpose. As demonstrated, the trends of anisotropic roughness response of the Ka-band radar are similar to Ku-band, but it has some distinct characteristics, such as higher directional sensitivity for low to medium WS range. The Ka-band is also more sensitive to the impacts of wave breaking and change of surface tension and viscosity due to change of surface temperature. Besides OVW measurement, these results have important implications for other oceanographic applications including precipitation measurement, surface topography applications.

Then we characterized the vector wind characteristics of linearly polarized (V and H pol) passive microwave brightness temperature ( $T_B$ ) from three lower frequency channels (10, 19, and 37 GHz) of GMI. Although, the  $T_B$ s have non-negligible WD dependency, the WD retrieval from

passive linearly polarized  $T_B$ s has not been possible. Because the WD signals are weak and easily obscured by atmospheric WV and CLW. So, we leveraged an atmospheric clearing algorithm that uses a linear combination of  $T_B$ s to suppress the atmospheric signal and enhance the WD signals. The WD signature then becomes statistically substantial and robust for vector wind retrieval. We utilized different spectral combination to find the optimum active and passive spectral combination for the best OVW retrieval.

A MLE based combined active, and passive (CAP) OVW retrieval algorithm was developed that minimizes the distance between the GMF and observations and normalizes by the known variance. The active and passive cost functions are further normalized by their maximum to make it uniform for active and passive. The minimum for each WS forms the 1D cost function for WD retrieval. The relative prominences of the cost function provided the possible WD solutions. There have been one to four solutions for 96% of WVCs in the validation dataset. The other had more than four solutions. The nature of the ambiguities was assessed in detail. Although the DPR and GMI jointly have two azimuths looks for any WVC in the retrieval, the structure and distribution of ambiguities are very similar to that of the conventional scatterometers. This is one of the very important leads of the proposed algorithm.

For the validation, one year of collocated near-simultaneous winds from ASCAT-B and ERA5 reanalysis were used as surface truth reference. The closest solution to the reference was compared for the performance evaluation. The GMI derived WS error showed a near-zero mean Gaussian distribution with an STD of <1 m/s. The CAP derived WS error were also Gaussian but pointed higher STD (~ 1.5 m/s). This is because GPM DPR operates across and critical transition EIA range at the middle that provides poor WS sensitivity. The WD retrieval error are also near

zero-mean Gaussian with mean RMSE of around  $27^\circ$  with both ASCAT and ERA5 WD. The RMSE for lower WS range is higher, but it reduces with increasing WS. For example, it becomes  $\leq 22^\circ$  for  $WS \geq 10$  m/s. The science requirements for specialized OVW instruments are  $WS \text{ STD} < 2$  m/s and  $WD \text{ RMSE} < 20^\circ$ . So, although the WS retrieval results meet the requirements well, the current WD retrieval error is higher than the requirement.

The performance of different spectral combinations of active and passive frequency channels were evaluated. The spectral combinations of active Ku and Ka-band with passive frequency channels of 10 and 19 GHz provided the best results. The inclusion of Ka-band improves the retrieval performance for lower to middle WS range. However, the passive 37 GHz frequency channel was not found to provide any additional benefit. The impact of SST on retrieval was assessed. For this, two versions of GMF were derived – one with SST as independent dimension, and the other by averaging over SST. The former provided the better results. The retrieval skill of the algorithm was found to be  $\sim 45\%$ . However, it also increases with WS and becomes  $\geq 50\%$  for  $WS \geq 10$  m/s.

Although, there are room for improvements (some of which are indicated below), the results are promising, and the scientific value of the results are high. This offers the potential to provide a long-term OVW data, which will include a unique monthly diurnal OVW s statistic. The scientific significance of this accomplishment lies in the fact that the non-sun-synchronous orbit of GPM allows the diurnal pattern of OVWs to be measured, which rarely occurs in satellite remote sensing of ocean surface winds. Furthermore, this ocean wind measurement capability can be extended to the TRMM to create a multidecadal climate data record for Earth science research.

TRMM achieved a lifetime of >17 years, which makes it a valuable dataset for studying climate change in the tropics.

## 7.2: Significance of the Study

Satellite missions are complex and expensive undertakings that require significant planning, preparation, and huge investment. The process of planning to having an operational satellite takes years that involve many different stakeholders. GPM mission has been one of the greatest endeavors in remote sensing history, and it successfully demonstrated its significance for precipitation measurement. We attempted to extend this effort to estimate another important climate variable, the vector winds, as a byproduct, utilizing the same measurements without any technical modification, or any extra cost. The algorithm and the model functions developed in this dissertation are readily applicable to the entire GPM-TRMM, and other similar instruments in future, with minor calibration modification, to produce an uninterrupted multidecade OVW data products (1997 to ongoing) for weather and climate studies, to assess the climate change impacts. Furthermore, due to the unique benefit of GPM (and TRMM) non-Sun synchronous orbit, a full diurnal sampling of the ocean surface is possible within a 2-month period, which will allow resolving the diurnal and semidiurnal variabilities of ocean surface vector winds in the tropical ocean. In addition, both the active and passive GMFs developed in this dissertation might be a great reference for characterizing surface response for pre- and post-launch instrument performance assessment and error characterization, etc.

### 7.3: Directions for Future Work

#### 7.3.1: More Appropriate Noise Model

An accurate knowledge of inherent measurement uncertainties of instruments is essential for OVW measurement and quality control [142]. Thus, for every scatterometer, relevant noise model was developed [56], [131]. Unfortunately, the DPR instruments do not have any known noise model so far that could be applied to normalize the uncertainty. Although we have knowledge about the NEDT of individual GMI channel, the effective noise mode for A is yet to be developed. This poses a significant problem in current CAP retrieval algorithm, because without an accurate estimate of instrument noise, the cost function cannot be properly normalized. As a result, it was seen that sometimes either active or the passive part of the algorithm dominated each other in the CAP algorithm. This decreased the retrieval skill and accuracy. So, a proper instrument as well as geophysical noise model for DPR and AVH channels might improve the retrieval skill and performance.

#### 7.3.2: An Objective Ambiguity Removal

The results presented represent the performance of the closest solution to reference (ERA5/ASCAT) wind direction, which is a measure of the actual performance. However, to develop the actual OVW data product, a more objective AR method needs to be used. Considering the nature of the MLE cost function and ambiguity structure, we recommend 2DVAR AR technique, as described in Section 5.3, would be appropriate for this.

#### 7.3.3: Secondary Effects

Besides the primary factors, i.e., WS, WD, EIA, and SST, that formed the GMFs, there are some key secondary factors that impact the  $\sigma^0$  and  $T_B$  vector wind signals and, thereby, the



retrieval accuracy (see [35]). These include factors such as significant ocean wave height (SWH), sea surface currents, confused sea-states, atmospheric stability, surface film, and rain etc. Although a proper geophysical noise model may take some of these into account, some key factors may still need to be considered explicitly. Larger waves have a significant impact in near nadir backscatter. So, as reported by some studies [98]–[100], one concern is the effect of SWH and ocean swell, which could be significant at this near nadir EIA range. Dual-frequency observations and collocated ocean wave numerical model forecasts should allow correction for these long ocean wave contributions [143]. Therefore, a future extension of this study to include ocean sea state, particularly the SWH effects on ocean normalized cross section at both Ku- and Ka-bands for lower EIAs.

#### 7.3.4: Other Potential Improvements

Following could be possible direction of future research to extend and enhance the studies of this dissertation.

##### 7.3.4.1: *Higher Spatial Resolution*

The results we presented in this dissertation was produced for a horizontal resolution of 25 km (0.25°). High resolution data products are critical user demand for various applications, such as coastal remote sensing where various commercial including rescue operation takes place. The DPR original horizontal resolution is around 5 km. So, an attempt might be taken to retrieve OVW with DPR original footprint resolution.

##### 7.3.4.2: *Ocean vector wind retrieval under rain*

This dissertation focused OVW retrieval under clear sky condition. With increasing rain-rate the underlying assumption for A parameter will not hold well, so the performance might degrade.

Some recent studies [126], [127] developed all-weather wind speed only retrieval algorithm using spectral combination of passive brightness temperature. Similar approach might be followed to extend the algorithm to make it applicable for all-weather conditions. Rain correction might be applied using DPR differential absorption characteristics.

## **APPENDIX A: NEUTRAL STABILITY WINDS**

Since the wind forcing, which creates the capillary waves superimposed on the large gravity waves, occurs at the ocean surface, the wind friction velocity ( $U^*$ ) is more appropriate metric to compare with the radar backscatter. However, in the natural ocean environment, this wind friction velocity measurement is not feasible. Therefore, the usual practice is to use a wind meter (anemometer) located on a buoy or boat at some height above the surface. Simultaneously sea surface temperature and the air temperature are measured to determine the atmospheric stability. The atmospheric profile of surface winds (wind speed versus height) can be reliably calculated by fluid mechanics and used to extrapolate anemometer measurement to the surface to derive  $U^*$ .

For a given air friction velocity at surface there can be many profiles of wind speed versus height, depending upon atmospheric stability (air/sea temperature gradient). The anemometer measurement at 20 m height is equivalent to 12.2 m/s for a stable atmosphere, for an example, as shown in Fig. A.1. This measurement is translated to the surface to produce a  $U^* = 5.4$  m/s. Next, if this  $U^*$  is moved to a reference height = 10 m along the neutral profile, the neutral stability wind speed becomes 10.1 m/s as depicted in the Fig.

Thus, the neutral stability winds at 10 m height have become the standard “surface truth” for comparison with remote sensing of ocean wind measurements. Under neutral stability conditions and a given  $U^*$  value, it is the wind speed that would have been measured by an anemometer. Thus, this normalization procedure effectively produces the corresponding  $U^*$ , which is instantaneously in equilibrium with the ocean capillary waves that produce the radar backscatter. In other words, the ocean so is highly correlated to  $U^*$  and the neutral stability wind speed.

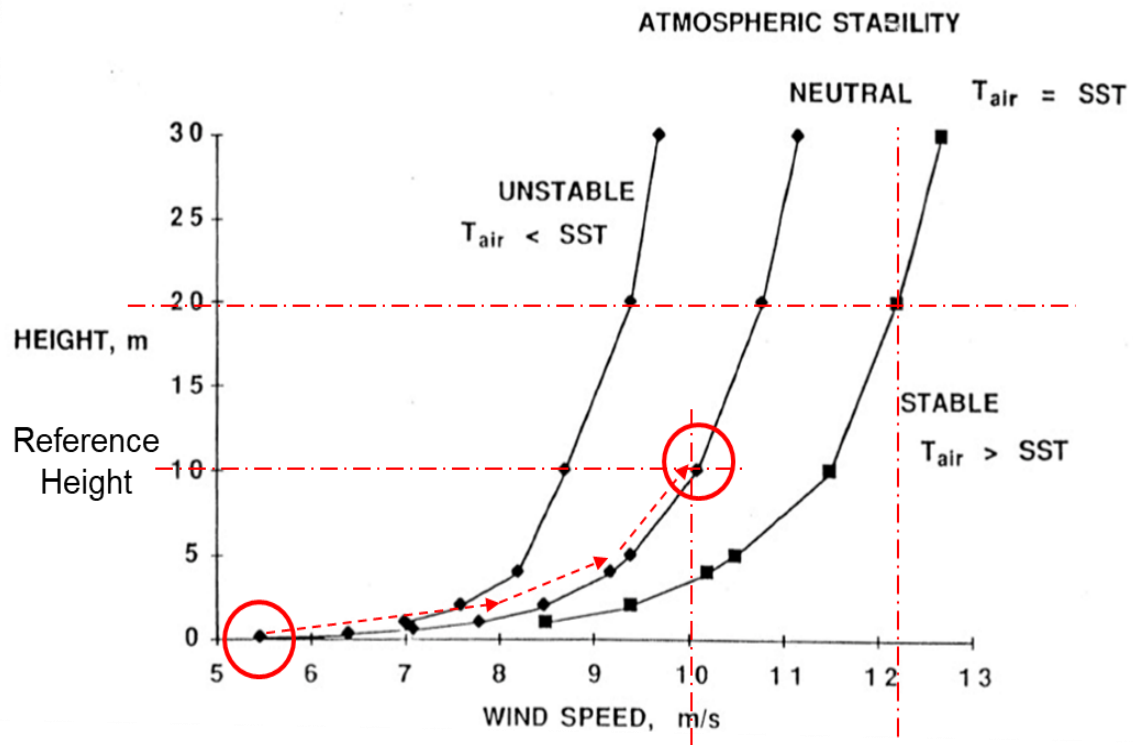


Figure A.1: Neutral stability wind profiles [Courtesy: Dr. W. Linwood Jones]

## **APPENDIX B: COPYRIGHT PERMISSION LETTERS**

**Re: GPM Contact Form: For permission to use the figure of GPM Core Observatory Satellite**

Reed, Jacob B. (GSFC-617.0)[TELOPHASE CORP] <jacob.reed@nasa.gov>

Sun 12/11/2022 10:15 AM

To: Alamgir Hossan <ah@Knights.ucf.edu>; Portier, Andrea M. (GSFC-612.0)[SCIENCE SYSTEMS AND APPLICATIONS INC] <andrea.m.portier@nasa.gov>; Huffman, George J. (GSFC-6120) <george.j.huffman@nasa.gov>; jason.west@mail.pps.eosdis.nasa.gov <jason.west@mail.pps.eosdis.nasa.gov>; owen.kelley@mail.pps.eosdis.nasa.gov <owen.kelley@mail.pps.eosdis.nasa.gov>

Hi Alagmir,

Yes, you may use this image. You can use the following credits:

*Credits: NASA Global Precipitation Measurement Mission*

Here is our full media usage policy for your records:

<https://www.nasa.gov/multimedia/guidelines/index.html>

Thanks,



**Jacob Reed**  
Digital Outreach Lead  
NASA Goddard Space Flight Center

[jacob.reed@nasa.gov](mailto:jacob.reed@nasa.gov)  
301.639.2484



[appliedsciences.nasa.gov](http://appliedsciences.nasa.gov)  
[gpm.nasa.gov](http://gpm.nasa.gov)

[Telophase Corp.](http://Telophase Corp.)

## REFERENCES

- [1] M. A. Bourassa *et al.*, “Remotely sensed winds and wind stresses for marine forecasting and ocean modeling,” *Front. Mar. Sci.*, vol. 6, p. 443, 2019.
- [2] A. B. V. Bôas *et al.*, “Integrated Observations of Global Surface Winds , Currents , and Waves : Requirements and Challenges for the Next Decade,” *Front. Mar. Sci.*, vol. 6, no. July, pp. 1–34, 2019.
- [3] A. Stoffelen, R. Kumar, J. Zou, V. Karaev, P. S. Chang, and E. Rodriguez, “Ocean surface vector wind observations,” *Remote Sens. Asian Seas*, pp. 429–447, 2018.
- [4] NASA Research Announcement, "Research Opportunities in Space and Earth Science (ROSES-2022)," [Online]. Available: <https://solicitation.nasaprs.com/ROSES2022>. [Accessed: Mar. 15, 2022].
- [5] L. Ricciardulli and A. Manaster, “Intercalibration of ASCAT scatterometer winds from MetOp-A,-B, and-C, for a stable climate data record,” *Remote Sens.*, vol. 13, no. 18, 2021.
- [6] World Meteorological Organization, “Systematic Observation Requirements for Satellite-based Products for Climate - GCOS-107 (WMO/TD No. 1338),” vol. 107, no. 1338, p. 103, 2006.
- [7] S.L. Durden and D. Perkovic-Martin, "The RapidScat ocean winds scatterometer: A radar system engineering perspective," *IEEE Geoscience and Remote Sensing Magazine*, vol. 5, no. 3, pp. 36-43, Sep. 2017.
- [8] C. Deser and C. A. Smith, “Diurnal and Semidiurnal Variations of the Surface Wind Field over the Tropical Pacific Ocean,” *J. Clim.*, vol. 11, no. 7, pp. 1730–1748, 1998.
- [9] A. Dai and C. Deser, “Diurnal and semidiurnal variations in global surface wind and divergence fields,” *J. Geophys. Res. Atmos.*, vol. 104, no. D24, pp. 31109–31125, 1999.
- [10] R. Ueyama and C. Deser, “A climatology of diurnal and semidiurnal surface wind variations over the tropical Pacific Ocean based on the Tropical Atmosphere Ocean moored buoy array,” *J. Clim.*, vol. 21, no. 4, pp. 593–607, 2008.



- [11] F.J. Turk, S. Hristova-Veleva, and D. Giglio, "Examination of the daily cycle wind vector modes of variability from the constellation of microwave scatterometers and radiometers," *Remote Sensing*, vol. 13, no. 1, pp. 141, Jan. 2021.
- [12] G. D. Giglio, *et al.*, "Annual Modulation of Diurnal Winds in the Tropical Oceans," *Remote Sensing*, vol. 14, no. 3, p. 459, Mar. 2022.
- [13] F. J. Wentz *et al.*, "Evaluating and Extending the Ocean Wind Climate Data Record," *IEEE J. Sel. Top. Appl. Earth Obs. Remote Sens.*, vol. 10, no. 5, pp. 2165–2185, 2017.
- [14] T. J. Lang, "Investigating the Seasonal and Diurnal Cycles of Ocean Vector Winds Near the Philippines Using RapidScat and CCMP," *J. Geophys. Res. Atmos.*, vol. 122, no. 18, pp. 9668–9684, 2017.
- [15] P. Garg, S. W. Nesbitt, T. J. Lang, and G. Priftis, "Diurnal cycle of tropical oceanic mesoscale cold pools," *J. Clim.*, vol. 34, no. 23, pp. 9305–9326, 2021.
- [16] A. C. Paget, D. G. Long, and N. M. Madsen, "RapidScat Diurnal Cycles over Land," *IEEE Trans. Geosci. Remote Sens.*, vol. 54, no. 6, pp. 3336–3344, 2016.
- [17] A. Y. Hou *et al.*, "The global precipitation measurement mission," *Bull. Am. Meteorol. Soc.*, vol. 95, no. 5, pp. 701–722, 2014.
- [18] G. Skofronick-Jackson *et al.*, "The global precipitation measurement (GPM) mission for science and Society," *Bull. Am. Meteorol. Soc.*, vol. 98, no. 8, pp. 1679–1695, 2017.
- [19] G. Skofronick-Jackson *et al.*, "The Global Precipitation Measurement (GPM) mission's scientific achievements and societal contributions: reviewing four years of advanced rain and snow observations," *Q. J. R. Meteorol. Soc.*, vol. 144, no. April, pp. 27–48, 2018.
- [20] C. Kummerow, W. Barnes, T. Kozu, J. Shiue, and J. Simpson, "The Tropical Rainfall Measuring Mission (TRMM) sensor package," *J. Atmos. Ocean. Technol.*, vol. 15, no. 3, pp. 809–817, 1998.
- [21] G. Skofronick-Jackson, "The Global Precipitation Measurement (GPM) Mission," *Int. Geosci. Remote Sens. Symp.*, pp. 3589–3592, 2020.

- [22] M. Portabella, A. Stoffelen, M. Belmonte, A. Verhoef, J. Verspeek, and J. Vogelzang, "ASCAT Scatterometer wind data processing," Instrumentation ViewPoint. *ESA Bull.*, vol. 102, pp. 19-27, 2000.
- [23] M. W. Spencer, "Improved resolution backscatter measurements with the SeaWinds pencil-beam scatterometer," *IEEE Trans. Geosci. Remote Sens.*, vol. 38, no. 1 I, pp. 89–104, 2000.
- [24] R. Yun *et al.*, "CFOSAT Rotating Fan-Beam Scatterometer Backscatter Measurement Processing," *Earth Sp. Sci.*, vol. 8, no. 11, pp. 1–18, 2021.
- [25] M. Panfilova and V. Karaev, "Gale Wind Speed Retrieval Algorithm Using Ku-Band Radar Data Onboard GPM Satellite," *Remote Sens.*, vol. 14, no. 24, 2022.
- [26] C. Jiang, L. Ren, J. Yang, Q. Xu, and J. Dai, "Wind Speed Retrieval Using Global Precipitation Measurement Dual-Frequency Precipitation Radar Ka-Band Data at Low Incidence Angles," *Remote Sens.*, vol. 14, no. 6, 2022.
- [27] F. J. Wentz, "Measurement of oceanic wind vector using satellite microwave radiometers," *IEEE Transactions on Geoscience and Remote Sensing*, vol. 30, no. 5. pp. 960–972, 1992.
- [28] T. Meissner and F. Wentz, "An Updated Analysis of the Ocean Surface Wind Direction Signal in Passive Microwave Brightness Temperatures," *IEEE Trans. Geosci. Remote Sens.*, vol. 40, no. 6, pp. 1230–1240, 2002.
- [29] S. Soisuvarn, Z. Jelenak and W. L. Jones, "An ocean surface wind vector model function for a Spaceborne Microwave Radiometer", *IEEE Trans. Geosci. Remote Sens.*, vol. 45, no. 10, pp. 3119-3130, 2007.
- [30] W. L. Jones, S. Soisuvarn, Jun Park, I. Adams, and T. Kasparis, "Combined active and passive microwave sensing of ocean surface wind vector from TRMM," *Ocean. '02 MTS/IEEE*, vol. 4, no. C, pp. 1981–1986, 2004.
- [31] S. Soisuvarn, W. L. Jones, and T. Kasparis, "Combined Active and Passive Microwave Sensing of Ocean Surface Wind Vector from TRMM," *Int. Geosci. Remote Sens. Symp.*, vol. 2, no. C, pp. 1257–1260, 2003.

- [32] S. Soisuvarn, W. L. Jones and T. Kasparis, "Validation of ocean surface wind vector sensing using combined active and passive microwave measurements," *IGARSS 2004. 2004 IEEE International Geoscience and Remote Sensing Symposium*, Anchorage, AK, USA, 2004, pp. 50, doi: 10.1109/IGARSS.2004.1368941.
- [33] S. O. Alswiss, P. Laupattarakasem, and W. L. Jones, "A novel Ku-band radiometer/scatterometer approach for improved oceanic wind vector measurements," *IEEE Trans. Geosci. Remote Sens.*, vol. 49, no. 9, pp. 3189–3197, 2011.
- [34] W. L. J. Moore, Richard K., "Satellite Scatterometer Wind Vector Measurements - the Legacy of the Seasat Satellite Scatterometer," no. December, *IEEE Geosci. Remote Sens. Newsletter*, pp. 18-32, 2004.
- [35] W. T. Liu and X. Xie, "Measuring ocean surface wind from space," *Remote Sens. Mar. Environ. Man. Remote Sens.*, pp. 149–178, 2006.
- [36] W. L. Jones, "Early Days of Microwave Scatterometry : RadScat to SASS," *IEEE Int. Geosci. Remote Sens. Symp. 2015*, pp. 4208–4211, 2015.
- [37] J. W. Jones, *et al.*, "The SEASAT-A satellite scatterometer: The geophysical evaluation of remotely sensed wind vectors over the ocean," *Journal of Geophysical Research: Oceans*, vol. 87, no. C5, pp. 3297-3317, Apr. 1982.
- [38] P. W. Gaiser *et al.*, "The windSat spaceborne polarimetric microwave radiometer: Sensor description and early orbit performance," *IEEE Trans. Geosci. Remote Sens.*, vol. 42, no. 11, pp. 2347–2361, 2004.
- [39] P. W. Gaiser, M. H. Bettenhausen, L. Li, and E. M. Twarog, "The WindSat polarimetric radiometer and ocean wind measurements," *Proc. MTS/IEEE Ocean. 2005*, vol. 2005, pp. 1043–1045, 2005.
- [40] Z. Jiang, Y. Li, F. Yu, G. Chen, and W. Yu, "A damped newton variational inversion method for SAR wind retrieval," *J. Geophys. Res.*, vol. 122, no. 2, pp. 823–845, 2017.
- [41] D. Entekhabi *et al.*, "The soil moisture active passive (SMAP) mission," *Proc. IEEE*, vol. 98, no. 5, pp. 704–716, 2010.

- [42] A. G. Fore, S. H. Yueh, W. Tang, B. W. Stiles, and A. K. Hayashi, "Combined Active/Passive Retrievals of Ocean Vector Wind and Sea Surface Salinity With SMAP," *IEEE Trans. Geosci. Remote Sens.*, vol. 54, no. 12, pp. 7396–7404, 2016.
- [43] S. H. Yueh *et al.*, "L-band passive and active microwave geophysical model functions of ocean surface winds and applications to Aquarius retrieval," *IEEE Trans. Geosci. Remote Sens.*, vol. 51, no. 9, pp. 4619–4632, 2013.
- [44] S. H. Yueh, S. J. Dinardo, A. G. Fore, and F. K. Li, "Passive and active L-band microwave observations and modeling of ocean surface winds," *IEEE Trans. Geosci. Remote Sens.*, vol. 48, no. 8, pp. 3087–3100, 2010.
- [45] Stoffelen, Adrianus Cornelis Maria. "Scatterometry." PhD diss., 1996.
- [46] P. A. Marcos, "Wind Field Retrieval from Satellite Radar Systems," Doctoral Thesis, Universitat de Barcelona, 2002.
- [47] F. Ulaby and D. Long, "Microwave Radar and Radiometric Remote Sensing," *Microw. Radar Radiom. Remote Sens.*, no. 2015, 2014.
- [48] M. Gade and A. Stoffelen, "An introduction to microwave remote sensing of the asian seas," *Remote Sens. Asian Seas*, pp. 3–38, 2018.
- [49] M. H. Freilich and B. A. Vanhoff, "The relationship between winds, surface roughness, and radar backscatter at low incidence angles from TRMM precipitation radar measurements," *J. Atmos. Ocean. Technol.*, vol. 20, no. 4, pp. 549–562, 2003.
- [50] V. Y. Karaev, Y. A. Titchenko, E. A. Meshkov, and M. A. Panfilova, "Microwave backscattering by the sea surface in the transition range of incidence angles (10°-20°): Theory and experiment," *Prog. Electromagn. Res. Symp.*, vol. 2017-Novem, pp. 2183–2188, 2017.
- [51] V. Y. Karaev, M. A. Panfilova, M. S. Ryabkova, Y. A. Titchenko, and E. M. Meshkov, "Doppler spectrum of microwave signal backscattered by sea surface at small incidence angles: Experiment," *Sovrem. Probl. Distantionnogo Zo. Zemli iz Kosmosa*, vol. 17, no. 2, pp. 149–161, 2020.

- [52] W. T. Liu and W. Tang, *Equivalent Neutral Wind*, USA, CA, Pasadena: *JPL Publ. Lab.*, pp. 17-96, 1996.
- [53] M. A. Bourassa and P. J. Hughes, "Surface heat fluxes and wind remote sensing," in *New Frontiers in Operational Oceanography*, Ed. by E. Buch, Springer, 2018, pp. 245-270.
- [54] D. E. Weissman *et al.*, "Challenges to satellite sensors of ocean winds: Addressing precipitation effects," *J. Atmos. Ocean. Technol.*, vol. 29, no. 3, pp. 356–374, 2012.
- [55] F. M. Naderi, M. H. Freilich, and D. G. Long, "Spaceborne Radar Measurement of Wind Velocity Over the Ocean—An Overview of the NSCAT Scatterometer System," *Proc. IEEE*, vol. 79, no. 6, pp. 850–866, 1991.
- [56] M. W. Spencer, C. Wu, and D. G. Long, "Tradeoffs in the design of a spaceborne scanning pencil beam scatterometer: application to seawinds," *IEEE Trans. Geosci. Remote Sens.*, vol. 35, no. 1, pp. 115–126, 1997.
- [57] A. Stoffelen, "RapidScat on the International Space Station ISS," [Online]. Available: [https://www-cdn.eumetsat.int/files/2020-04/pdf\\_tl\\_15\\_09\\_16\\_b.pdf](https://www-cdn.eumetsat.int/files/2020-04/pdf_tl_15_09_16_b.pdf)
- [58] K. Zhao and C. Zhao, "Evaluation of HY-2A scatterometer ocean surface wind data during 2012-2018," *Remote Sens.*, vol. 11, no. 24, 2019.
- [59] X. Li, W. Lin, B. Liu, Z. Wang, B. Zhang, and Y. He, "Sea Surface Wind Retrieval Using the Combined Scatterometer and Altimeter Backscatter Measurements of the HY-2B Satellite," *IEEE Trans. Geosci. Remote Sens.*, pp. 1–12, 2021.
- [60] W. Tang, W. T. Liu, B. Stiles, and A. Fore, "Detection of diurnal cycle of ocean surface wind from space-based observations," *Int. J. Remote Sens.*, vol. 35, no. 14, pp. 5328–5341, 2014.
- [61] J. Vogelzang and A. Stoffelen, "Improvements in Ku-band scatterometer wind ambiguity removal using ASCAT-based empirical background error correlations," *Q. J. R. Meteorol. Soc.*, vol. 144, no. 716, pp. 2245–2259, 2018.

- [62] L. Ren *et al.*, "Ocean Surface Wind Speed Dependence and Retrieval From Off-Nadir CFOSAT SWIM Data," *Earth Sp. Sci.*, vol. 8, no. 6, pp. 1–15, 2021.
- [63] D. Hauser *et al.*, "Satellite remote sensing of surface winds, waves, and currents: where are we now?," *Surveys in Geophysics*, vol. 44, no. 1, pp. 1-90, 2023.
- [64] A. Stoffelen and M. Portabella, "On bayesian scatterometer wind inversion," *IEEE Trans. Geosci. Remote Sens.*, vol. 44, no. 6, pp. 1523–1533, 2006.
- [65] B. W. Stiles, B. D. Pollard, and R. S. Dunbar, "Direction interval retrieval with thresholded nudging: A method for improving the accuracy of QuikSCAT winds," *IEEE Trans. Geosci. Remote Sens.*, vol. 40, no. 1, pp. 79–89, 2002.
- [66] B. S. Gohil, P. Sharma, R. Sikhakolli, and A. Sarkar, "Directional stability and conservation of scattering (DiSCS)-based directional-ambiguity removal algorithm for improving wind fields from scatterometer: A quikSCAT example," *IEEE Geosci. Remote Sens. Lett.*, vol. 7, no. 3, pp. 592–595, 2010.
- [67] T. Meissner and F. J. Wentz, "The Emissivity of the Ocean Surface Between 6 and 90 GHz Over a Large Range of Wind Speeds and Earth Incidence Angles," *IEEE Trans. Geosci. Remote Sens.*, vol. 50, no. 8, pp. 3004–3026, 2012.
- [68] S. Brown *et al.*, "The compact ocean wind vector radiometer: A new class of low-cost conically scanning satellite microwave radiometer system," in *Proc. IEEE Geosci. Remote Sens. Soc. (IGRSS)*, 35th Can. Remote Sens. Soc. (CSRS), 2014.
- [69] S. H. Yueh, "Modeling of wind direction signals in polarimetric sea surface brightness temperatures," *IEEE Trans. Geosci. Remote Sens.*, vol. 35, no. 6, pp. 1400–1418, 1997.
- [70] S. H. Yueh, R. Kwok, and S. V. Nghiem, "Polarimetric scattering and emission properties of targets with reflection symmetry," *Radio Sci.*, vol. 29, no. 6, pp. 1409–1420, 1994.
- [71] S. H. Yueh, W. J. Wilson, F. K. Li, S. V. Nghiem, and W. B. Ricketts, "Polarimetric Measurements of Sea Surface Brightness Temperatures Using an Aircraft K-Band Radiometer," *IEEE Trans. Geosci. Remote Sens.*, vol. 33, no. 1, pp. 85–92, 1995.

- [72] S. H. Yueh, W. J. Wilson, S. J. Dinardo, and F. K. Li, "Polarimetric microwave brightness signatures of ocean wind directions," *IEEE Trans. Geosci. Remote Sens.*, vol. 37, no. 2 II, pp. 949–959, 1999.
- [73] M. H. Bettenhausen, C. K. Smith, R. M. Bevilacqua, N. Y. Wang, P. W. Gaiser, and S. Cox, "A nonlinear optimization algorithm for windSat wind vector retrievals," *IEEE Trans. Geosci. Remote Sens.*, vol. 44, no. 3, pp. 597–610, 2006.
- [74] C. K. Smith, M. Bettenhausen, and P. W. Gaiser, "A statistical approach to WindSat ocean surface wind vector retrieval," *IEEE Geosci. Remote Sens. Lett.*, vol. 3, no. 1, pp. 164–168, 2006.
- [75] T. Meissner and F. Wentz, "Ocean retrievals for WindSat radiative transfer model, algorithm, validation," *Proc. MTS/IEEE Ocean. 2005*, vol. 2005, no. February 2005, 2005.
- [76] S. H. Yueh and J. Chabell, "Sea surface salinity and wind retrieval using combined passive and active L-band microwave observations," *IEEE Trans. Geosci. Remote Sens.*, vol. 50, no. 4, pp. 1022–1032, 2012.
- [77] S. H. Yueh *et al.*, "L-band passive and active microwave geophysical model functions of ocean surface winds and applications to Aquarius retrieval," *IEEE Trans. Geosci. Remote Sens.*, vol. 51, no. 9, pp. 4619–4632, 2013.
- [78] S. Yueh, A. Fore, W. Tang, H. Akiko, and B. Stiles, "L-Band Active-Passive Microwave Remote Sensing of Ocean Surface Wind During Hurricanes," *2016 IEEE Int. Geosci. Remote Sens. Symp.*, pp. 2235–2238, 2016.
- [79] J. Gao, G. Tang, and Y. Hong, "Similarities and improvements of GPM dual-frequency precipitation radar (DPR) upon TRMM precipitation radar (PR) in global precipitation rate estimation, type classification and vertical profiling," *Remote Sens.*, vol. 9, no. 11, pp. 1–26, 2017.
- [80] F. J. Wentz and T. Meissner, "Atmospheric absorption model for dry air and water vapor at microwave frequencies below 100 GHz derived from spaceborne radiometer observations," *Radio Sci.*, 2016.
- [81] T. Iguchi, "Dual-frequency precipitation radar (DPR) on the global precipitation

- measurement (GPM) mission's core observatory" in *Satellite Precipitation Measurement*, Springer, pp. 183-192, 2020, [online] Available: [https://link.springer.com/chapter/10.1007/978-3-030-24568-9\\_11](https://link.springer.com/chapter/10.1007/978-3-030-24568-9_11).
- [82] D. Newell *et al.*, "GPM Microwave Imager (GMI) on-orbit performance and calibration results," *Int. Geosci. Remote Sens. Symp.*, vol. 2015-Novem, pp. 5158–5161, 2015.
- [83] D. W. Draper *et al.*, "The Global Precipitation Measurement ( GPM ) Microwave Imager ( GMI ): Instrument Overview and Early On-Orbit Performance," *IEEE J. Sel. Top. Appl. Earth Obs. Remote Sens.*, vol. 8, no. 7, pp. 3452–3462, 2015.
- [84] D. Draper and D. Newell, "Global Precipitation Measurement (GPM) Microwave Imager (GMI) after four years on-orbit," *15th Spec. Meet. Microw. Radiom. Remote Sens. Environ. MicroRad 2018 - Proc.*, pp. 10–13, 2018.
- [85] F. J. Wentz and D. Draper, "On-orbit absolute calibration of the global precipitation measurement microwave imager," *J. Atmos. Ocean. Technol.*, vol. 33, no. 7, pp. 1393–1412, 2016.
- [86] A. Hossan, M. Jacob, and W. L. Jones, "Active/Passive ocean wind vector measurements from GPM core observatory," *16th Spec. Meet. Microw. Radiom. Remote Sens. Environ. MicroRad 2020 - Proc.*, pp. 1–4, 2020.
- [87] A. Hossan, M. Jacob, and W. L. Jones, "Ocean Vector Wind Measurements from GPM to Study Diurnal Cycles of Tropical Winds," *Int. Geosci. Remote Sens. Symp.*, pp. 7330–7333, 2021.
- [88] A. Hossan and W. L. Jones, "Wind Vector and SST Dependence of Ku- and Ka- Band Ocean Surface Nrcs At Low Incidence Angles," *Int. Geosci. Remote Sens. Symp.*, vol. 2021-July, pp. 8003–8006, 2021.
- [89] A. Hossan, M. Jacob, and L. Jones, "Ocean Vector Wind Retrievals From TRMM Using a Novel Combined Active/Passive Algorithm," *IEEE J. Sel. Top. Appl. Earth Obs. Remote Sens.*, vol. 13, pp. 5569–5579, 2020.
- [90] A. Hossan, M. Jacob, W. Linwood Jones, and H. Medrozo, "An active/passive microwave retrieval algorithm for inferring ocean vector winds from TRMM," *15th Spec. Meet.*



*Microw. Radiom. Remote Sens. Environ. MicroRad 2018 - Proc.*, pp. 30–35, 2018.

- [91] A. Hossan, I. S. Member, M. Jacob, I. S. Member, W. L. Jones, and I. L. Fellow, “Microwave Active/Passive Measurements of Diurnal Ocean Wind Vector from TRMM,” pp. 2–6, 2018.
- [92] A. Hossan and W. Linwood Jones, “Ku-and Ka-band ocean surface radar backscatter model functions at low-incidence angles using full-swath gpm dpr data,” *Remote Sens.*, vol. 13, no. 8, 2021.
- [93] N. Majurec, J. T. Johnson, S. Tanelli, and S. L. Durden, “Comparison of model predictions with measurements of ku-and ka-band near-nadir normalized radar cross sections of the sea surface from the genesis and rapid intensification processes experiment,” *IEEE Trans. Geosci. Remote Sens.*, vol. 52, no. 9, pp. 5320–5332, 2014.
- [94] C. Kummerow, W. Barnes, T. Kozu, J. Shiue, and J. Simpson, “The Tropical Rainfall Measuring Mission (TRMM) Sensor Package,” *J. Atmos. Ocean. Technol.*, vol. 15, no. 3, pp. 809–817, Jun. 1998.
- [95] W. L. Jones, S. Soisuvarn, Jun Park, I. Adams, and T. Kasparis, “Combined active and passive microwave sensing of ocean surface wind vector from TRMM,” *Ocean. '02 MTS/IEEE*, vol. 4, no. August 2014, pp. 1981–1986, 2002.
- [96] S. Soisuvarn, W. L. Jones, and T. Kasparis, “Combined Active and Passive Microwave Sensing of Ocean Surface Wind Vector from TRMM.”
- [97] L. Li, E. Im, S. Member, L. N. Connor, P. S. Chang, and S. Member, “Retrieving Ocean Surface Wind Speed From the TRMM Precipitation Radar Measurements,” vol. 42, no. 6, pp. 1271–1282, 2004.
- [98] N. Tran and B. Chapron, “Combined wind vector and sea state impact on ocean nadir-viewing Ku- And C-band radar cross-sections,” *Sensors*, vol. 6, no. 3, pp. 193–207, 2006.
- [99] N. Tran, B. Chapron, and D. Vandemark, “Effect of long waves on Ku-band ocean radar backscatter at low incidence angles using TRMM and altimeter data,” *IEEE Geosci. Remote Sens. Lett.*, vol. 4, no. 4, pp. 542–546, 2007.

- [100] X. Chu, Y. He, and V. Y. Karaev, "Relationships between ku-band radar backscatter and integrated wind and wave parameters at low incidence angles," *IEEE Trans. Geosci. Remote Sens.*, vol. 50, no. 11 PART2, pp. 4599–4609, 2012.
- [101] S. Tanelli, S. L. Durden, and E. Im, "Simultaneous measurements of ku- and ka-band sea surface cross sections by an airborne radar," *IEEE Geosci. Remote Sens. Lett.*, vol. 3, no. 3, pp. 359–363, Jul. 2006.
- [102] Q. Yan, J. Zhang, C. Fan, and J. Meng, "Analysis of Ku- and Ka-Band Sea Surface Backscattering Characteristics at Low-Incidence Angles Based on the GPM Dual-Frequency Precipitation Radar Measurements," *Remote Sens.*, vol. 11, no. 7, p. 754, 2019.
- [103] F. Nouguier, A. Mouche, N. Rasclé, B. Chapron, and D. Vandemark, "Analysis of Dual-Frequency Ocean Backscatter Measurements at Ku-and Ka-Bands Using Near-Nadir Incidence GPM Radar Data," *IEEE Geosci. Remote Sens. Lett.*, vol. 13, no. 9, pp. 1310–1314, 2016.
- [104] Z. Wang *et al.*, "SST Dependence of Ku-and C-Band Backscatter Measurements," *IEEE J. Sel. Top. Appl. Earth Obs. Remote Sens.*, vol. 10, no. 5, pp. 2135–2146, 2017.
- [105] F. J. Wentz, T. Meissner, J. Scott, and K. A. Hilburn, "Remote Sensing Systems GPM GMI Daily Environmental Suite on 0.25 Deg Grid, Version 8.2, [2019]," Remote Sensing Systems, Santa Rosa, CA, USA, 2019. [Online]. Available: [www.remss.com/missions/gmi](http://www.remss.com/missions/gmi). [Accessed: Jan. 15, 2021].
- [106] H. Hersbach *et al.*, "The ERA5 global reanalysis," *Q. J. R. Meteorol. Soc.*, vol. 146, no. 730, pp. 1999–2049, Jul. 2020.
- [107] X. Chu, Y. He, and G. Chen, "Asymmetry and anisotropy of microwave backscatter at low incidence angles," *IEEE Trans. Geosci. Remote Sens.*, vol. 50, no. 10 PART2, pp. 4014–4024, 2012.
- [108] N. Tran, D. Vandemark, C. S. Ruf, and B. Chapron, "The dependence of nadir ocean surface emissivity on wind vector as measured with microwave radiometer," *IEEE Trans. Geosci. Remote Sens.*, vol. 40, no. 2, pp. 515–523, 2002.
- [109] D. Vandemark, B. Chapron, H. Feng, and A. Mouche, "Sea Surface Reflectivity Variation

- With Ocean Temperature at Ka-Band Observed Using Near-Nadir Satellite Radar Data,” *IEEE Geosci. Remote Sens. Lett.*, vol. 13, no. 4, pp. 510–514, 2016.
- [110] D. Ho and A. Asem, “NOAA AVHRR image referencing,” *Int. J. Remote Sens.*, vol. 7, no. 7, pp. 895–904, 1986.
- [111] X. Chu, Y. He, and G. Chen, “Asymmetry and anisotropy of microwave backscatter at low incidence angles,” *IEEE Trans. Geosci. Remote Sens.*, vol. 50, no. 10 PART2, pp. 4014–4024, 2012.
- [112] A. Mouche, V. Kudryavstev, D. Hauser, G. Caudal, and B. Chapron, “Use of dual polarization radar measurements to understand the azimuth behavior of the sea surface backscattered signal,” *Int. Geosci. Remote Sens. Symp.*, pp. 1867–1870, 2006.
- [113] Y. Y. Yurovsky, V. N. Kudryavtsev, S. A. Grodsky, and B. Chapron, “Ka-Band Dual Copolarized Empirical Model for the Sea Surface Radar Cross Section,” *IEEE Trans. Geosci. Remote Sens.*, vol. 55, no. 3, pp. 1629–1647, 2017.
- [114] D. Vandemark, B. Chapron, H. Feng, and A. Mouche, “Sea Surface Reflectivity Variation With Ocean Temperature at Ka-Band Observed Using Near-Nadir Satellite Radar Data,” *IEEE Geosci. Remote Sens. Lett.*, vol. 13, no. 4, pp. 510–514, 2016.
- [115] Z. Wang *et al.*, “SST Dependence of Ku- and C-Band Backscatter Measurements,” *IEEE J. Sel. Top. Appl. Earth Obs. Remote Sens.*, vol. 10, no. 5, pp. 2135–2146, 2017.
- [116] T. Meissner and F. J. Wentz, “The emissivity of the ocean surface between 6 and 90 GHz over a large range of wind speeds and earth incidence angles,” *IEEE Trans. Geosci. Remote Sens.*, vol. 50, no. 8, pp. 3004–3026, 2012.
- [117] T. Meissner and F. Wentz, “An updated analysis of the ocean surface wind direction signal in passive microwave brightness temperatures,” *IEEE Trans. Geosci. Remote Sens.*, vol. 40, no. 6, pp. 1230–1240, 2002.
- [118] W. Berg *et al.*, “Intercalibration of the GPM microwave radiometer constellation,” *J. Atmos. Ocean. Technol.*, vol. 33, no. 12, pp. 2639–2654, 2016.

- [119] P. S. Chang and L. Li, "Ocean surface wind speed and direction retrievals from the SSM/I," *IEEE Trans. Geosci. Remote Sens.*, vol. 36, no. 6, pp. 1866–1871, 1998.
- [120] G. Huffman *et al.*, "NASA GPM Integrated Multi-satellitE Retrievals for GPM (IMERG) Algorithm Theoretical Basis Document (ATBD) Version 06," *Nasa/Gsfc*, no. January, p. 29, 2020.
- [121] M. Kazumori and S. J. English, "Use of the ocean surface wind direction signal in microwave radiance assimilation," *Q. J. R. Meteorol. Soc.*, vol. 141, no. 689, pp. 1354–1375, 2015.
- [122] P. W. Gaiser *et al.*, "The windSat spaceborne polarimetric microwave radiometer: Sensor description and early orbit performance," *IEEE Trans. Geosci. Remote Sens.*, vol. 42, no. 11, pp. 2347–2361, 2004.
- [123] S. Soisuvarn, "An ocean surface wind vector model function for a spaceborne microwave radiometer and its application," PhD dissertation, University of Central Florida, Orlando, FL, USA, 2006.
- [124] S. Soisuvarn, Z. Jelenak, and W. L. Jones, "An ocean surface wind vector model function for a Spaceborne Microwave Radiometer," *IEEE Trans. Geosci. Remote Sens.*, vol. 45, no. 10, pp. 3119–3130, 2007.
- [125] L. N. Connor and P. S. Chang, "Ocean surface wind retrievals using the TRMM microwave imager," *IEEE Trans. Geosci. Remote Sens.*, vol. 38, no. 4 II, pp. 2009–2016, 2000.
- [126] T. Meissner and F. J. Wentz, "Wind-vector retrievals under rain with passive satellite microwave radiometers," *IEEE Trans. Geosci. Remote Sens.*, vol. 47, no. 9, pp. 3065–3083, 2009.
- [127] T. Meissner, L. Ricciardulli, and F. Wentz, "All-weather wind vector measurements from intercalibrated active and passive microwave satellite sensors," *Int. Geosci. Remote Sens. Symp.*, pp. 1509–1511, 2011.
- [128] M. Portabella and A. Stoffelen, "A probabilistic approach for SeaWinds data assimilation," *Q. J. R. Meteorol. Soc.*, vol. 130, no. 596 PART A, pp. 127–152, 2004.

- [129] J. Vogelzang, A. Stoffelen, A. Verhoef, J. De Vries, and H. Bonekamp, "Validation of two-dimensional variational ambiguity removal on SeaWinds scatterometer data," *J. Atmos. Ocean. Technol.*, vol. 26, no. 7, pp. 1229–1245, 2009.
- [130] B. Chapron, F. Collard, and F. Ardhuin, "Direct measurements of ocean surface velocity from space: Interpretation and validation," *J. Geophys. Res. C Ocean.*, vol. 110, no. 7, pp. 1–17, 2005.
- [131] D. G. Long and M. W. Spencer, "Radar backscatter measurement accuracy for a spaceborne pencil-beam wind scatterometer with transmit modulation," *IEEE Trans. Geosci. Remote Sens.*, vol. 35, no. 1, pp. 102–114, 1997.
- [132] M. Portabella and A. Stoffelen, "Quality control and wind retrieval for Seawinds," *Sci. Rep. WR-2002-01*, no. February, 2000.
- [133] A. G. Fore, S. H. Yueh, W. Tang, B. W. Stiles, and A. K. Hayashi, "Combined Active / Passive Retrievals of Ocean Vector Wind and Sea Surface Salinity With SMAP," *IEEE Trans. Geosci. Remote Sens.*, vol. 54, no. 12, pp. 7396–7404, 2016.
- [134] A. G. Fore, B. W. Stiles, A. H. Chau, B. A. Williams, R. S. Dunbar, and E. Rodríguez, "Point-wise wind retrieval and ambiguity removal improvements for the QuikSCAT climatological data set," *IEEE Trans. Geosci. Remote Sens.*, vol. 52, no. 1, pp. 51–59, 2014.
- [135] S. J. Shaffer, R. S. Dunbar, S. V. Hsiao, and D. G. Long, "A Median-Filter-Based Ambiguity Removal Algorithm for NSCAT," *IEEE Trans. Geosci. Remote Sens.*, vol. 29, no. 1, pp. 167–174, 1991.
- [136] R. N. Hoffman, S. M. Leidner, J. M. Henderson, R. Atlas, J. V. Ardizzone, and S. C. Bloom, "A two-dimensional variational analysis method for NSCAT ambiguity removal: Methodology, sensitivity, and tuning," *J. Atmos. Ocean. Technol.*, vol. 20, no. 5, pp. 585–605, 2003.
- [137] W. Lin, M. Portabella, A. Stoffelen, J. Vogelzang, and A. Verhoef, "On mesoscale analysis and ASCAT ambiguity removal," *Q. J. R. Meteorol. Soc.*, vol. 142, no. 697, pp. 1745–1756, 2016.
- [138] W. Zhixiong, Z. Chaofang, and Z. O. U. Juhong, "An improved wind retrieval algorithm

- for the HY-2A scatterometer,” vol. 33, no. 5, pp. 1201–1209, 2015.
- [139] J. Vogelzang, “Two-dimensional variational ambiguity removal ( 2DVAR ) ver 1.8,” pp. 1–64, 2022.
- [140] L. Ricciardulli, T. Meissner, and F. Wentz, “Towards a Climate Data Record of satellite ocean vector winds,” *Int. Geosci. Remote Sens. Symp.*, pp. 2067–2069, 2012.
- [141] L. Ricciardulli and F. J. Wentz, "Remote Sensing Systems ASCAT C-2015 Daily Ocean Vector Winds on 0.25 deg grid, Version 02.1," in *Remote Sensing Systems*, Santa Rosa, CA, USA, April 2016, [2021]. Available: [www.remss.com](http://www.remss.com). Accessed on: Jul. 18, 2022.
- [142] M. Portabella and A. Stoffelen, “Scatterometer backscatter uncertainty due to wind variability,” *IEEE Trans. Geosci. Remote Sens.*, vol. 44, no. 11, pp. 3356–3361, 2006.
- [143] T. Elfouhaily, D. Vandemark, J. Gourrion, and B. Chapron, “Estimation of wind stress using dual-frequency TOPEX data,” *J. Geophys. Res. Ocean.*, vol. 103, no. C11, pp. 25101–25108, 1998.